Coloring photovoltaic modules using printed textiles: Fabrication, validation and the prediction of appearance & energy yield

Von der Fakultät für Mathematik und Physik

der Gottfried Wilhelm Leibniz Universität Hannover

zur Erlangung des akademischen Grades

Doktor der Naturwissenschaften

Dr. rer. nat.

genehmigte Dissertation von

M.Sc. Timo Gewohn

2023

Referent:	Prof. Dr. Rolf Brendel
Korreferenten:	Prof. Dr. Gunther Seckmeyer
	Prof. Dr. Arthur Weeber
Tag der Promotion:	20.07.2023

Abstract

The targets set by many nations to increase renewable energy production lead to a greater demand for photovoltaic modules (PV). In order to reduce the additional area required, it is advisable to first utilize existing areas that were previously unused for energy generation. As a result, building-integrated PV modules, especially those integrated into façades, are gaining in importance. However, such PV modules not only provide energy, they also have to meet aesthetic requirements. For a cost-benefit analysis and the calculation of the payback period, an accurate yield prediction is essential. However, a yield prediction for PV modules modified in appearance and mounted vertically onto a façade is less accurate than a yield prognosis for standard and roof-mounted modules. In this work, I present the Colored Textile (CoTex) method, which alters the appearance of PV modules by using imprinted textiles, such as nonwovens. I validate this method by various laboratory and long-term measurements in terms of durability, energy yield and appearance of such CoTex modules. Depending on the selection of the textile used and the printed color, the energy yield varies. For example, a PV module in light gray design achieves an energy yield of 89% compared to a standard module.
The CoTex method allows endless possibilities for the appearance of the manufactured modules by using printed materials. Depending on the textiles and printing parameters used, a different appearance is created. To ensure that the appearance and energy output of specific CoTex modules are known before they are manufactured, I perform the simulation of a digital prototype. After calibration based on eight different colored sample modules, a digital prototype can be simulated for any combination of the three printing inks cyan, magenta and yellow. The deviation between the simulated and the measured color are hardly perceptible for an observer, the deviation of the simulated from the measured energy yield is below 2 %.
Using the energy yield determined by the digital prototype, a total yield prediction can be performed for a CoTex module. By applying the ground view factor for vertically mounted PV modules and including ground shading from objects in the surrounding area, I reduce the deviation between measured and simulated energy yield by up to 10.5 % over a 12-month period compared to using the standard model to calculate ground reflectance. By adding an angular correction of the transmission of the CoTex layer depending on the position of the sun, the yield prediction for CoTex modules can be performed with an accuracy comparable to that of standard PV modules.

Key words: Colored photovoltaic modules, digital prototype, energy yield prognosis

Zusammenfassung

Der Transfer des Energiesystems hin zu einem höheren Anteil an regerenativen Energiequellen führt zu einem größeren Bedarf an installierten Photovoltaikanlagen. Um den zusätzlichen Flächenbedarf zu reduzieren, bietet es sich an, bereits bestehende und bisher für die Energieerzeugung ungenutzte Flächen zu erschließen. Dadurch gewinnen gebäudeintegrierte Photovoltaikmodule (PV-Module) an Bedeutung. Solche PV-Module dienen jedoch nicht nur der Energieerzeugung, sie müssen auch ästhetischen Ansprüchen genügen. Für eine Kosten-Nutzen-Analyse und der Berechnung der Amortisationszeit ist eine genaue Ertragsprognose essentiell. Die Ertragsprognose äußerlich veränderte und vertikal angebrachte PV-Module ist bisher jedoch nur mit einer deutlich geringeren Genauigkeit als für auf Dachflächen installierte PV-Module möglich.
In dieser Arbeit stelle ich die *Colored Textile* (CoTex) - Methode vor, mit welcher das Aussehen von PV-Modulen durch die Verwendung von bedruckten Textilien verändert werden kann. Diese Methode wird durch Labor- und Langzeitmessungen in Bezug auf die Haltbarkeit, den Energieertrag und das Aussehen validiert. Je nach Wahl der Materialien variiert der Energieertrag. Ein PV-Modul im hellgrauen Design erreicht beispielsweise einen Energieertrag von 89% verglichen mit einem Standardmodul.
Die CoTex Methode erlaubt durch die Verwendung von bedruckten Materialien unendlich viele Möglichkeiten zur Variation des Aussehens der fertigen Module. Damit schon vor der Herstellung bestimmter CoTex-Module das Aussehen und der Energieertrag bekannt sind, führe ich die Simulation eines digitalen Prototyps durch. Nach Kalibrierung auf Basis von acht verschiedenfarbigen Probemodulen kann ein digitaler Prototyp für jede beliebige Kombination der drei Tinten Cyan, Magenta und Gelb simuliert werden. Die Abweichung zwischen der simulierten und der gemessenen Farbe sind dabei für einen Beobachter kaum wahrnehmbar, die Abweichung des simulierten vom gemessenen Energieertrag liegt unter 2%.
Mit dem simulierten Energieertrag erstelle ich eine vollständige Ertragsprognose für ein CoTex-Modul. Durch die Verwendung des Bodensichtfaktors für vertikal montierte PV-Module und das Einbeziehen von Verschattung, reduziere ich die Abweichung zwischen gemessenem und simulierten Energieertrag um bis zu 10.5% im Vergleich zur Verwendung des Standardmodells zur Berechnung der Bodenreflektion. Ich nutze eine Einfallswinkelkorrektur der Transmission der CoTex-Schicht und erreiche damit bei der Ertragsprognose eine ähnliche Genauigkeit wie für Standard PV-Module.

Stichwörter: Farbige Photovoltaikmodule, digitaler Prototyp, Ertragsprognose

Contents

List of Abbreviations **vii**

Symbols **ix**

1 Introduction **1**

2 Theory **4**

2.1 Color theory 4

2.1.1 The Eye 4

2.1.2 Color Vision 5

2.1.3 Trichromacy 6

2.1.4 The CIE color space 8

2.1.5 Color difference 10

2.2 Simulation of appearance and energy yield 11

2.2.1 Color mixing and printing 12

2.2.2 The Clapper-Yule model 13

2.2.3 Simulation of the external quantum efficiency 17

2.3 Energy yield prognosis 20

2.3.1 Irradiation 21

2.3.2 Ground view factor 22

2.3.3 Calculation of the ground diffuse irradiation 25

2.3.4 Calculation of the energy yield 27

3 State of the art **29**

3.1 Colored building-integrated photovoltaic modules 29

3.1.1 Theoretical consideration of colored solar cells 29

3.1.2 Techniques for coloring solar cells and PV modules 31

3.1.3 Classification of colored PV modules with respect to appearance and energy yield 34

3.2 Energy yield estimation 35

4 Postproduction coloring of PV modules with imprinted textiles **40**

4.1 Fabrication and measurement methods 40

4.1.1 Fabrication of customized PV modules containing textile layer . 40

4.1.2 Coloring of the nonwoven fabrics . . . 41
4.1.3 Durability tests . . . 42
4.1.4 UV-stability test . . . 43
4.1.5 Measurement of the reflection spectrum . . . 44
4.1.6 Measurement of the external quantum efficiency . . . 44
4.1.7 Measurement of the short-circuit current density . . . 45
4.1.8 Measurements at the outdoor façade test facility . . . 45
4.2 Analysis of the appearance, energy yield and durability of CoTex PV modules . . . 46
4.2.1 Position of the textile . . . 46
4.2.2 Visual assessment of the samples . . . 47
4.2.3 EQE and short-circuit current of customized modules . . . 51
4.2.4 Durability and outdoor test . . . 54
4.2.5 UV-stability . . . 56
4.2.6 Long-term outdoor application . . . 60
4.2.7 Cost estimation . . . 62
4.3 Conclusion of Chapter 4 . . . 62

5 Simulation of a digital prototype 63
5.1 Sample preparation and simulation methods . . . 64
5.1.1 Coloring of the samples . . . 64
5.1.2 Simulation of the digital prototype of colored BIPV modules . . . 65
5.1.3 Correction of ink spreading . . . 66
5.2 Visual assessment of the samples . . . 66
5.3 Simulation of the digital prototype . . . 68
5.3.1 Investigation of samples I40 . . . 69
5.3.2 Investigation of the samples I50 . . . 72
5.3.3 Investigation of the samples O50 . . . 75
5.3.4 Investigation of the samples CF . . . 79
5.4 Ink spreading correction . . . 82
5.5 Consequences of printing inaccuracies . . . 84
5.6 Conclusion of Chapter 5 . . . 85

6 Energy yield calculation 89
6.1 Methods for the energy yield calculation . . . 89
6.1.1 Calculation of the diffuse and the direct irradiance fraction . . . 90
6.1.2 Transposition of the diffuse insolation . . . 90
6.1.3 Accuracy of the GVI calculation . . . 91
6.1.4 Data for annual irradiance calculation . . . 92
6.2 Dependence of I_{ground} on environmental parameters . . . 94
6.3 Accuracy of various irradiation calculation models . . . 96
6.3.1 Accuracy of decomposition models . . . 96

6.3.2 Accuracy of transposition models 97
6.3.3 Annual deviation of the irradiance 100
6.4 Energy yield calculation for façade modules 101
6.4.1 Accuracy of yield calculation for façade modules 101
6.4.2 Accuracy of energy yield calculation of CoTex modules 102
6.5 Conclusion of Chapter 6 104

7 Summary **106**
7.1 Fabrication and validation of the CoTex PV modules 106
7.2 Implementation and validation of the simulation of a digital prototype . 107
7.3 Improvement and accuracy of the yield prediction for façade modules . . 108

A Appendix **109**
A.1 Calculation of the color difference ΔE_{00} 109
A.2 Equations and coefficients for the Perez diffuse transposition model . . . 110
A.3 Results with different decomposition models 111
A.4 Sandia Array Performance Model 112

Bibliography **114**

List of Publications **122**

Acknowledgements **124**

List of Abbreviations

AOI Angle of Incidence

ARC Anti-Reflection Coating

a-Si Amorphous Silicon

BAPV Building-Applied Photovoltaics

BIPV Building-Integrated Photovoltaic

CIE Commission Internationale de l'Éclairage

CoTex Colored Textiles

CPI Color Performance Index

c-Si Crystalline Silicon

DHI Diffuse Horizontal Irradiance

DNI Direct Normal Irradiance

DVI Diffuse Vertical Irradiance

E East

EQE External Euantum Efficiency

FPLD Freudenberg Performance Light Diffuser

GHI Global Horizontal Irradiance

GVF Ground View Factor

GVI Global Vertical Irradiance

IMUK Institute of Meteorology and Climatology Hannover

IQE Internal Quantum Efficiency

IR Infrared

ISFH Institute for Solar Energy Research Hamelin

I-V Current-Voltage

MPP Maximum Power Point

N North

nZEBs nearly Zero Energy Buildings

POA Plane of Array

PV Photovoltaic

PVGIS Photovoltaic Geographical Information System

S South

SE South-East

SPD Spectral Power Distribution

STC Standard Test Conditions

SW South-West

TMY Typical Meteorological Year

UV Ultraviolet

W West

Symbols

Symbol	Description	Unit
I_{MPP}	Current at the maximum power point	A
I_{SC}	Short-circuit current	A
J_{SC}	Short-circuit current density	$\mathrm{mA\,cm^{-2}}$
I_{X}	Current at $\frac{1}{2}V_{\mathrm{OC}}$	A
I_{XX}	Current at $\frac{1}{2}(V_{\mathrm{OC}} + V_{\mathrm{MPP}})$	A
e	Relative root mean square error	
V_{MPP}	voltage at the maximum power point	V
P_{MPP}	Power at the maximum power point	W
V_{OC}	Open-circuit voltage	V
$\overline{x}$	Mean value	
σ	Standard deviation	
x_{i}	Measured value	
y_{i}	Reference value	
R	Reflection	
λ	Wavelength	nm
X	X coordinate of CIE-XYZ color space	
Y	Y coordinate of CIE-XYZ color space	
Z	Z coordinate of CIE-XYZ color space	
x	x coordinate of CIE-xyY color space	
y	y coordinate of CIE-xyZ color space	
$\bar{x}$	Color matching function for the S cone	
$\bar{y}$	Color matching function for the M cone	
$\bar{z}$	Color matching function for the L cone	
$L*$	L* coordinate of CIE-L*a*b* color space	
$a*$	a* coordinate of CIE-L*a*b* color space	
$b*$	b* coordinate of CIE-L*a*b* color space	
$\Delta E_{1,2}$	Euclidean color distance between two colors	
ΔE_{00}	CIE color distance between two colors	
I_{meas}	Measured irradiance	$\mathrm{W\,m^{-2}}$
I_{calc}	Calculated irradiance	$\mathrm{W\,m^{-2}}$

Symbol	Description	Unit
$I_{\text{Ground, Std.}}$	Ground reflected irradiance, calculated with the standard method	$\mathrm{W\,m^{-2}}$
$I_{\text{Ground, GVF}}$	Ground reflected irradiance, calculated using the ground view factor	$\mathrm{W\,m^{-2}}$
$I_{\text{Ground, GVF sh.}}$	Ground reflected irradiance, calculated using the ground view factor and ground shading	$\mathrm{W\,m^{-2}}$
$\overline{I_{\text{meas}}}$	Mean measured irradiance	$\mathrm{W\,m^{-2}}$
N	Number of data used	
$r_{J_{\text{SC}}}$	Ratio of J_{SC} between a CoTex and a reference module	
$\Delta r_{J_{\text{SC}}}$	Deviation of the $r_{J_{SC}}$	
E_{CoTex}	Energy yield of CoTex module	kW
E_{ref}	Energy yield of reference module	kW
$r_{\text{CoTex/ref}}$	Ratio between E_{CoTex} and E_{ref}	
E_{A}	Extraterrestrial irradiance	$\mathrm{W\,m^{-2}}$
k_{D}	Diffuse fraction	
k_{T}	Clearness index	
θ_{Z}	Zenith angle of the sun	°
ϵ	Sky clearness parameter	
Δ	Sky brightness parameter	
AM	Relative air mass	
θ	Angle of incidence	°
A	Transmittance of beam irradiance through the atmosphere for the transposition models of Hay & Davies and Reindl *et al.*	
F	Modulating function for the transposition modell of Klucher *et al.*	
f	Horizontal brightening correction factor for the transposition model of *Reindl et al.*	
α	PV module tilt angle	°
F_1	Circumsolar brightness coefficient	
F_2	Horizon brightness coefficient	
a	Solid angle occupied by the circumsolar region, as seen from the POA	°
c	Solid angle occupied by the circumsolar region, as seen from the horizontal plane	°
R_{b}	Ratio of beam irradiance on a tilted surface to that on a horizontal plane	

Chapter 1

Introduction

In order to realize the transformation of the energy system to climate-neutral energy generation, a massive expansion of renewable energy sources is necessary. One of these energy sources is Photovoltaic (PV), which is indispensable both with regard to the prevention of climate change and its economic efficiency of energy production. Due to the constantly decreasing prices of PV modules, the costs for the area or the land take an increasingly larger part of the required investment costs for a PV power plant. In order to utilize already built-up areas and thus minimize space requirements for greenfield sites, PV modules are mounted on existing roof surfaces or, in the case of new buildings or renovations, Building-Integrated Photovoltaic (BIPV) modules are integrated directly into the building envelope. The building-integrated variant fulfills a dual function: in addition to generating energy, the BIPV modules also perform the function of the regular building envelope and protect the building from environmental influences. Another driver of the growth in the Building-Applied Photovoltaics (BAPV) and BIPV segment is the European Union's directive for nearly Zero Energy Buildings (nZEBs), which requires new buildings to include some form of renewable energy generation starting in the year 2021 [1]. Due to the increasingly popular choice of a heat pump instead of a conventional gas heating system, the increasing amount of electric vehicles and, last but not least, the rising share of employees who work from home, the electric energy demand in private households is increasing. This also makes a home power system which generates regenerative energy for direct self-consumption more attractive to many landlords from an economic perspective.

BIPV allows the use of surfaces for energy production that already exist but have no other use than being part of the building envelope. But due to their exposed location, BIPV façade systems must satisfy homeowners' and stakeholders' architectural and visual requirements in addition to generating electricity. Therefore, there are many different approaches to modify the appearance of PV modules. These range from only slight changes in color tone, to bright hues or even graphics and patterns that can show almost any appearance, such as that of a solidly built clinker façade. What all methods have in common is the reduction of the energy yield of the PV module. If light is reflected from the PV module thus creating a certain appearance, this light is no longer

available for energy generation. By reducing the energy yield, the power generation cost of such PV modules increases, which in turn extends the payback period. Furthermore, PV modules whose appearance has been changed are more expensive than standard modules because additional materials are needed and process steps have to be changed. In order to improve the cost-benefit ratio of PV modules that have been altered in appearance, the existing methods must be further developed in terms of a higher energy yield or a simpler and thus more cost-effective implementation.

For colored BIPV modules to convince potential customers, three aspects must be fulfilled in the best possible way: First, the appearance have to be convincing. Second and third, the energy yield has to be preferably high and the investment cost preferably low, respectively. The colored PV modules offered on the market so far usually achieve only one or at most two of these aspects (see e.g. [55]). Therefore, further research and development in this field is necessary.

In this work, I present a method for altering the appearance of PV modules by applying colored textiles onto photovoltaic modules. With this technique, different textiles, whether white, dyed or printed, can be used to modify the appearance of photovoltaic modules. I evaluate the technique in terms of, appearance, energy yield, durability in outdoor measurements, UV stability and long-term effects in outdoor operation in the damp-heat test procedure.

The decisive advantages of this method, apart from the low energy loss, are the low manufacturing costs and the high degree of individuality. As the textiles are applied to already manufactured PV modules, the manufacturing process of the PV modules is not changed and any PV modules from mass production can be used. This also enables a high degree of individuality without significantly increasing the price, since only the textile has to be individually selected or printed, but the PV modules themselves can be produced in large quantities.

Additionally, I also present a digital prototype of a PV module, a mathematical model for predicting the appearance and yield of an arbitrarily colored PV module whose appearance has been altered by laminating colored textiles (CoTex) onto the front glass of the module and by using a printed foil. Applied colors, whether by CoTex, colored foils, ceramic printing, or another coloring technique, always appear darker when applied to a PV module due to the dark blue or black solar cells behind the textile. For optimized planning at the beginning of the building process, it is therefore highly advantageous, to be able to offer a certain range of appearance of colored PV modules with information of the respective energy yield. The digital prototype is used to determine the appearance of the finished PV module. I simulate all achievable color variations and the resulting short-circuit current densities by using the reflection and External Euantum Efficiency (EQE) measurements of a set of eight colored PV modules only. I confirm the simulation results by experimental investigations.

In order to increase the further expansion of BIPV façade systems, it is important to enable investors to evaluate the economic viability of façade systems already in the planning phase of buildings. For this purpose, yield prognoses are required. However, the current standard forecasting methods do not adequately represent the special characteristics of BIPV façade systems. In particular, the irradiation reflected from the ground onto the PV module represents a larger share of the total insolation for façade modules than for on-roof PV systems due to the larger inclination angle. Also, the accuracy of the conversion of diffuse irradiance from the horizontal to the module plane decreases with increasing angle of inclination and is therefore lowest for vertically mounted façade modules. In this thesis, I demonstrate how the accuracy of the calculation of the irradiance on such modules can be significantly increased if the ground view factor is used to estimate the irradiance reflected from the ground onto a vertically mounted PV module.

In the following, I will first present the theory for understanding the yield prediction and the simulations of the appearance and yield of the colored PV modules. In particular, I discuss the color theory, and how colors are created and calculated. Subsequently I provide an overview of many different techniques for changing the appearance of PV modules, as well as theoretical work on this topic. The current state of the art of yield prediction of vertically mounted PV modules emphasizes the need for research in this area.

In chapter 4, CoTex modules are investigated experimentally. Various durability tests on the setup, but also on the UV stability of the appearance are carried out. In addition, CoTex modules with different textiles printed and non-printed are examined and compared with regard to their appearance and energy yield.

Chapter 5 presents the simulation of the digital prototype, which predicts the appearance and energy yield of CoTex modules. This involves printing the textiles used in any color combination of the three primary colors cyan, magenta and yellow. The accuracy of the simulation is investigated on four groups of samples, including three different materials and three different printing techniques.

Chapter 6 deals with the energy yield prediction of vertically mounted PV modules. The focus of my work is the successful integration of a ground view factor to improve the accuracy of the calculation of the irradiance reaching the PV module and the application of the yield prediction to CoTex modules.

Chapter 2

Theory

For the understanding of the simulation of the appearance, some photometric fundamentals are required. I will go into detail about the theory of colors and explain how human beings perceive colors. This theoretical background is important to understand how colors can be determined from reflectance spectra. The last section on color theory describes the calculation of color differences. The definitions given there are an important criterion for distinguishing the appearance of colored PV modules before and after any tests or for validating the simulations. The section on color theory is followed by the theory of Clapper and Yule's model, which I use for the simulations of the appearance and energy yield of colored PV modules. In the last section, I briefly explain how an energy yield prognosis works, especially the irradiation conditions and the determination of the characteristic curve of a PV module are presented.

2.1 Color theory

For most people it is natural that they see colors when they look around. It is a very important attribute for humans – and many animals too – that they are able to see colors. It helps us to differentiate between objects in our surrounding and to recognize them. However, why are we able to see colors?
The following description of color vision is mainly based on the work of Bruce MacEvoy [12], the theory of the CIE (International Commission of Illumination, in French *Commission Internationale de l'Éclairage*) color space and the calculation of colors in the book of János Schanda [76].

2.1.1 The Eye

Everything we see comes from visible light being reflected or emitted by objects in our environment and reaching the eye. Visible light is defined as electromagnetic radiation with a wavelength between about 360 nm and 830 nm. Figure 2.1 shows the eye. The incoming light hits the cornea where it is refracted to a fixed focal point. The lens is responsible for the fine adjustment. The eye's focal point is therefore variable

and depends on the shape of the lens. Depending on whether you want to focus on a nearby or distant object, it can be stretched or compressed through the ciliary body. The combination of cornea and lens focuses incoming light on the retina. The amount of light, which enters the pupil, is controlled by the iris. When only dim light reaches the eye, the iris increases the aperture into the pupil and when bright light incidences, the iris reduces the aperture. This can reduce the amount of light which reaches the retina to 5%.

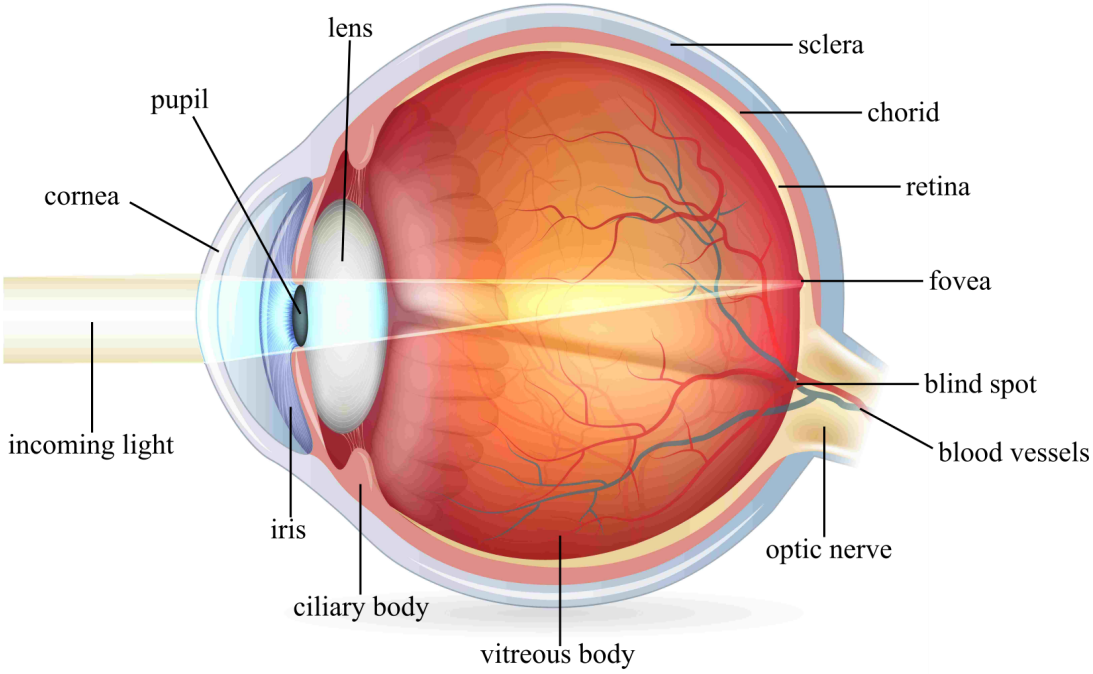

Figure 2.1: The structure of the human eye. Shown is how an incident light beam is focused on the fovea. Illustration reproduced from [8].

The retina consists of a dense network of about 200 million neurons, of which about half are photoreceptor cells and half are secondary cells. When an image is projected onto the retina, signals from the nerve cells are transmitted to the brain via the optic nerve. These signals are processed in the brain to form a color image. The optic nerve is located in the retina and therefore forms the blind spot. We do not perceive light that hits this spot.

2.1.2 Color Vision

There are two types of photoreceptor cells: cones and rods. The about 100 million rods are responsible for vision at night and with only dim light. The 6 million cones respond to daylight luminance and provide information about color and contrast. There are three different types of cones but only one type of rods. As a consequence, there are four different types of photopigments, for the four different photoreceptors. The first type is rhodopsin, it is in the rods and responsible for scotopic vision, most sensitive to green light, which corresponds to wavelength around 505 nm. The opsins in the

three cone types are called photopsins, they cover the visible part of the light spectrum and are therefore divided into short (S), medium (M) and long (L) wavelength ranges. The S-cones are most sensitive to a wavelength of 445 nm, the M-cones to 540 nm and the L-cones to 565 nm. Each photopigment is most likely to react to the light with a wavelength of the maximum of its absorption curve, but with less probability, it reacts to light with other wavelength, too. Figure 2.2 shows the absorption curves of the three different cones. In Figure 2.2 a) the curves are normalized to their peak. It is noticeable that the curves overlap, thus a photon can be absorbed in certain wavelength ranges by different cones. This is very important and essential for our ability to see colors. It can also be seen that the absorption curve of the S-cone is narrower and there are fewer overlaps than with the M- and L- cone. The shapes of the M- and L-cones, on the other hand, look almost identical and overlap in large parts. Furthermore, we can learn from these curves, that human's spectral sensitivity has two maxima. One in the short wavelength range at 445 nm and the other one a broad peak in the long wavelength area between 540 nm and 565 nm. Between those maxima, there is an area of minimum sensitivity between 475 nm and 485 nm. Figure 2.2 b) shows the absorption curves of the cone distributions weighted with their proportions in the retina. The exact ratio between the three photoreceptors is different for every person. From this view it becomes clear that any photon with a wavelength above 445 nm is most likely to be absorbed by a L-cone. When interference occurs over all wavelengths, the absorption probability for a M-cone is only 40% and for a S-Cone only 6% of the probability for a L-cone.

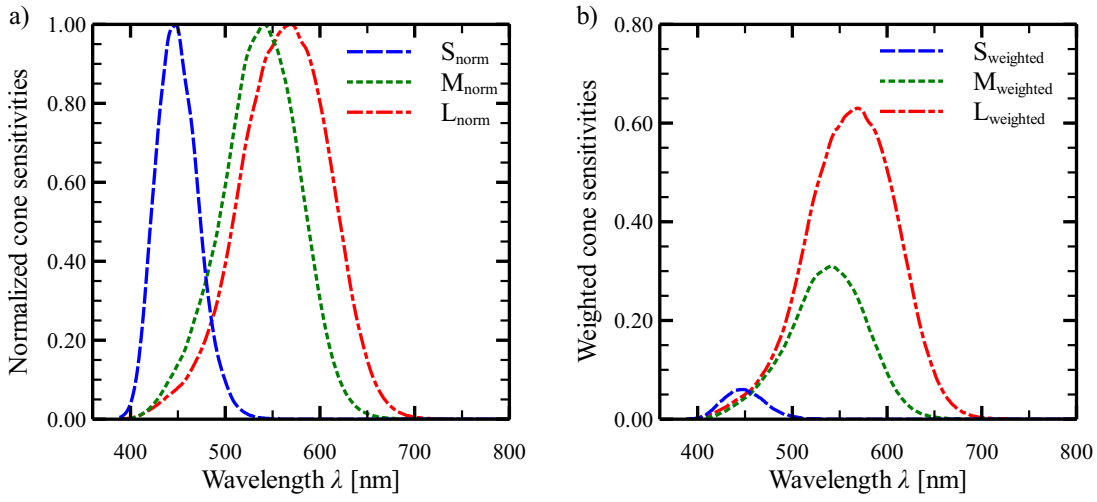

Figure 2.2: a) normalized and b) weighted absorption curves of the S-, M- and L-cones. [83]

2.1.3 Trichromacy

The idea that millions of different colors can be created by combining only three different types of color receptors is called the three-color theory or trichromatic theory of color vision. One of the fundamentals of this theory is that the signals of the three cones are always combined and considered in relation to each other. By assigning a

color to each combination of possible output signals of the photoreceptors, we obtain the color triangle. This triangle contains all possible colors perceptible to humans and thus represents a connection between our color perception and the physical cause of the color stimulus. As explained above, one photoreceptor can be excited by a combination of several wavelengths and light intensities. This means that the brain cannot obtain accurate information about the incident light from a single type of photoreceptor. It is called the principle of univariance, that one individual photoreceptor cannot differentiate between changes in light intensity or changes in the wavelength of incoming light. Only by comparing the output signals of different types of photoreceptors the information about the incoming light can be extracted. To visualize the combination of the three cone types, a three-dimensional space is created. In this cone excitation space, each cone output represents one dimension. Figure 2.3 a) shows an example where the combination of cone sensitivities for the incident wavelengths of 450 nm, 500 nm, and 600 nm are marked with a line. Using the normalized cone sensitivity function fundamental leads to a value combination of M = 0.59, L = 0.39 and S = 0.1 for 500 nm. This can be done for all wavelengths, the result is a curve, called the spectrum locus (Figure 2.3 b) for the monochromatic cone excitations. The spectrum locus contains all possible combinations of cone excitation caused by polychromatic instead of monochromatic light incidence.

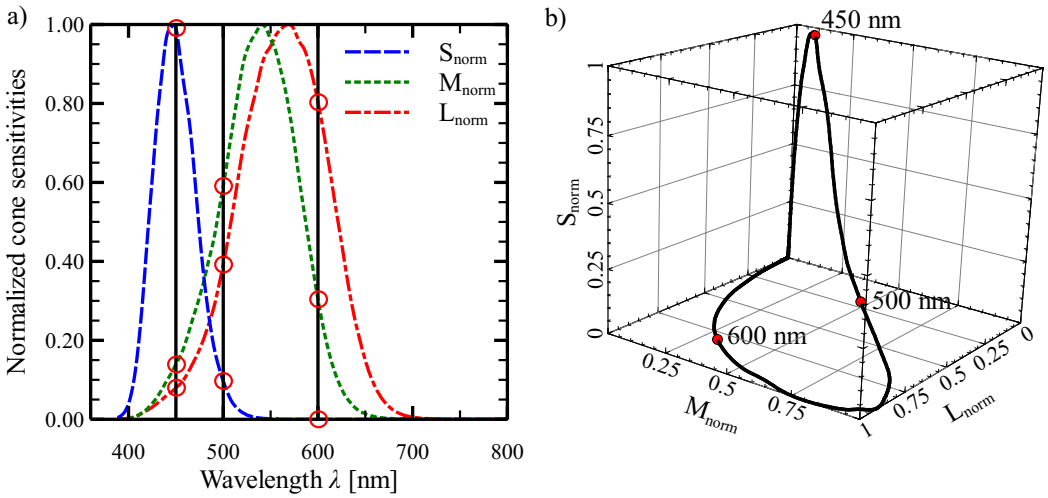

Figure 2.3: a) Combinations of the values of the normalized cone sensitivity functions at incident light with wavelengths of 450 nm, 500 nm, and 600 nm. b) shows the cone spectrum locus, which shows the feasible combinations of S-, M-, and L-cones for all wavelengths. [83]

This cone excitation space depends on the cone sensitivity fundamental which is used. By normalizing to the total cone excitation, the mixing triangle, shown in figure 2.4, can be created from the three-dimensional spectrum locus. It contains the clearer and better known approach of the chromaticity diagram. The blue diamonds mark the spectrum locus, which is shown in figure 2.3 b). The colored area shows the chromaticity diagram resulting from cone excitation by polychromatic light. In this illustration, all possible colors are shown, but the variations of brightness of different

wavelength are removed by dividing the cone excitation by the stimulation in each cone: $C = (\frac{L}{L+M+S}|\frac{M}{L+M+S}|\frac{S}{L+M+S}) = (\frac{L}{B}|\frac{M}{B}|\frac{S}{B}) = (\frac{L}{B}|\frac{M}{B}|\frac{B-L-M}{B})$, where B is the brightness and C the chromaticity, containing the coordinates for the mixing triangle of the cone excitation. Chromaticity consists only of hue and excitation purity and does not include brightness or luminance. For example, the colors white and grey have the same chromaticity, but a different brightness. The edges of the mixing triangle represent the pure cone outputs, which equals the three primary colors. In fact, those pure primary colors can never be seen, because there are always at least two cones excited. When the proportions of all primary colors equal their perceptual weight, we see white light.

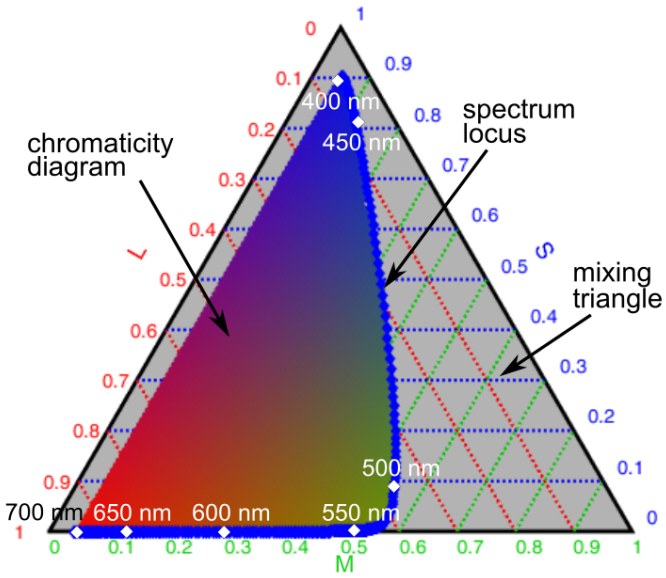

Figure 2.4: The chromaticity diagram shows all possible combinations of excitation of the three cones by the mixing triangle. The chromaticity diagram is enclosed by the spectrum locus, which marks the monochromatic colors. [12]

2.1.4 The CIE color space

In order to determine concrete colors for certain cone stimuli, a color space is needed. I use the three-dimensional Commission Internationale de l'Éclairage (CIE) XYZ color space to determine colors as seen by the human eye. Since the number of individual cones in the eye and thus the color vision differs from person to person, a standard observer and his color vision were defined by the CIE color matching functions [74]. Figure 2.5 a) shows the three color matching functions $\bar{x}$, $\bar{y}$ and $\bar{z}$, which are weighting functions for the light sensitivity of the three different cone cells of the eye of the standard observer and are determined in the wavelength range from 360 nm to 830 nm. For the calculation of the color, which the standard observer perceives from a certain object, the reflection spectrum $R(\lambda)$ of the object as well as the relative Spectral Power Distribution (SPD) of the incident light are decisive. This relative SPD indicates the normalized power per area per wavelength λ of the incident light, or of a light source.

Figure 2.5 b) shows the Standard Daylight Illuminant CIE-D65, which is based on the daylight in Western and Northern Europe, and used as the SPD for the standard observer [48]. For comparison, the AM1.5g spectrum [15], which is more familiar in the PV sector, is also shown.

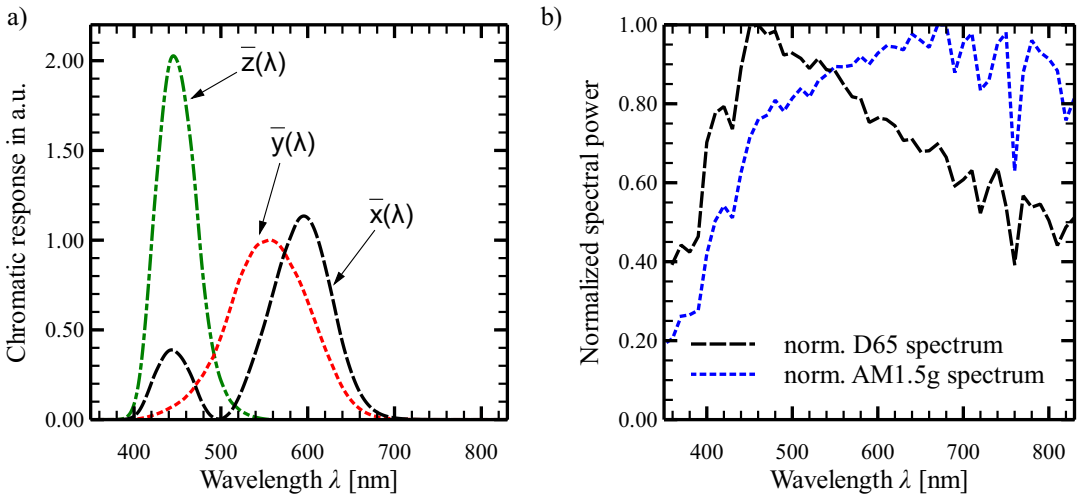

Figure 2.5: a) Color matching functions $\bar{x}$, $\bar{y}$ and $\bar{z}$ of the CIE color space. b) CIE Standard Daylight illuminant D65 (dashed black line) and the normalized AM1.5g spectrum (blue dotted line). [76]

We determine the X, Y and Z coordinates of the CIE color system, which are called the tristimulus values, using

$$\begin{aligned} X &= \int_{360nm}^{830nm} R(\lambda) D65(\lambda) \bar{x}(\lambda) d\lambda \\ Y &= \int_{360nm}^{830nm} R(\lambda) D65(\lambda) \bar{y}(\lambda) d\lambda \\ Z &= \int_{360nm}^{830nm} R(\lambda) D65(\lambda) \bar{z}(\lambda) d\lambda. \end{aligned} \tag{2.1}$$

In order to represent the three-dimensional color space more simply, the Z-component for each point of the color chart is determined mathematically from the other two by the relationship $x + y + z = 1$. When x and y are defined by:

$$x = \frac{X}{X+Y+Z} \quad \text{and} \quad y = \frac{Y}{X+Y+Z} \tag{2.2}$$

each X, Y, Z triple can be associated with a color from the CIE chromaticity diagram that is shown in Figure 2.6 a). By this simplification, as already with the mixing triangle in Figure 2.4, only the chromaticity and not the brightness of the colors is mapped.

2.1.5 Color difference

An important aspect in this thesis is the assessment of the appearance of colored PV modules before and after different tests, as well as the comparison between simulated and measured colors. To perform this comparison quantitatively, we determine the color difference between two colors.
Figure 2.6 a) shows the CIE xy chromaticity diagram with the colors of the possible combinations of the three photoreceptors in a two-dimensional plane in the CIE xy color space. Thus, information is lost, no different brightness levels are shown. However, the three-dimensional representation of a color space, such as the common RGB or XYZ color spaces, also has a weakness: The color space is not visually uniform, which means that color differences between different colors perceived as equal do not have the same distance in the color space. Figure 2.6 c) shows the three-dimensional L*a*b* color space developed by CIE. The three coordinates L*a*b* are generated by a nonlinear transformation of the XYZ color space. Color differences perceived as identical have the same Euclidean distance ΔE in this color space. The L*-axis can take values between 0 and 100 and describes the brightness of a color, it is perpendicular to the a*-b*-plane, which describes the chromaticity. The a*-coordinate indicates the green/red and the b*-coordinate the blue/yellow area. The transformation from XYZ to L*a*b* color space is carried out with the following equations [76]:

$$\begin{aligned} L^* &= 116 f(\frac{Y}{Y_n}) - 16 \\ a^* &= 500[f(\frac{X}{X_n}) - f(\frac{Y}{Y_n})] \\ b^* &= 200[f(\frac{Y}{Y_n}) - f(\frac{Z}{Z_n})]. \end{aligned} \tag{2.3}$$

Where $f(\frac{X}{X_n})$ is defined as:

$$f(\frac{X}{X_n}) = \begin{cases} (\frac{X}{X_n})^{\frac{1}{3}}, & if \frac{X}{X_n} < (\frac{24}{116})^3 \\ \\ \frac{841}{108}\frac{X}{X_n} + \frac{16}{116}, & if \frac{X}{X_n} \geq (\frac{24}{116})^3 \end{cases}$$

Equivalently to this, $f(\frac{Y}{Y_n})$ and $f(\frac{Y}{Z_n})$ are determined.
X, Y and Z are calculated with eq. (2.1), X_n, Y_n and Z_n are the tristimulus values of a perfectly diffuse reflecting white radiator and are used for normalization. The color distance was originally defined as a simple Euclidean distance [76]:

$$\Delta E_{1,2} = \sqrt{(L_1^* - L_2^*)^2 + (a_1^* - a_2^*)^2 + (b_1^* - b_2^*)^2}. \tag{2.4}$$

This definition has been constantly developed, to the current standard CIEDE2000 or ΔE_{00} [4]:

$$\Delta E_{00} = \sqrt{\left(\frac{\Delta L'}{k_L S_L}\right)^2 + \left(\frac{\Delta C'}{k_C S_C}\right)^2 + \left(\frac{\Delta H'}{k_H S_H}\right)^2 + R_T \frac{\Delta C'}{k_C S_C} \frac{\Delta H'}{k_H S_H}} \tag{2.5}$$

The color distance ΔE_{00} [5] quantifies the differences between any two colors. It is defined so that a ΔE_{00} for any two colors is perceived by an average person as the same color difference. This function is more precisely adapted to the perception of the human eye and describes color differences in the green and the blue range in particular more accurately than the original definition $\Delta E_{1,2}$. This definition differs from the original version by the weighting functions S_L for lightness, S_C for chroma, S_H for hue and the associated weighting factors k_L, k_C and k_H [60]. When calculating the individual parameters in equation (2.5), I follow the definitions of Sharma *et al.* [78]. Since eq. (2.5) contains a large number of parameters, the individual definitions can be found in the appendix only.

Figure 2.6 a) shows the chromaticity diagram in which four color distances ΔE_{00}, related to a specific color, are drawn as an example. Furthermore, for a second color six significantly smaller color distances are drawn, Figure 2.6 b) shows an enlargement of these distances. A color distance ΔE_{00} of any two colors that is smaller than two is only perceptible at close observation for the average person [77].

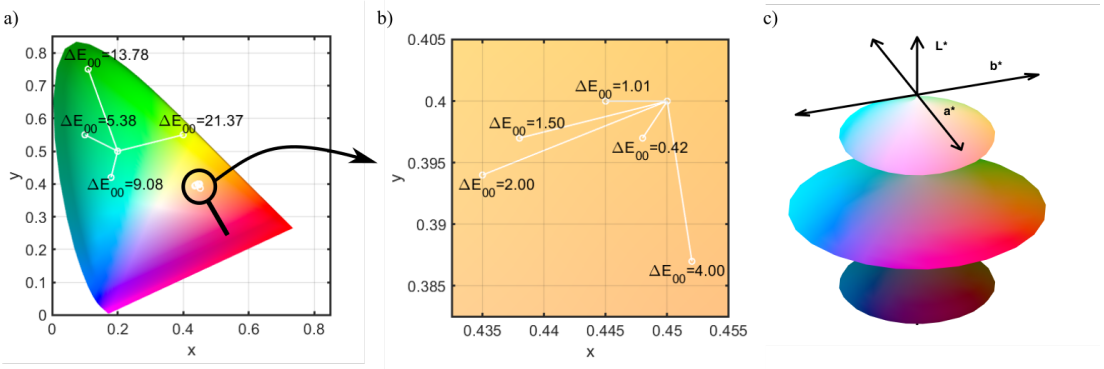

Figure 2.6: a) CIE chromaticity diagram, created with MATLAB. For two colors ($x_1 = 0.2, y_1 = 0.5$ and $x_2 = 0.45, y_2 = 0.4$) the distance ΔE_{00} to four respectively six other colors are shown. The respective colors are marked by a white circle and the color pairs are connected by a line. b) shows an enlargement of the area with the plotted colors and the respective ΔE_{00} values. c) shows the L*a*b* color space, a nonlinear transformation of the XYZ color space. Diagram created with MATLAB.

2.2 Simulation of appearance and energy yield

For the simulation of the appearance of any mixed color, I use a variation of the Clapper-Yule model [14]. This model was developed for the prediction of the reflection spectrum for halftone printed colors on paper and is based on reflection measurements of eight colors and the calculation of internal reflections. I have slightly modified this model and use it on the one hand to predict the reflectance spectrum of a PV module

whose appearance has been altered by the application of a printed layer. On the other hand, I also use the model to predict the transmission through this printed layer and thus the external quantum efficiency (EQE) of the respective PV module.
I will briefly explain the principle of halftone printing in the next paragraph, followed by a detailed explanation of the Clapper-Yule model.

2.2.1 Color mixing and printing

The color of an object depends on its reflection spectrum. In the case of colored BIPV modules where the color impression is generated by a printed layer above the solar cells, the reflection spectrum is dominated by this colored layer and the solar cell below it. For an already manufactured PV module, only the reflection spectrum of the colored layer is variable. Printed colors are created by subtractive color mixing: Each printed ink absorbs a specific part of the incident spectrum, the inks thus act as optical filters and change the reflection spectrum of the respective surface. Figure 2.7 shows the subtractive color mixing with the CMY system, which is used in this work. It contains cyan (C), magenta (M) and yellow (Y) as primary colors. If, for example, the color red is to be generated, magenta and yellow are mixed at a ratio 1:1 so that only the wavelength range perceived as red by the human eye is being reflected. If all three basic colors are mixed 1:1:1, no light is reflected and the human eye perceives the color black. [35]

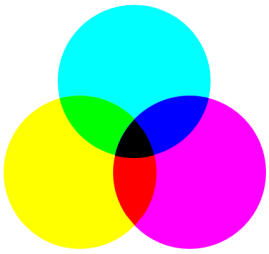

Figure 2.7: Illustration of subtractive color mixing.

The halftone printing technique creates a homogeneous color impression with three basic colors in a dot pattern [51]. The size and density of the dots varies depending on the print coverage and the required color impression. The print coverage ranges from 0% to 100% per ink and describes the area covered by the ink. A print coverage of 100% accordingly means that the entire area is covered with this ink. A mixed color is produced in halftone printing by a specific mixture of the three inks cyan (c), magenta (m) and yellow (y). The three ink screens are rotated relative to each other, typically at 30° intervals, in order to avoid conspicuous periodic screens caused by the Moiré effect [91]. Fig. 2.8 shows the rotation of the ink screens and the resulting color mixing. Depending on the selected printing parameters, there may be an overlap of certain ink spots, so that in addition to the unmixed inks, the mixed colors red (r), green (g), blue (b) and black (k) are created. Between these ink spots there are also unprinted, i.e.

white (w) areas. This results in 8 different colored elements on the surface, which are called colorants.

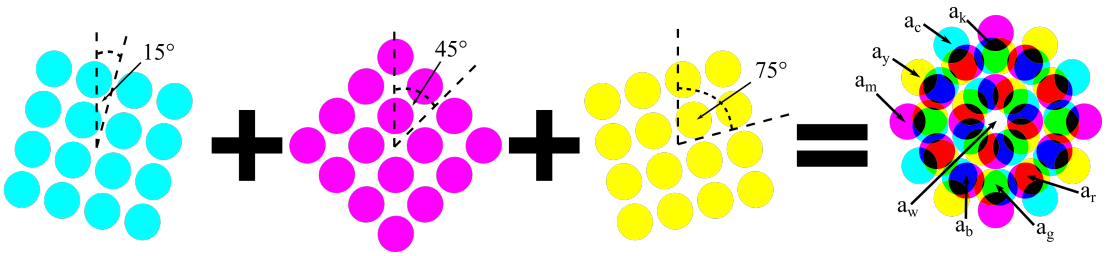

Figure 2.8: In halftone printing, the inks are rotated in relation to each other. The colors a_c, a_m, a_y, a_r, a_g, a_b, a_k and a_w, that result from the overlaying of printed inks are called colorants.

Figure 2.9 shows a) the optical microscope image and b) a camera shot of a sample printed with 50% magenta and 50% yellow, giving a terracotta-colored impression. In the microscope image, individual dots and the rotation of the ink screens are visible.

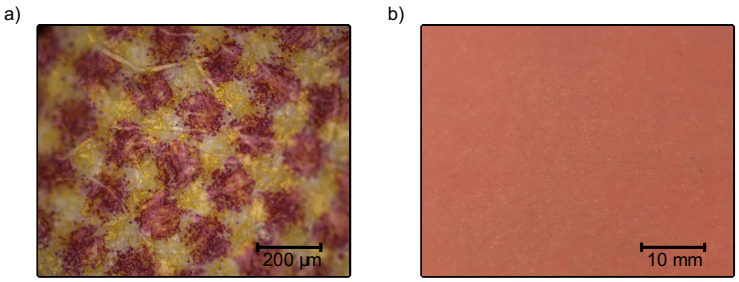

Figure 2.9: Image obtained with a) an optical microscope and b) with a digital camera of a sample printed with 50% magenta and 50% yellow.

In halftone printing, there is a discrepancy between the planned size of the ink blobs and the real size. Depending on the substrate, the ink blobs may burst more, and the resulting lower density of ink pigments makes the ink blob less opaque. This phenomenon is called ink spreading. The extent of ink spreading depends not only on the medium to be printed, but also on whether one ink is printed on top of another. A correction of the ink spreading is possible by examining on a selection of samples to what extent the real print differs from the desired print. I used the model of Hersch *et al.* [43] for this purpose. The exact procedure is explained in section 5.1.

2.2.2 The Clapper-Yule model

I use the Clapper-Yule model to determine the reflectance R_{print} of a printed PV module, based on which I can simulate the color of the module using equation (2.1). Fig. 2.10 illustrates the model when applied to a PV module. The term T_{in} describes the losses of the incident light beam during the transition from air to the imprinted medium and the propagation through the colored layer. R_{int} represents the reflections inside the medium. T_{out} describes the portion of the radiation that leaves the medium.

Using these three terms and the specular reflectance r_{spec}, R_{print} is obtained by:

$$R_{\text{print}}(\lambda) = r_{\text{spec}} + T_{\text{in}}(\lambda)R_{\text{int}}(\lambda)T_{\text{out}}(\lambda) \tag{2.6}$$

To allow a better understanding, I will derive the three terms separately in detail in the following and merge them at the end. I have adopted the following derivation from reference [43].

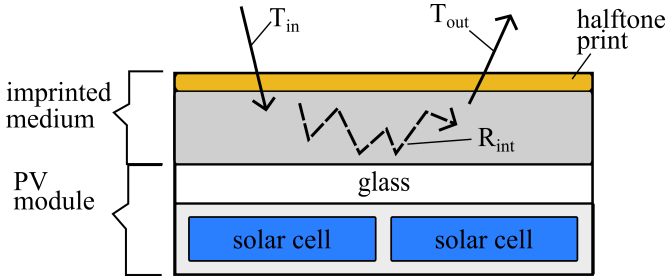

Figure 2.10: Simplified overview scheme showing the factors T_{in}, R_{int} and T_{out} for calculating the reflectance R_{print} of a printed medium using the model of Clapper and Yule. [43]

1) First, we focus on the light T_{in} entering the medium. To illustrate, I present the process in Fig. 2.11 as an example for a sample printed with cyan and magenta, each with a print coverage of 50%. Fig. 2.11 a) shows an incoming light beam at different locations on the surface of the imprinted medium. At the interface between air and the sample the specular reflectance r_{spec} occurs:

$$r_{\text{spec}} = \left(\frac{n_{\text{medium}} - n_{\text{air}}}{n_{\text{medium}} + n_{\text{air}}}\right)^2, \tag{2.7}$$

with the indices of refraction $n_{\text{air}} = 1$ of air and n_{medium} of the respective medium. The transmission through the colorant j depends on the surface coverage a_j and the wavelength λ-dependent transmission $t_j(\lambda)$. In combination with the surface reflectance, this results in an attenuation of an incident light beam by a factor of $(1 - r_{\text{spec}})a_j t_j(\lambda)$. Fig. 2.11 b) illustrates the close-up of a sample printed with cyan and magenta each with 50% print coverage. Four different colored areas are generated: on the top left part there is only the cyan ink, on the top right there is no ink, on the bottom left cyan and magenta overlap, and on the bottom right there is only the magenta ink. The probability P_c for a light ray to hit the cyan-colored area a_c is the print coverage of cyan multiplied by the proportion of the area that is not magenta: $P_c = c \cdot (1 - m) = 0.5 \cdot (1 - 0.5) = 0.25$. The area fraction on which only the cyan ink is present is equal to the probability: $a_j = P_c = 0.25$. Accordingly, the probabilities are determined for the magenta area P_m, the blue area P_b where cyan and magenta overlap, and the white area P_w where no ink is present:

$$P_m = m \cdot (1 - c) \qquad P_b = c \cdot m \qquad P_w = (1 - c)(1 - m), \tag{2.8}$$

where the indices represent the respective colorant.

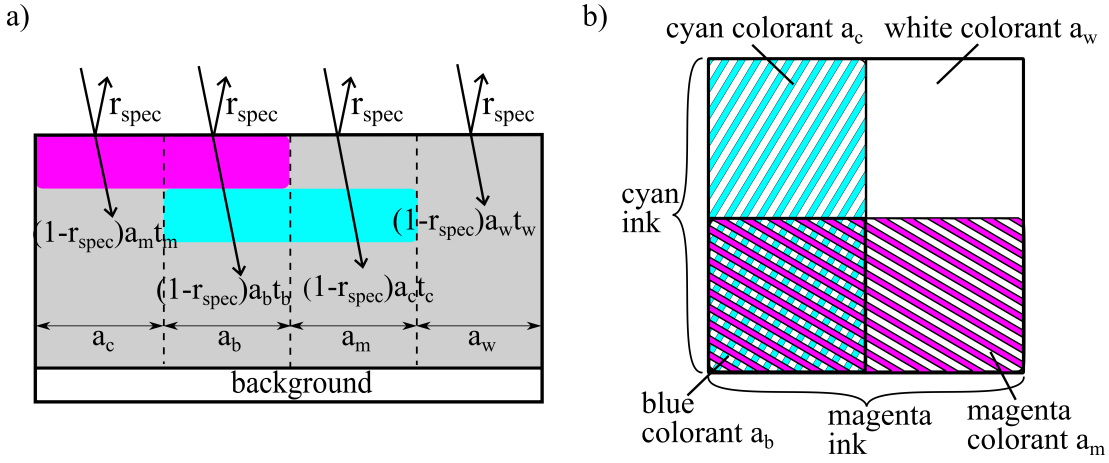

Figure 2.11: Simplified scheme of incoming light rays into the printed medium (a) and the top view of the printed medium (b). [43]

The probability for a light ray to hit a certain colorant thus defines the surface coverage of this colorant, it is $a_j = P_j$. If all three inks are used instead of just two, the result will be eight different colorants (see Fig. 2.8). The calculation of the probabilities, or the proportions of the surface of the respective colorants are calculated according to the same principle as in eq. (2.8):

$$\begin{aligned} a_\mathrm{w} &= (1-c)(1-m)(1-y) & a_\mathrm{c} &= c(1-m)(1-y) \\ a_\mathrm{m} &= (1-c)m(1-y) & a_\mathrm{y} &= (1-c)(1-m)y \\ a_\mathrm{r} &= (1-c)my & a_\mathrm{g} &= c(1-m)y \\ a_\mathrm{b} &= cm(1-y) & a_\mathrm{k} &= cmy \end{aligned} \tag{2.9}$$

These equations are called Demichel's equations [19]. Based on Fig. 2.11 and equation (2.9) it follows with the incoming irradiation $E_0(\lambda)$:

$$T_\mathrm{in}(\lambda) = (1 - r_\mathrm{spec}) \sum_{j=1}^{8} a_\mathrm{j} t_\mathrm{j}(\lambda) \cdot E_0(\lambda). \tag{2.10}$$

2) The next aspect we consider is the internal reflection R_int as shown in Fig. 2.12. After passing the halftone layer, the incoming light T_{in} receives the diffuse scattering $r_g(\lambda)$ in the substrate and is reflected back at the boundary layer with the internal, angle- and wavelength-independent reflectance r_{int}. If we also take into account the halftone layer, the radiation $E_1(\lambda)$ after one reflection cycle results in

$$E_1(\lambda) = T_\mathrm{in}(\lambda) r_\mathrm{g}(\lambda) \sum_{j=1}^{8} (a_j t_j(\lambda)^2) r_\mathrm{int} r_\mathrm{g}(\lambda). \tag{2.11}$$

The consideration of infinite reflection cycles forms a geometric series and leads to the radiation $E_{\mathrm{R}}(\lambda)$ reflected from the printed medium [11]:

$$\begin{aligned} E_{\mathrm{R}}(\lambda) &= T_{\mathrm{in}}(\lambda) r_{\mathrm{g}}(\lambda) \sum_{k=1}^{\infty} \left[\sum_{j=1}^{8} (a_j t_j(\lambda)^2) r_{\mathrm{int}} r_{\mathrm{g}}(\lambda) \right]^k \\ &= \frac{T_{\mathrm{in}}(\lambda) r_{\mathrm{g}}(\lambda)}{1 - r_{\mathrm{g}}(\lambda) r_{\mathrm{int}} \sum_{j=1}^{8} a_j t_j(\lambda)^2}. \end{aligned} \tag{2.12}$$

Thus, it follows for the factor of internal reflections:

$$R_{\mathrm{int}}(\lambda) = \frac{r_{\mathrm{g}}(\lambda)}{1 - r_{\mathrm{g}}(\lambda) r_{\mathrm{int}} \sum_{j=1}^{8} a_j t_j(\lambda)^2}. \tag{2.13}$$

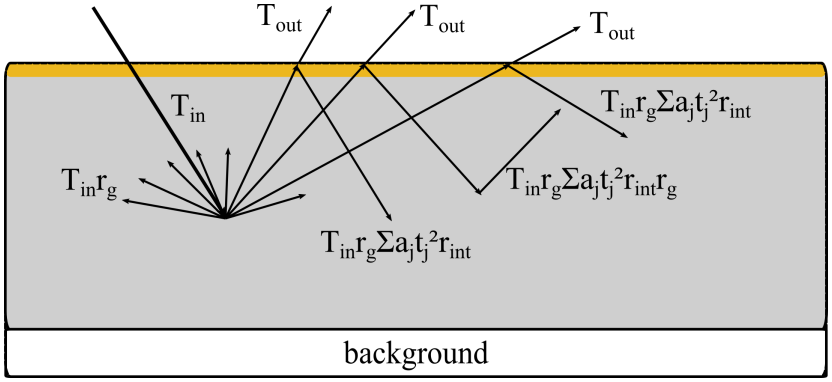

Figure 2.12: Simplified scheme for incident radiation T_{in}, that is reflected in the substrate by Lambertian reflection r_{g} and internal reflection r_{int}. The size of the arrows has no relation to the respective photon flux. [43]

3) The factor T_{out} describes the portion of the radiation that leaves the substrate:

$$T_{\mathrm{out}}(\lambda) = (1 - r_{\mathrm{int}}) \sum_{j=1}^{8} a_{\mathrm{j}} t_{\mathrm{j}}(\lambda). \tag{2.14}$$

Computation of the reflectance R_{print} of the imprinted medium

Using equations (2.10), (2.13) and (2.14) we get the total reflectance of the printed substrate:

$$\begin{aligned} R_{\mathrm{print}}(\lambda) &= r_{\mathrm{spec}} + T_{\mathrm{in}}(\lambda) R_{\mathrm{int}}(\lambda) T_{\mathrm{out}}(\lambda) \\ &= r_{\mathrm{spec}} + \frac{(1 - r_{\mathrm{spec}}) r_{\mathrm{g}}(\lambda) \left[\sum_{j=1}^{8} a_{\mathrm{j}} t_{\mathrm{j}}(\lambda) \right]^2 (1 - r_{\mathrm{int}})}{1 - r_{\mathrm{int}} r_{\mathrm{g}}(\lambda) \left[\sum_{j=1}^{8} a_{\mathrm{j}} t_{\mathrm{j}}^2(\lambda) \right]}. \end{aligned} \tag{2.15}$$

The two reflections r_{spec} and r_{int} can be calculated numerically via the Fresnel equations [31]. For the determination of the parameters $t_j(\lambda)$ only the reflectance $R_j(\lambda)$ of the material printed with colorant j must be measured. Using the measured reflection

spectrum R_w of the unprinted medium simplifies the equation to

$$R_\mathrm{w}(\lambda) = r_\mathrm{spec} + \frac{(1-r_\mathrm{spec})r_\mathrm{g}(\lambda)\left[a_\mathrm{w}t_\mathrm{w}(\lambda)\right]^2(1-r_\mathrm{int})}{1-r_\mathrm{int}r_\mathrm{g}(\lambda)\left[a_\mathrm{w}t_\mathrm{w}^2(\lambda)\right]}$$
$$\overset{a_\mathrm{w}=t_\mathrm{w}=1}{=} r_\mathrm{spec} + \frac{(1-r_\mathrm{spec})r_\mathrm{g}(\lambda)(1-r_\mathrm{int})}{1-r_\mathrm{int}r_\mathrm{g}(\lambda)}$$

and rearranging the equation according to the Lambertian reflection $r_\mathrm{g}(\lambda)$ results in

$$r_\mathrm{g}(\lambda) = \frac{R_\mathrm{w}(\lambda) - r_\mathrm{spec}}{(1-r_\mathrm{int})(1-r_\mathrm{spec}) + r_\mathrm{int}(R_\mathrm{w}(\lambda) - r_\mathrm{spec})}. \tag{2.16}$$

I use the measured reflectance spectrum of the individual colorant j:

$$R_\mathrm{j}(\lambda) = r_\mathrm{spec} + \frac{(1-r_\mathrm{spec})r_\mathrm{g}(\lambda)a_\mathrm{j}^2t_\mathrm{j}^2(\lambda)(1-r_\mathrm{int})}{1-r_\mathrm{int}r_\mathrm{g}(\lambda)a_\mathrm{j}t_\mathrm{j}^2(\lambda)}$$
$$\overset{a_\mathrm{j}=1}{=} r_\mathrm{spec} + \frac{(1-r_\mathrm{spec})r_\mathrm{g}(\lambda)t_\mathrm{j}^2(\lambda)(1-r_\mathrm{int})}{1-r_\mathrm{int}r_\mathrm{g}(\lambda)t_\mathrm{j}^2(\lambda)}$$

and obtain the transmittance of the certain colorants by rearranging eq. 2.15:

$$t_j(\lambda) = \sqrt{\frac{R_j(\lambda) - r_\mathrm{spec}}{r_\mathrm{g}(\lambda)\left[(R_j(\lambda) - r_\mathrm{spec})r_\mathrm{int} + (1-r_\mathrm{int})(1-r_\mathrm{spec})\right]}}. \tag{2.17}$$

2.2.3 Simulation of the external quantum efficiency

The PV energy yield depends on the PV module's efficiency, which is given by its short-circuit current density J_SC, the open-circuit voltage V_OC and fill factor. The short-circuit current density

$$J_{SC} = q\int_0^\infty d\lambda\Phi(\lambda)EQE(\lambda) \tag{2.18}$$

depends on the module's external quantum efficiency (EQE), the elementary charge q and the wavelength λ-dependent incoming photon flux $\Phi(\lambda)$ [84]. Figure 2.13 depicts a cross section of a CoTex PV module which is irradiated from above. The photon flux reaching the PV module's surface is $\Phi_0(\lambda)$, e.g. the photon flux of the AM1.5G spectrum [15]. The photon flux $\Phi_1(\lambda)$ on the left hand side describes the photon flux that enters the PV module and is therefore reduced by the reflection at the interface from air to the glass. In addition to this reflection, the photon flux $\Phi_2(\lambda)$ on the right hand side is also reduced by the absorption in the Colored Textiles (CoTex) layer and the reflection at the interface between the CoTex layer and the glass. Consequently, coloring a PV module mainly decreases its J_SC, because the photon flux $\Phi_2(\lambda)$ is always smaller than the photon flux $\Phi_1(\lambda)$ which reaches the solar cell of a standard PV module.

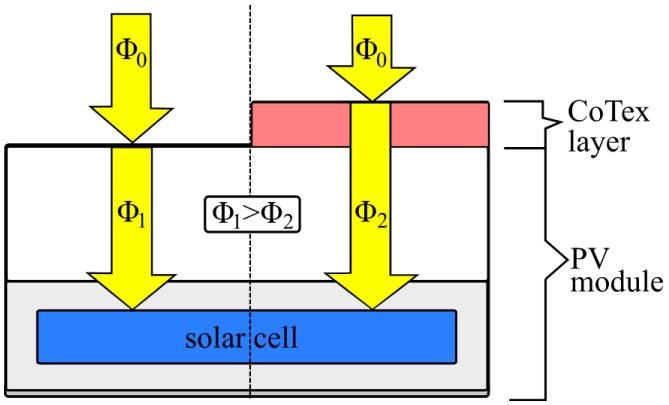

Figure 2.13: Schematic illustration of the photon flux in a standard module (left, $\Phi_1(\lambda)$) and a CoTex module (right, $\Phi_2(\lambda)$) to show that the photon flux arriving at the solar cell is always lower in the CoTex module than in the standard module due to the additional layer.

To show that the J_{SC} is sufficient to describe solar cells or PV modules in terms of energy yield, we consider the single diode model, shown in Fig. 2.14 a), to characterize a solar cell. According to Kirchhoff's laws, the current I is

$$I = I_{Ph} - I_D - I_{sh} \tag{2.19}$$

with the light-generated current I_{Ph}, the diode current I_D and the shunt current I_{sh}. For an ideal diode the following applies:

$$I_D = I_0 \left[\exp\left(\frac{q(V + IR_s)}{nkT}\right) - 1 \right] \tag{2.20}$$

with the diode ideality factor $n = 1$, the saturation current I_0, the elementary charge q, the Boltzmann constant k, the voltage V and the series resistance R_s. Also derived from Kirchhoff's laws, the current I_{sh} can be determined by

$$I_{sh} = \frac{V + IR_s}{R_{sh}} \tag{2.21}$$

If eq. (2.20) and (2.21) are used in eq. (2.19), the generated current in an ideal diode is:

$$I = I_{Ph} - I_0 \left[\exp\left(\frac{q(V + IR_s)}{kT}\right) - 1 \right] - \frac{V + IR_s}{R_{sh}} \tag{2.22}$$

Figure 2.14 b) shows the relationship between the power output at the P_{MPP} and the I_{SC}, derived by calculating the I-V curve of a solar cell using eq. (2.22). All parameters are kept constant except for the incident photocurrent I_{Ph}, which is varied between 0 and 46.6 mA, corresponding to the maximum photo current for the AM1.5G spectrum on a fixed area of 1 cm^2. The result shows a linear relationship between I_{SC} and P_{MPP}.

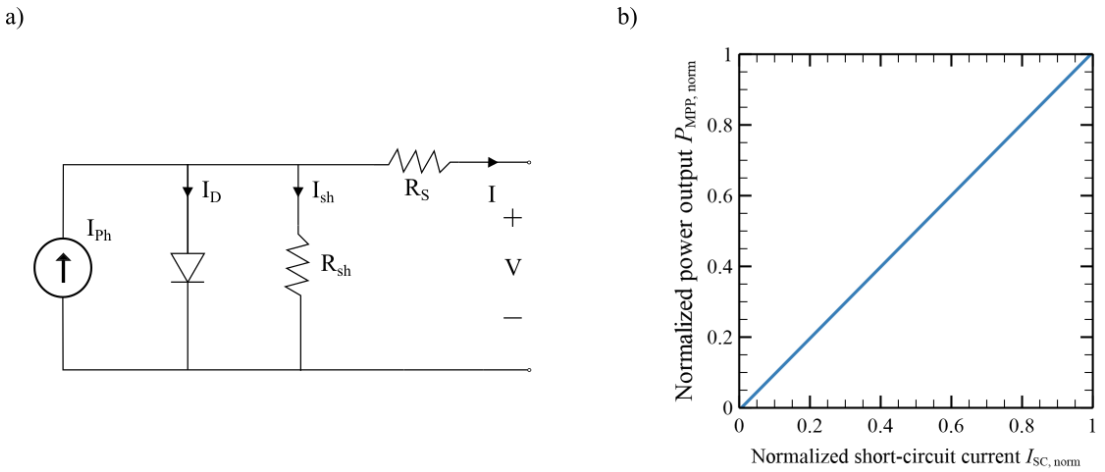

Figure 2.14: a) Equivalent circuit diagram of the single diode model. b) Relationship of I_{SC} and P_{MPP}, calculated with the single diode model. The values for both, I_{SC} and P_{MPP}, are normalized to their maximum.

The proportional correlation between output power of a solar cell or module and J_{SC} can be approximated by

$$P_{\mathrm{MPP}} \approx \frac{P_{\mathrm{MPP,max}}}{J_{\mathrm{SC,max}}} \cdot J_{SC}(I_{\mathrm{Ph}}). \tag{2.23}$$

Using Eq. (2.18) and (2.23), we can thus estimate the energy yield E from a measured or simulated EQE:

$$E = \int dt P_{\mathrm{MPP}}(t) \tag{2.24}$$

It follows that by altering the appearance using CoTex layers, the J_{SC} in particular is reduced. For simplification, I thus assume that module output power and J_{SC} are proportional, i.e. that open-circuit voltage and fill factor change only negligibly due to the application of CoTex layers. I calculate J_{SC} from the simulated EQE as described in the following section.

For the simulation of the EQE of individually colored PV modules I use a variation of the Clapper-Yule model [14] for the simulation of the reflection spectra (see section 2.2.2). Instead of the reflection, I now consider the relative transmittance T_j of the colored layer:

$$T_j(\lambda) = \frac{EQE_j(\lambda)}{EQE_{ref}} \tag{2.25}$$

where $EQE_j(\lambda)$ is the EQE of a PV modules colored with colorant j and EQE_{ref} is the measured EQE of a single-cell module without a colored layer.

The different absorption behavior of the various inks make the adaptation of the equations of the Clapper-Yule model more complex. Unfortunately, explaining all the internal processes in detail was beyond the scope of this dissertation. Therefore, I use an approximation by replacing the parameters r_s and r_{int} in equation 2.15 with wisely

chosen fit parameters f_1 and f_2 to determine the relative transmittance $T_{print}(\lambda)$

$$T_{print}(\lambda) = f_1 + \frac{(1-f_1)r_{\mathrm{g}}(\lambda)\left[\sum_{j=1}^{2^k} a_j r_j(\lambda)\right]^2 (1-f_2)}{1 - f_2 r_{\mathrm{g}}(\lambda)\left[\sum_{j=1}^{2^k} a_j r_j^2(\lambda)\right]} \tag{2.26}$$

which yields to

$$\begin{aligned} r_{\mathrm{g}}(\lambda) &= \frac{T_{\mathrm{w}}(\lambda) - f_1}{1 + f_2 T_{\mathrm{w}}(\lambda) - f_1 - f_2} \\ t_j(\lambda) &= \sqrt{\frac{1}{r_{\mathrm{g}}(\lambda)} \cdot \frac{T_j(\lambda) - f_1}{f_2(T_j(\lambda) - f_1) + (1-f_2)(1-f_1)}} \end{aligned} \tag{2.27}$$

for the transmittances of each colorant $t_j(\lambda)$ and the internal reflection $r_{\mathrm{g}}(\lambda)$. Multiplying the simulated transmittance of the colored layer with EQE_{ref} gives the EQE of the colored module:

$$EQE_{\mathrm{print}} = T_{\mathrm{print}}(\lambda) \cdot EQE_{\mathrm{ref}}(\lambda). \tag{2.28}$$

I use the measured $EQEs$ of the eight colorants to determine f_1 and f_2, more on this in chapter 5.

2.3 Energy yield prognosis

The energy yield prognosis for photovoltaic modules aims to predict the energy yield of a single PV module or an entire PV park for a certain period of time. For this purpose, a yield calculation of the photovoltaic module is performed based on module characteristics, location and orientation of the PV module as well as climate data. Module characteristics include, for example, solar cell type, material information, I-V curve parameters, and temperature coefficients. These module characteristics are usually specified in the data sheet, but can also be measured. Climate data includes irradiance, ambient temperature, wind speed, and humidity. It is common to use a Typical Meteorological Year (TMY) for which typical months are selected from measurement data for a specific location for a period of at least 10 years based on special criteria [40]. Usually hourly averaged measurement data is used, but basically the yield calculation is also possible for smaller and larger time intervals. It is assumed that the weather of the past is a good approximation for the weather in the future [3]. Therefore, the yield calculation with the TMY becomes a yield forecast for the future. Figure 2.15 shows the procedure for the yield prediction of colored PV modules that I use in this work. The green fields contain measured data, which were either measured by me or colleagues at ISFH, at the Institute of Meteorology and Climatology Hannover (IMUK) or taken from open sources. The orange fields contain sections that have been determined by established computational models. The blue fields mark sections that are new for the yield prediction or at least contain improvements that were developed within

the scope of this work. In this section I will cover all fields in this scheme, only the simulation of *EQE* of colored PV modules will be addressed in the second section.

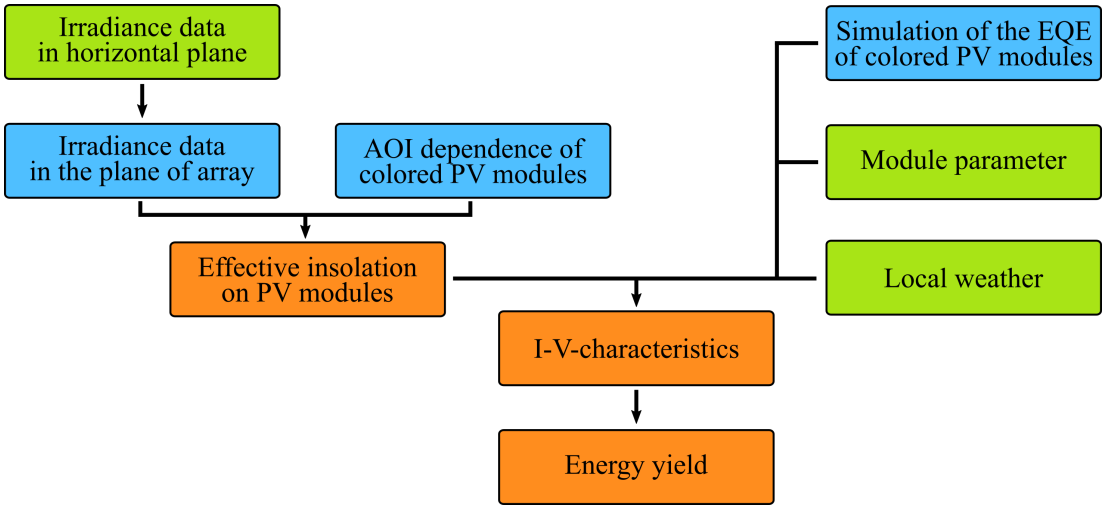

Figure 2.15: Scheme for the energy yield prediction of colored PV modules. The green fields represent measured data, the orange fields represent methods or functions that are commonly used and that I apply. Methods I developed or further developed are listed in the blue fields: the simulation of the EQE of colored PV modules, the transposition of irradiance data into the plane of array and Angle of Incidence (AOI) dependence of colored PV modules.

When I evaluate the accuracy of the models and methods used, I consider the arithmetic mean value $\overline{x}$, the standard deviation σ and the relative root-mean-square error e. The calculation of these quantities is done by

$$\overline{x} = \frac{\sum_{i=1}^{N} x_i}{N}, \quad \sigma = \sqrt{\frac{\sum_{i=1}^{N}(x_i - \overline{x})^2}{N}}, \quad e = \frac{\sqrt{\frac{\sum_{i=1}^{N}(x_i - y_i)^2}{N}}}{\overline{x}}. \tag{2.29}$$

Here x_i is the simulated value i, N is the number of simulated values x_i, and y_i is a reference value. In this work, y_i is usually the measured value. In this section, I will briefly discuss the radiation incident on the PV module and explain the calculation of Ground View Factor (GVF), which I use to estimate the radiation reflected from the ground onto a tilted PV module. Module parameters, the models used to convert and calculate irradiation in the inclined plane, and the model used to determine the module temperature will be described in the methods section.

2.3.1 Irradiation

Insolation has a dominant impact on the PV energy yield. Measured irradiance is widely available for many locations (PVGIS [45], EUMETSAT, etc.). Usually the Global Horizontal Irradiance (GHI) and sometimes also the Diffuse Horizontal Irradiance (DHI) or Direct Normal Irradiance (DNI) is provided. The GHI includes direct and diffuse solar irradiance incident on a horizontal sensor (Fig. 2.16 a). Reflection from the ground is not included. The DNI consists of the irradiance incident on a sensor oriented perpendicular to the direction of incidence (Fig.2.16 b).

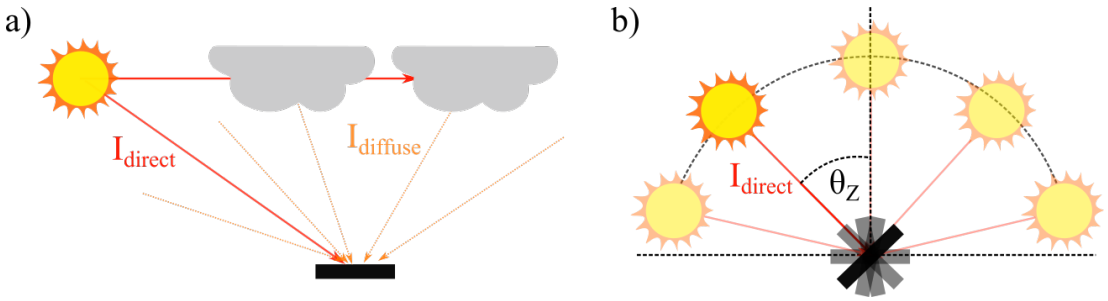

Figure 2.16: a) The total direct (I_{direct}) and diffuse (I_{diffuse}) irradiance incident on a horizontal sensor represents the GHI. If the GHI is reduced by the direct component, the DHI remains. b) The DNI accounts for the direct irradiance on a sensor oriented perpendicular to the incoming irradiance.

If two of these components are known, the third can be calculated in conjunction with the zenith angle of the sun θ_Z using the following relationship:

$$GHI = DHI + DNI \cos\theta_Z. \tag{2.30}$$

The horizontal diffuse irradiance has to be converted into the Plane of Array (POA) of the tilted PV module. The methods used to do this are presented in chapter 6.1.2. The direct light component I_{direct} incident on a PV module is determined straight from the DNI via the geometric relationship between the position of the sun and POA. For this purpose, the AOI θ shown in Figure 2.17 is used:

$$I_{\text{direct}} = DNI \cdot \cos\theta \tag{2.31}$$

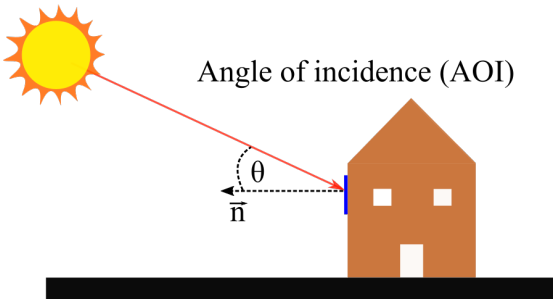

Figure 2.17: The AOI θ is given by the position of the sun and the normal vector $\vec{n}$ of the PV module.

2.3.2 Ground view factor

View factors describe the radiation transfer between any two surfaces. The view factor VF_{12} of surface A_1 to surface A_2 provides the ratio between the radiation flux Φ_{12} emitted by A_1 and hitting A_2 in relation to the total radiation Φ_1 emitted by A_1:

$$VF_{12} = \frac{\Phi_{12}}{\Phi_1} = \frac{\Phi_{12}}{\pi L A_1} \tag{2.32}$$

It is assumed that A_1 emits the radiance L diffusely in equal parts in all directions of the half dome. I use the view factor to determine the fraction of the radiation reflected

from the ground that hits a PV module. In the following, I derive from the general view factor for arbitrary surfaces the integral for the case of the GVF for vertically mounted PV modules considered in this work. Figure 2.18 shows the view factor VF_{12} from the infinitesimal surface element dA_1 of surface A_1 to the distance s apart surface element dA_2 of surface A_2. The orientation of the surfaces to each other is described by the angles β_1 and β_2 to the respective surface normals $\vec{n}_1$ and $\vec{n}_2$. The transferred radiation $d^2\Phi_{12}$ from dA_1 to dA_2 with radiance L follows the inverse-square law [49]:

$$d^2\Phi_{12} = L\frac{\cos\beta_1 \cos\beta_2}{s^2} dA_1 dA_2 \tag{2.33}$$

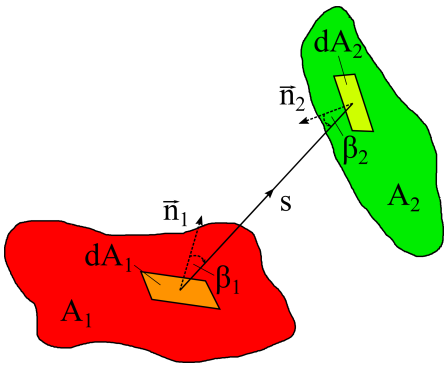

Figure 2.18: The radiation transfer between two infinitesimal surface elements dA_1 and dA_2 of any two surfaces A_1 and A_2 oriented to their junction line of distance s by the angles β_1 and β_2 is described by the view factor VF_{12}.

Figure 2.19 shows the case where we are dealing with a PV module mounted on a façade. We consider a point $P_1 = (x_1 \,|\, y_1 \,|\, 0)$, which is in the x-y plane and thus on the ground and a point $P_2 = (0 \,|\, y_2 \,|\, z_2)$ in the y-z plane representing the PV module on the façade. The angles β_1 and β_2 between the vector $\overrightarrow{P_1P_2}$ and the normal vectors $\vec{n_1} = (0 \,|\, 0 \,|\, 1)$ and $\vec{n_2} = (1 \,|\, 0 \,|\, 0)$ are calculated as follows:

$$\begin{aligned}
\cos\beta_1 &= \frac{|\overrightarrow{P_1P_2} \cdot \vec{n_1}|}{|\overrightarrow{P_1P_2}| \cdot |\vec{n_1}|} = \frac{z_2}{\sqrt{x_1^2 + (y_1 - y_2)^2 + z_2^2}} = \frac{z_2}{s} \\
\cos\beta_2 &= \frac{|\overrightarrow{P_1P_2} \cdot \vec{n_2}|}{|\overrightarrow{P_1P_2}| \cdot |\vec{n_2}|} = \frac{x_1}{\sqrt{x_1^2 + (y_1 - y_2)^2 + z_2^2}} = \frac{x_1}{s},
\end{aligned} \tag{2.34}$$

where s is the distance between point P_1 and P_2. With equation 2.33 and 2.34 follows for the case of radiation transfer between two infinitesimal surfaces perpendicular to each other:

$$d^2\Phi_{12} = L\frac{x_1 z_2}{s^4} dA_1 dA_2 = L\frac{x_1 z_2}{(x_1^2 + (y_1 - y_2)^2 + z_2^2)^2} dA_1 dA_2. \tag{2.35}$$

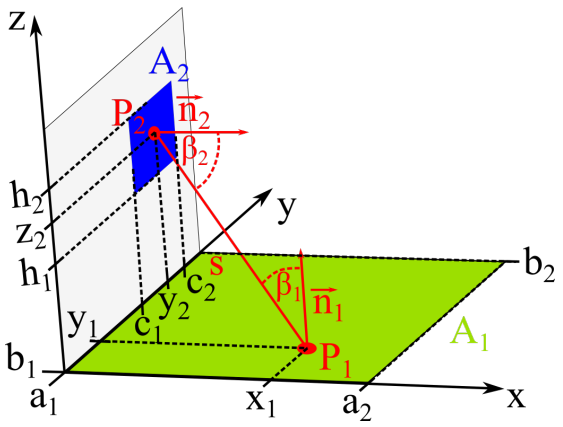

Figure 2.19: Scheme for calculating the ground view factor for two areas A_1 and A_2 that are perpendicular to each other.

By calculating the integral, we obtain the radiation transfer between the finite areas A_1 and A_2:

$$\Phi_{12} = \int_{a_1}^{a_2} \int_{b_1}^{b_2} \int_{c_1}^{c_2} \int_{h_1}^{h_2} L \frac{xz}{(x^2 + (y_1 - y_2)^2 + z^2)^2} dx dy_1 dy_2 dz \tag{2.36}$$

where a_1, a_2, b_1, b_2, c_1, c_2, h_1 and h_2 denote the boundaries of the surfaces A_1 and A_2 and thus also of the integrals. We need the view factor Φ_{21} from the PV module to the ground surface, thereby we use the reciprocity relation [88]:

$$\Phi_{21} = \frac{A_1}{A_2} \Phi_{12}. \tag{2.37}$$

This results in the ground view factor from a PV module (area A_2) to the ground (area A_1):

$$GVF = \frac{\Phi_{21}}{\pi L A_1} = \frac{1}{\pi A_2} \int_{a_1}^{a_2} \int_{b_1}^{b_2} \int_{c_1}^{c_2} \int_{h_1}^{h_2} \frac{xz}{(x^2 + (y_1 - y_2)^2 + z^2)^2} dx dy_1 dy_2 dz \tag{2.38}$$

To avoid the complex and time-consuming computation of the four-dimensional integral, I use the solution of Ehlert and Smith to compute the view factor between mutually perpendicular rectangular surfaces [26]:

$$GVF = \frac{1}{A_2} \sum_{l=1}^{2} \sum_{k=1}^{2} \sum_{j=1}^{2} \sum_{i=1}^{2} \Big[(-1)^{l+k+j+i} G(a_i, b_j, c_k, h_l) \Big]. \tag{2.39}$$

The function G is defined as:

$$G = \frac{1}{2\pi} \left[\xi\eta \arctan \frac{\xi}{\eta} - \frac{1}{4} (\eta^2 - \xi^2) \ln (\eta^2 + \xi^2) \right], \tag{2.40}$$

using

$$\xi = b - c \qquad \eta = \sqrt{a^2 + h^2}. \tag{2.41}$$

2.3.3 Calculation of the ground diffuse irradiation

The diffuse reflection of the ground results from the albedo ρ, i.e. the reflectivity of the ground, and the GHI hitting the ground. To calculate the proportion I_{Ground} of the reflected radiation that reaches a PV module, the view factor from equation (2.38), which was introduced in this work, is used:

$$I_{Ground} = GHI \cdot \rho \cdot GVF \tag{2.42}$$

If the area in front of the PV modules has different albedo ρ_i of the number i, the respective GVF_i must be determined for areas A_i:

$$I_{Ground,\,GVF} = GHI \cdot \sum_{k=1}^{i} (\rho_k \cdot GVF_k) \tag{2.43}$$

where $GVF = \sum_{k=1}^{i} GVF_k$ applies.
Figure 2.20 shows the situation when part of the open area A in front of the PV modules is temporarily shaded. In this area, only DHI is reflected. The shaded area $A_{sh.}$ results from the height h and width b of the object responsible for the shading and the respective elevation angle θ_{el} of the sun:

$$A_{sh.}(\theta_{el}) = \frac{h}{\tan \theta_{el}} \cdot b \tag{2.44}$$

The remaining portion of A represents the unshaded area $A_{unsh.}$:

$$A_{unsh.}(\theta_{el}) = A - A_{sh.}(\theta_{el}) \tag{2.45}$$

This results in

$$\begin{aligned} I_{Ground,\,GVF\,sh.} &= I_{Ground,\,shaded} + I_{Ground,\,unshaded} \\ &= GHI \cdot \sum_{k=1}^{i} (\rho_k \cdot GVF(A_{unsh.})_k) + DHI \cdot \sum_{k=1}^{i} (\rho_k \cdot GVF(A_{sh.})_k \end{aligned} \tag{2.46}$$

for the calculation of the fraction of ground reflection that falls on a PV module attached to the façade.

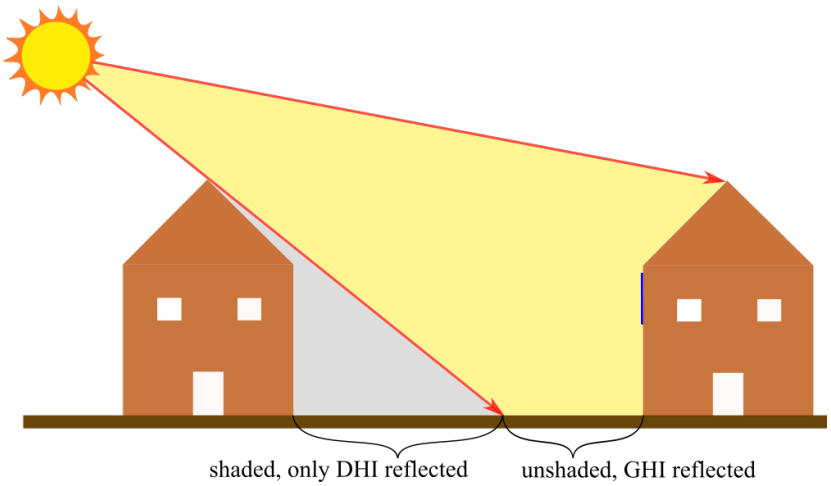

Figure 2.20: Objects in the surroundings shade the surface in front of a façade module. DHI is reflected from the shaded surface, GHI from the unshaded surface.

In the established calculation of ground reflection for vertical PV modules, an infinitely extended area in front of the façade is assumed. The area A_2 of the PV module remains the same, but the limits of the area of the ground turn into $a_1 = 0$, $a_2 = \infty$, $b_1 = -\infty$ and $b_2 = \infty$. With these limits, the result for the integral in equation (2.36) is:

$$\begin{aligned}\Phi_{12} &= \int_0^{\infty} dx \int_{-\infty}^{\infty} dy_1 \int_{c_1}^{c_2} dy_2 \int_{h_1}^{h_2} dz L \frac{xz}{(x^2 + (y_1 - y_2)^2 + z^2)^2} \\ &= L \int_{c_1}^{c_2} dy_2 \int_{h_1}^{h_2} dz z \int_0^{\infty} dx x \underbrace{\int_{-\infty}^{+\infty} dy_1 \frac{1}{(x^2 + (y_1 - y_2)^2 + z^2)^2}}_{:= \mathrm{int}_{\mathrm{dy}_1}}\end{aligned}$$

in a first step, the rearrangement of the terms simplifies the calculation of the integral $\mathrm{int}_{\mathrm{dy}_1}$:

$$\begin{aligned}\mathrm{int}_{\mathrm{dy}_1} &= \frac{1}{2}\left[\frac{y_1 - y_2}{(x^2 + z^2)(x^2 + (y_1 - y_2)^2 + z^2)^2} + \frac{\arctan \frac{y_1 - y_2}{\sqrt{x^2 + z^2}}}{(x^2 + z^2)^{3/2}}\right]_{-\infty}^{+\infty} \\ &= \frac{1}{2(x^2 + z^2)^{3/2}}\left[\arctan \frac{y_1 - y_2}{\sqrt{x^2 + z^2}}\right]_{-\infty}^{+\infty} = \frac{\pi}{2(x^2 + z^2)^{3/2}}.\end{aligned}$$

Substituting the result into the above equation yields:

$$\begin{aligned}\Phi_{12} &= \frac{\pi L}{2} \int_{c_1}^{c_2} dy_2 \int_{h_1}^{h_2} dz z \int_0^{\infty} dx \frac{x}{(x^2 + z^2)^{3/2}} = \frac{\pi L}{2} \int_{c_1}^{c_2} dy_2 \int_{h_1}^{h_2} dz z \left[\frac{-1}{\sqrt{x^2 + z^2}}\right]_0^{\infty} \\ &= \frac{\pi L}{2} \int_{c_1}^{c_2} dy_2 \int_{h_1}^{h_2} dz \frac{z}{z} = \frac{\pi L}{2}(c_2 - c_1)(h_2 - h_1) = \frac{\pi L A_2}{2}.\end{aligned}$$

Using this term for the GVF in equation (2.38) leads to:

$$GVF = \frac{\Phi_{12}}{\pi L A_2} = \frac{\pi L A_2}{2\pi L A_2} = \frac{1}{2}.$$

This GVF for an infinitely extended open area in front of the PV module results in the so far established formula for the calculation of the ground reflection for vertically mounted PV modules:

$$I_{Ground,\,Std.} = \frac{1}{2}\, GHI \cdot \rho_{mean}, \tag{2.47}$$

where ρ_{mean} is an average albedo of the ground surface.

2.3.4 Calculation of the energy yield

Figure 2.21 shows the typical Current-Voltage (I-V) characteristic of a solar cell that I use to calculate the yield of photovoltaic modules or solar cells. Five parameters that can be read from the I-V characteristic measured at Standard Test Conditions (STC) are used to calculate the I-V characteristic for arbitrary temperatures and irradiations. These parameters are the short-circuit current I_{SC}, the open-circuit voltage V_{OC} and the current I_{MPP}, voltage V_{MPP} and power P_{MPP} at the maximum power point.

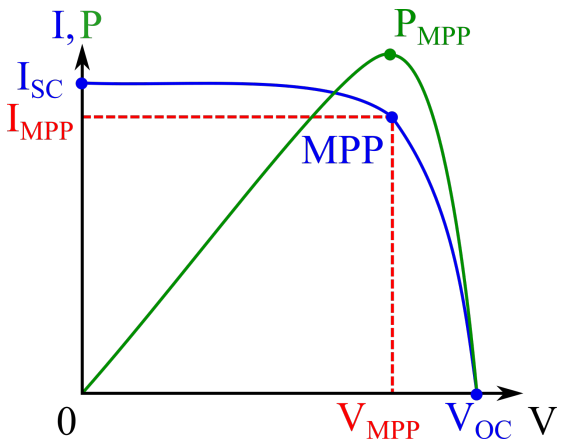

Figure 2.21: Characteristic curve of a solar cell, the important parameters I_{SC}, V_{OC}, I_{MPP}, V_{MPP} and P_{MPP} are marked.

The energy yield in a certain time period is given by the integral of the output power

$$P_{\mathrm{MPP}} = I_{\mathrm{MPP}} \cdot V_{\mathrm{MPP}} \tag{2.48}$$

over the respective period, as indicated in equation (2.24). I use the Sandia Array Perfomance Model [54] to determine I_{MPP} and V_{MPP}. The respective equations (A.14 - A.21) can be found in appendix A.4.
An addition occurs when calculating the energy yield for CoTex modules. There, I calculate the angle of incidence (AOI) θ dependent relative transmission through the

colored layers of the CoTex module

$$\tau_{\text{rel.}}(\theta) = \frac{P_{\text{MPP, outdoor}}}{P_{\text{MPP, STC}}} \tag{2.49}$$

using the measured values from the outdoor $P_{\text{MPP, outdoor}}$ and the measurement $P_{\text{MPP, STC}}$ at standard test conditions (STC) of a CoTex module and multiply it with equation (2.48) to estimate the energy yield of an arbitrary CoTex module:

$$P_{\text{MPP, CoTex}}(\theta) = I_{\text{MPP}} \cdot V_{\text{MPP}} \cdot \tau_{\text{rel.}}(\theta) \tag{2.50}$$

After providing the theoretical background for the individual aspects of this thesis, I will move on to consider the current state of the art in science in the next chapter.

Chapter 3

State of the art

In this chapter, I provide an overview of the current state of the art on colored photovoltaic modules and yield prediction for vertically mounted, building-integrated photovoltaic modules. This overview is useful for subsequent classification of the results presented in this dissertation.

3.1 Colored building-integrated photovoltaic modules

In the last decades, a lot of research on the development of colored BIPV modules has been done [25]. Numerous different techniques for altering the appearance have been developed. These techniques differ in the complexity and effort of their implementation as well as in the losses they cause and the appearance they provide. For the majority of the techniques that have been developed so far, the costs for industrial production are unknown or difficult to estimate, since they are not (yet) commercially available products but research objects. This leads us to limit the focus of this chapter to the appearance and energy yield caused by the various techniques.
First, I discuss the theoretical work on the appearance and yield loss of colored solar cells. Next, I will overview various techniques for modifying the appearance of PV modules. Finally, I present the approach of Røyset *et al.* [75] to classify colored PV modules.

3.1.1 Theoretical consideration of colored solar cells

Altering the appearance of PV modules always results in a loss of power yield. This loss depends on the method used to change the appearance. Halme and Mäkinen [41] as well as Peharz and Ulm [68] investigated the losses of colored PV modules theoretically in ideal as well as realistic scenarios. Their results for efficiencies for colored solar cells are therefore considered as theoretical maximum achievable values.
Halme and Mäkinen studied the theoretical efficiency limits of single band gap colored solar cells [41]. No particular solar cell technology was considered. In their study, a colored appearance was created by reflecting 100% of the incident light in two very

narrow wavelength regions. Outside the reflected regions, all incident photons were absorbed, as long as their energy is larger than the band gap. The AM1.5G spectrum normalized to 1000 W/m^2 was used as the light source. When calculating the efficiency, they neglected other losses, such as those due to parasitic absorption and considered only the losses due to the reflection R. The decisive factor for the resulting efficiency was therefore the respective Internal Quantum Efficiency (IQE)

$$IQE = 1 - R.$$

By combining two narrow reflection peaks, almost the entire sRGB color space can be produced with a solar cell efficiency of over 29%, compared to the maximum efficiency of 33.77% of a black solar cell with R = 0. This is a very idealized scenario, which cannot be produced in reality.
It is difficult to define a parameter to evaluate how suitable a color or a colored PV module is for an application. Halme and Mäkinen name the interaction of human color perception and luminosity as an important factor for the evaluation of a color. Brighter colors require more reflected light and thus result in lower efficiency. The human eye is most sensitive to the wavelength range around 550 nm, so colors in the green-yellow range are perceived brighter even with lower luminosity. According to Halme and Mäkinen, yellow-green colors are therefore best suited for colored solar cells. Figure 3.1 shows the colors of the MacBeth ColorChecker [62] with the respective efficiency limit and relative luminosity, where 1 means a perfect white reflector. The MacBeth ColorChecker shows typical colors from everyday life based on measured reflectance spectra. It is mainly used for the calibration of cameras.

Figure 3.1: Colors of the Macbeth ColorChecker chart with the relative luminosity and the theoretical efficiency limit calculated by Halme and Mäkinen. Illustration taken from [41].

Peharz and Ulm calculated the power losses of crystalline silicon solar cells for the RAL colors, that are commonly used and standardized in the industry [68]. For this purpose, they measured the reflection spectra of samples in RAL colors and calculated

the respective color coordinates in the CIE-XYZ color space. Subsequently, they simulated these color coordinates by combining two narrow reflective wavelength regions for c-Si solar cells. In contrast to the work of Halme and Mäkinen, the reflectance in this region was left variable and not fixed at 100%, but the width of the reflective wavelength region was defined to be 20 nm and 40 nm, respectively. The resulting power of the colored solar cell was then determined using the two-diode model. Peharz and Ulm thus calculated power losses between 2% and 20% for RAL-colored c-Si solar cells. If the measured, continuous reflection of the RAL colors for the visible wavelength range is used instead of the two narrow reflection ranges, power losses of up to 50% apply for the different RAL colors (Fig.3.2).

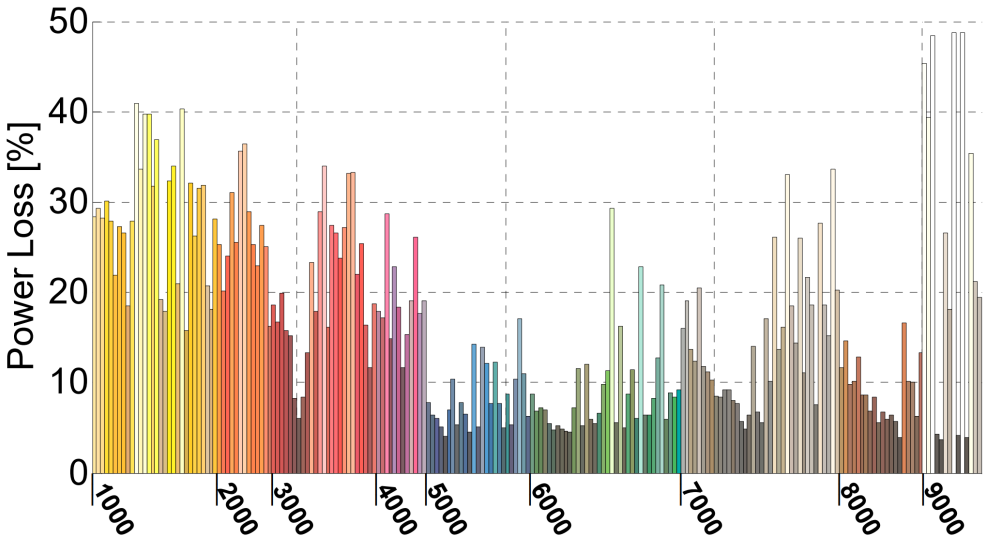

Figure 3.2: Power losses for RAL-colored c-Si solar cells using measured reflection spectra of standardized RAL colors for the wavelength range of 380 nm to 780 nm, calculated by Peharz and Ulm. Figure taken from [68].

3.1.2 Techniques for coloring solar cells and PV modules

Many different techniques have already been developed and evaluated to improve the visual integration of a PV module into its environment, to enhance it aesthetically or simply to allow a high degree of design creativity. In the following, I will give some examples of colored PV modules and solar cells with different manufacturing techniques, with a focus on techniques for Crystalline Silicon (c-Si) solar cells. There are numerous other examples of thin-film and Amorphous Silicon (a-Si) solar cells (see [25] for example), but they were not considered in this work.
I divide the various techniques and examples of colored c-Si PV modules into three categories. In the first category, a modification of the Anti-Reflection Coating (ARC) directly changes the color of the solar cells. The second category summarizes techniques in which the appearance of PV modules is altered by adding or changing coatings and layers between the front glass and the solar cell. The third category includes techniques which modify the front glass.

Anti-reflection coating on solar cells. Uncoated, textured c-Si solar cells reflect about 20% of the incident light. To reduce these optical losses, an ARC is usually applied, which changes the appearance of the solar cell from silvery to dark blue or even black. By varying the thickness or type of the ARC, or by adding additional layers, it is possible to change the reflected wavelength range and thus the color of the solar cell. Such changes of the ARC must be implemented directly by the solar cell manufacturer. The choice of specific colors for colored BIPV modules is very individual, so rather smaller quantities are needed. Since manufacturers usually only work with very large quantities, techniques in this category are rarely used [25]. Figure 3.3 a) shows colored solar cells from Lof Solar with efficiencies ranging from 15.8% to 18.6%, depending on the color [58]. Figure 3.3 b) shows photos of solar cells by Chen *et al.* [13] where a desired narrow reflectance spectrum is created by using two very thin ARCs. The short-circuit current density of those colored cells is above 99% compared to the reference solar cell with only one ARC.

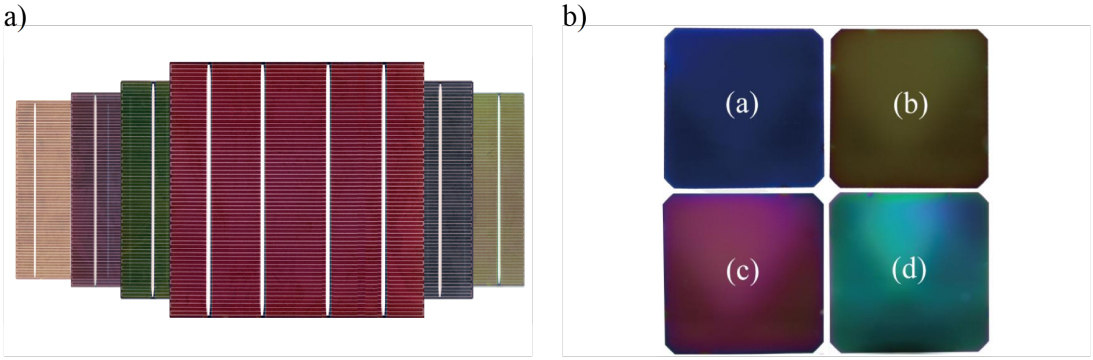

Figure 3.3: Pictures of colored solar cells having their color determined a) by varying the ARC thickness [58] and b) by using two ARCs [13].

Additional and modified layers between solar cell and front glass. Using a colored encapsulation material instead of the standard transparent one allows to use existing process steps and thus saves effort and costs for implementation. Figure 3.4 a) shows photos of single-cell modules produced with colored encapsulation material [55]. The resulting appearance is very dark and some features of the solar cells are still easily distinguishable. By using a colored encapsulation material, the energy yield of the PV modules is reduced by 6% to 20%, depending on the color [55]. Adding an additional layer between the solar cell and the front glass is also easy to implement. Figure 3.4 b) shows a PV module from Kaleo Solar, where a high definition photo has been laminated into a PV module [50]. The solar cells are completely masked, and the colors of the image are powerful. Depending on the picture and colors used, the energy yield reduction is 10% to 40%.

a)

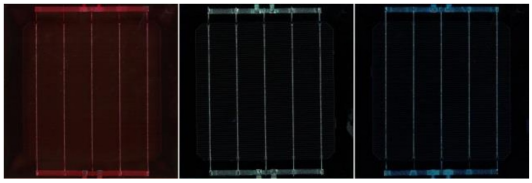

b)

Figure 3.4: a) Photos of single-cell PV modules using colored encapsulation materials [55] and b) BIPV module with an integrated high definition graphic, manufactured by Kaleo Solar [50].

Modifying the front glass. Most of the methods used to change the appearance of PV modules focus on the front glass. Some examples of different techniques are shown in Figure 3.5. The Centre Suisse d'Electronique et de Microtechnique (CSEM) applied a film to the front glass that diffusely reflects most of the visible light, creating a white appearance [25]. The infrared portion of the light is not reflected, thus the white PV module produces approximately 60% of the energy output of a standard module (Fig. 3.5 a). SwissINSO SA developed $Kromatix^{TM}$, a widely used colored front glass [21]. A multi-layer coating is applied to the inside of the glass, which reflects the intended wavelength only. In addition, the surface of the glass is treated so that diffuse reflection takes place instead of specular reflection. Depending on the color, the loss of energy yield is between 10% and 15% compared to a PV module with a standard front glass (Fig. 3.5 b). Another option is to print directly on the front or back of the front glass. In this case, the glass must be printed before the module is manufactured and the inks are permanently bonded to the glass by heating. Depending on the inks and print coverage used, the yield reduction due to printing is between 10% and 50% (Fig. 3.5 c) [24]. In the EU project ConstructPV, sandblasting was used to create micro cavities in the front glass, giving PV modules a milky white appearance (Fig. 3.5 d) [25]. The consortium SolarGlasLabor filled the micro cavities created by sandblasting with color particles, so that the appearance of the PV modules can have any color (Fig. 3.5 e) [80]. Using this technique, the energy yield of PV modules is reduced by 12% to 25%, depending on the color. Another technique was developed by Sunage SUNCOL. They apply a mineral coating to the front glass to produce muted colors with losses in energy yield between 13% and 15% (Fig. 3.5 f) [25]. Bläsi *et al.* established a promising method using the principle of the Morpho butterfly: through a combination of thin-film interference effects and a three-dimensional photonic structure, only a selected narrow wavelength range is reflected (Fig. 3.5 g) [9]. This allows bright colors to be produced with a relatively small loss in energy output of about 7%. The technique involves both processing the inside of the front glass and also applying an additional layer underneath the front glass.

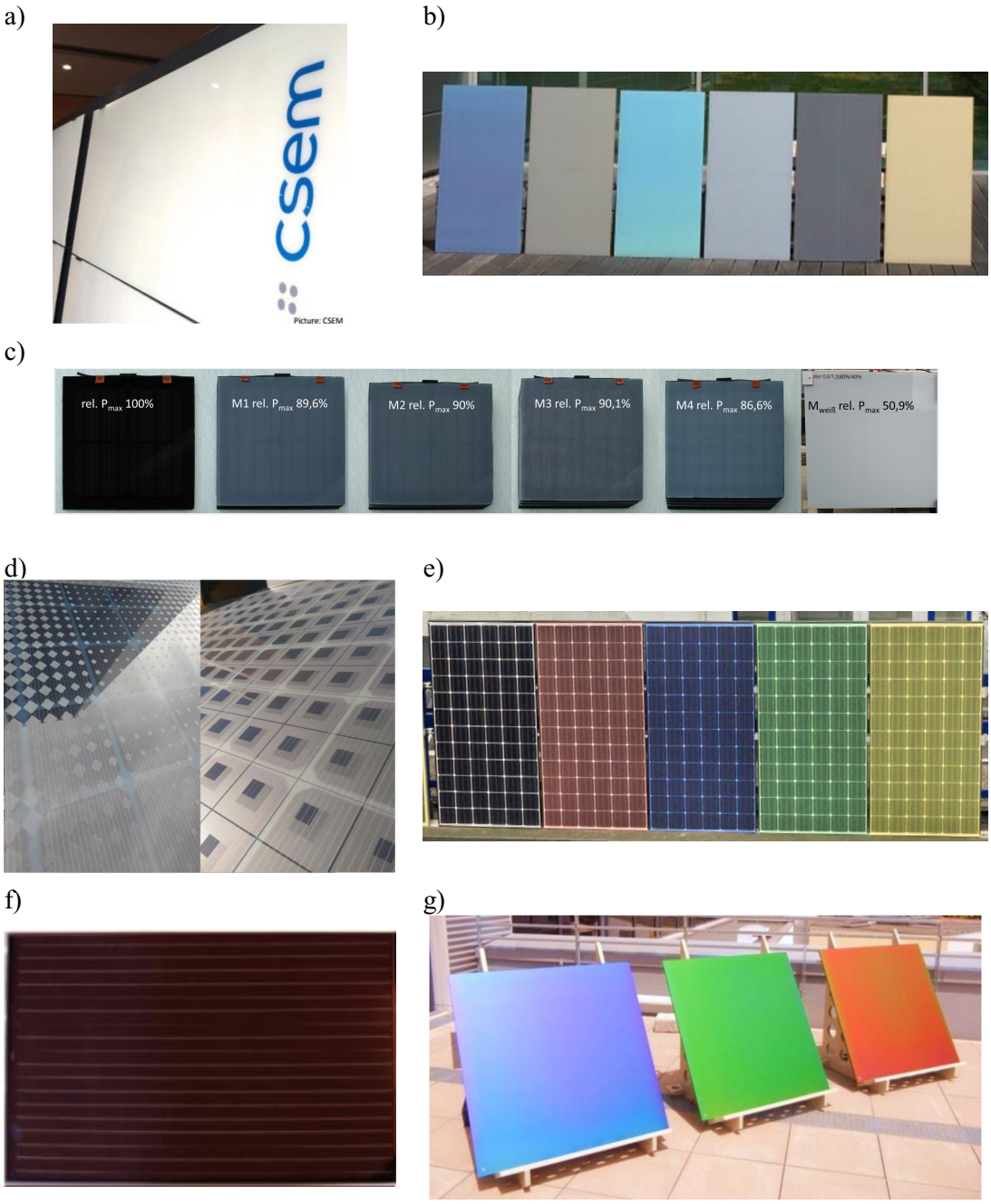

Figure 3.5: Photos of PV modules whose appearance has been modified by various techniques. a) White PV modules by CSEM [25], b) Colored PV modules with $Kromatix^{TM}$ front glasses by SwissINSO [21], c) Single-cell modules altered with digital printing [24], d) sand blasted milky-white PV modules [25], e) sand blasted and colored PV modules, produced by SolarGlasLabor [80], f) red PV module colored by mineral coating, manufactured by Sunage SUNCOL [25], g) PV modules colored using the Morpho butterfly effect [9].

3.1.3 Classification of colored PV modules with respect to appearance and energy yield

The losses in energy yield with different coloring techniques can be easily expressed quantitatively by comparison with a reference module thus enabling classification. The appearance or color of PV modules is more difficult to classify. Figure 3.6 a) shows

15 colored PV modules that obtained their color by different techniques [75]. Røyset *et al.* measured the reflectance spectra of those samples and used them to calculate the color coordinates in the CIE-XYZ and CIE-L*a*b* color space. They showed that the luminosity, defined by the color coordinate Y or $L*$, has the strongest effect on the energy yield of the PV modules. Therefore, to compare colored PV modules, they introduced a Color Performance Index (CPI)

$$CPI = \frac{Y}{r_{\text{power}}}, \tag{3.1}$$

where r_{power} corresponds to the loss of energy yield relative to a reference module. Figure 3.6 b) shows the CPI and power loss for the 15 colored PV modules in Figure 3.6 a). They found that the energy yield of a PV module decreases with increasing luminosity. For the 15 samples measured, the CPI was between 0.9 and 1.6 [75]. The CPI allows a classification: the high luminosity with a high r_{power} of sample 9 has a higher CPI than a PV module with a low luminosity and low r_{power}, such as sample 12. Sample 11, in which luminosity and r_{power} are in the medium range, has the highest CPI. The CPI can thus also be particularly helpful when comparing different coloring techniques. If the coverage of the colored layer, and thus the degree of masking of the underlying solar cell, the intensity of the color and the energy yield differ, the CPI can be used for evaluation.

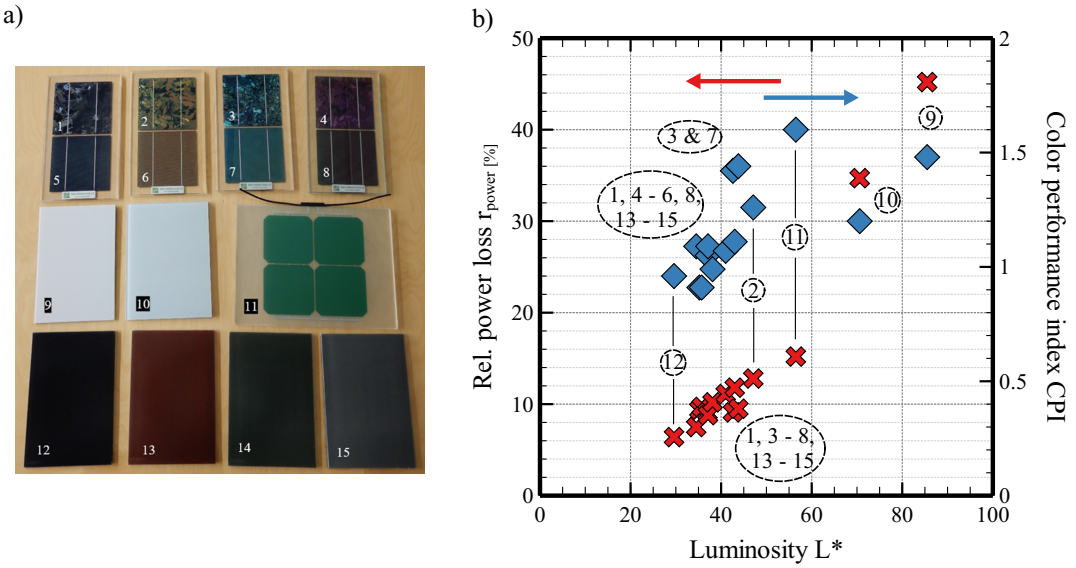

Figure 3.6: a) Pictures of 15 colored PV modules and b) the corresponding relative power loss r_{power} (red crosses) and CPI values (blue diamonds) plotted against luminosity as reported in [75]. The numbers indicates the sample number from a).

3.2 Energy yield estimation

The output power and other parameters of a PV module such as current I_{MPP} and voltage V_{MPP} at the maximum power point, short-circuit current I_{SC} and open-circuit

voltage V_{OC} are specified by manufacturers for STC, i.e. at a perpendicular irradiation of 1000 W/m² using the AM1.5g spectral distribution and an ambient temperature of 25°C [16]. However, the characteristics obtained under STC differ from the actual achieved values in outdoor applications, which depend strongly on the orientation and tilt angle of the module and the weather at the location. Yield predictions estimate the actual energy yield of a PV module under realistic field conditions.
The insolation on the PV module has a major influence on the PV yield [44,86]. However, usually only irradiation values in the horizontal plane are available, from which the irradiation in the inclined plane must then be derived. Figure 3.7 shows the direct I_{direct} and diffuse I_{diffuse} solar irradiation, as well as the ground-reflected irradiation I_{ground} incident on a PV module tilted by an angle α. These three terms have to be calculated from the global horizontal irradiance (GHI), the direct normal irradiance (DNI) and the diffuse horizontal irradiance (DHI). Where DNI and DHI must first be calculated from the GHI. I will explain these relationsips in more detail in chapter 6. The total irradiation on the tilted module I_t is given by:

$$I_t = I_{\text{direct}} + I_{\text{diffuse}} + I_{\text{ground}}. \tag{3.2}$$

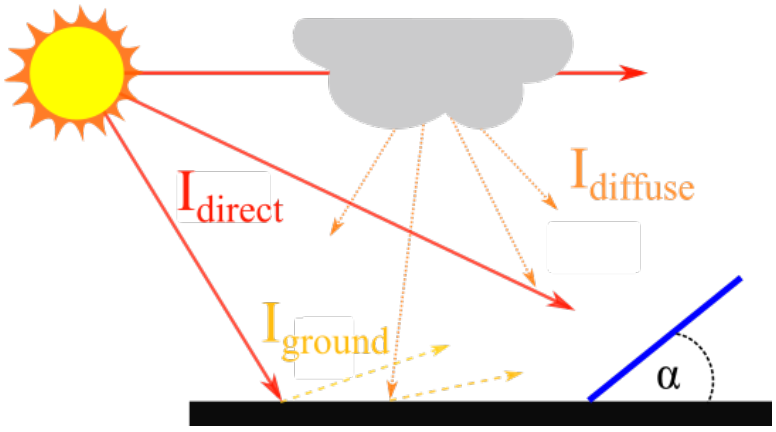

Figure 3.7: Scheme of direct (I_{direct}) and diffuse (I_{diffuse}) solar irradiation as well as ground-reflected irradiation (I_{ground}) hitting a PV module tilted by angle α.

I_{direct} can be calculated directly from the geometric relationship between the module plane, the position of the sun and the DNI. Difficulties arise in the conversion of the diffuse horizontal irradiance to the inclined plane and in the calculation of the ground reflection.
When calculating I_{ground}, an isotropic model is usually used and an infinitely extended, open area in front of the PV module is assumed [18]. Only the installation angle of the PV module, the GHI and an average albedo ρ_{mean} are considered:

$$I_{\text{ground}} = GHI \cdot \rho_{\text{mean}} \cdot \frac{1 - \cos\alpha}{2} \tag{3.3}$$

For façade modules that are mounted vertically ($\alpha = 90°$), this equation simplifies to:

$$I_{\text{ground}} = \frac{1}{2} GHI \cdot \rho_{mean} \tag{3.4}$$

However, this equation often leads to an overestimation of I_{ground}, especially for façade modules, since there are usually no infinitely extended open areas in front of façade modules. Furthermore, it would be helpful to specify several albedos, as the surfaces in front of façades are often different, e.g. lawn, pavement and asphalt road alternate. For this reason, I introduce the ground view factor (GVF), where a higher accuracy is to be achieved by considering several environmental variables. Please have a look at section 2.3.2 for the theory of the GVF.

I_{diffuse} is calculated via transposition models from the DHI. There are at least 30 different approaches to transpose the irradiation from horizontal to an inclined plane [17]. The simplest models assume purely isotropic radiation (e.g. Liu & Jordan [57]). However, this assumption underestimates I_{diffuse} because a module facing the sun receives more diffuse irradiance than a module facing other directions [38, 85]. Anisotropic models such as those developed by Perez [70], Reindl [73], Gueymard [37], Hay & Davies [42] and Klucher [52], among others, take into account a circumsolar and a horizontal brightening factor. These factors describe a direction-dependent higher diffuse irradiation from the sun and the horizon. Depending on location and climate, the models differ in their applicability, mostly because they are more prone to error for primarily sunny, cloudy, or heavily overcast sky conditions [38, 39, 44].
Numerous of these models have been evaluated and compared for different locations around the world and for differently inclined planes. Table 3.1 shows the smallest reported errors in literature in the calculation of insolation on tilted planes for different locations for south-facing surfaces. Different transposition models were used and compared in all studies. Only the smallest errors from each study are listed in the table. The errors depend on the tilt angle and were obtained for different climatic zones. The sampling rates of the measurement data range from intervals of hours to minutes. The time periods considered span from 25 days spread over a year to several years. The authors of the considered studies evaluated the accuracy of the models by the relative root mean square error e

$$e = \frac{\sum \sqrt{(I_{meas} - I_{calc})^2}}{N \cdot \overline{I_{meas}}}, \tag{3.5}$$

with the measured irradiance I_{meas}, the calculated irradiance I_{calc} and the mean irradiance $\overline{I_{\text{meas}}}$ of all N measured irradiance values.

Table 3.1: Accuracy achieved for the transposition of horizontal irradiation to an inclined plane depending on input measured irradiation data and module inclination [18, 20, 38, 46, 56, 59, 63–66, 69].

Input irradiance data	module tilt	lowest e	reference
GHI, DNI/DHI and I_{ground}	40° - 51°	4.3% - 8%	[38, 46, 63]
	90°	5.6% - 7.7%	
GHI and DNI/DHI	40° - 51°	4.3% - 17.8%	[18, 20, 38, 59, 65, 69, 73]
	90°	7.6% - 12.9%	[38, 59, 69, 73]
GHI	40° - 51°	8% - 10.16%	[38, 46, 56, 64, 66]
	90°	16% - 19.5%	[38, 46, 64]

Since the performance of the models depends on the local weather conditions and orientation of the PV modules, we take a closer look at the results of the study by Mubarak *et al.* [63]. The measurements of Mubarak *et al.* took place at the Institute of Meteorology and Climatology at the Leibniz University of Hanover, which is only about 43 km away from the Institute for Solar Energy Research Hamelin (ISFH) and thus the measurements presented in this work. Therefore, the weather conditions of the two sites are comparable. In their study, the authors calculate the irradiation incident on planes inclined by 10°, 20°, 30°, 40°, 50°, 60°, 70° and oriented toward the south, as well as on vertical planes oriented toward the East (E), South (S), West (W), North (N), South-East (SE), and South-West (SW). For the calculations they used the transposition models of Liu & Jordan [57], Klucher [52], Hay & Davies [42], Reindl [73] and Perez [70]. Measured input data were the GHI, DHI, and ground reflectance over a 2-year period. The calculated irradiation is compared with the measured global irradiation in the respective inclined plane during the same period. Figure 3.8 shows the resulting e values of the respective models, module inclinations and cardinal directions. With the exception of the Hay & Davies model, e increases with increasing tilt for all models and is maximum at 90°. It is also significant that the anisotropic models show the best agreement for south-facing PV modules and the worst agreement for north-facing modules.

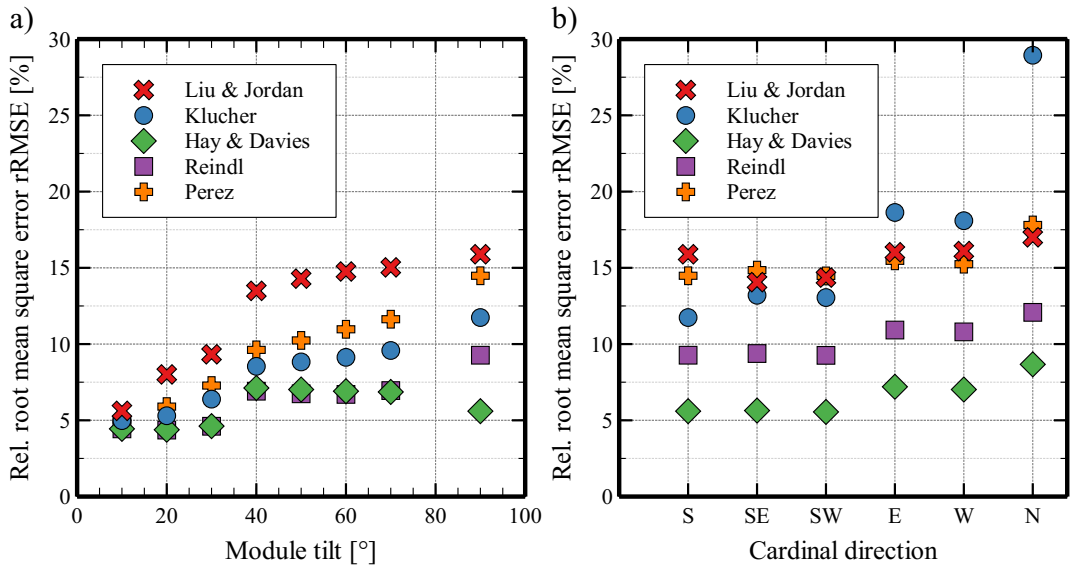

Figure 3.8: e of calculated irradiation on inclined planes with 5 different transposition models for a) different inclination angles towards south and b) different cardinal directions for an inclination angle of 90°, as reported in [63].

Hofmann *et al.* showed for 30 locations around the world that despite the high e, if measured GHI and DHI are used, the annual energy yield of a PV module tilted by 40° towards the south can be estimated with an absolute deviation between -4% and +3%. If only GHI data is available, the annual deviation is between -5% and +9% [44]. Depending on the location, the time resolution of the input measurements, the transposition model used and the model used to calculate the DHI, this deviation can be significantly smaller [44].

The research results in this field emphasize two aspects: First, the accuracy of the yield prediction for façade modules is lower than for on-roof modules or other modules that are tilted by 30° to 50°. Second, the accuracy of the yield prediction strongly depends on the models used to estimate the irradiance on the PV module, the climatic conditions at a specific location as well as the specific application. No model can be declared as the best model, depending on the application, a certain model may be more suitable than others. There is currently no decision-making criterion for selecting the potentially best model for a particular location. Depending on the local weather and climate, a particular model will provide the best results. However, to find this model, measurement data is required and several models need to be tested and compared.

Chapter 4

Postproduction coloring of PV modules with imprinted textiles

This chapter deals with experimental investigations on CoTex PV modules. Different textiles and colors are analyzed in terms of appearance, short-circuit current density and coverage of the solar cells. Furthermore, investigations of the durability of the CoTex structure, of the UV stability and outdoor yield measurements are presented. I have already published the manufacturing process of the CoTex modules, as well as some of the results described in this chapter, in [36] and in [32].

4.1 Fabrication and measurement methods

4.1.1 Fabrication of customized PV modules containing textile layer

Figure 4.1 shows the structure of the CoTex BIPV modules [32]. It is composed of a commercially available PV module and an additional layer system on top.

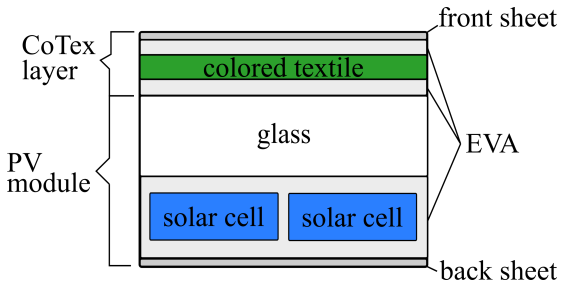

Figure 4.1: Schematic of the CoTex PV modules: In addition to the normal setup of a PV module, a colored textile or other fabric is laminated onto the front glass and protected by a weather-resistant top layer. [36]

The CoTex layer system consists of a woven or a nonwoven fabric embedded between two layers of UV-absorbing EVA (EVASKY S87, Bridgestone) and covered with a transparent front sheet (FPL-FET-T250-T50, Toyal Solar). In this work, I apply the CoTex layer system in two ways: It is either laminated onto the respective PV module in one lamination step. I refer to this type as **permanent** application. I use a standard

PV module laminator (ICOLAM, Meier Vakuumtechnik), a temperature of 150 °C, a pressure of 10^5 Pa and a lamination time of 15 minutes. Otherwise I use the refractive index matching liquid Paraffin, to temporarily couple the CoTex layer system optically to the PV module [53]. This facilitates the screening of a large number of different top layers on top of one and always the same PV module. I refer to this type of application as **non-permanent**. [32]

Any nonwoven fabric or other textile may be used for this approach, whether colored or white. Printing on a specific textile allows a wide range of colors and also the printing of patterns and images. For printing I use the material Freudenberg Performance Light Diffuser (FPLD) [30], which is a nonwoven fabric for LED lighting systems. It consists of polyester fibers and combines high transmission and strong light diffusion. This material is available in different variations. I use the FPLD 40, 50 and 65, where the number indicates the density of the material in g/m². [32]

In this work, I also use colored foils to fabricate customized PV modules. In this case, I replace the CoTex layer in Fig. 4.1 by the foil. However, the foil is irrelevant to this chapter, so I will not discuss it in more detail until Chapter 5.

The measurements done in this work on non-permanently applied samples are all performed with the same single cell module shown in Fig. 4.2 a) and b). We prepare this one-cell PV module using a 156 × 156 mm² silicon solar cell with silver fingers on the front and a full-area aluminum metallization on the rear. The cell is contacted on the front and the rear with the smart wire technology [79]. The module has a three-film transparent backsheet (FPL-FET-T250-T50, Toyal Solar) on the bottom. The cell is encapsulated with UV-transmissive EVA (EVASKY S85, Bridgestone) with a thickness of 460 μm and has a low-iron glass plate with a thickness of 4 mm on the top. [32]

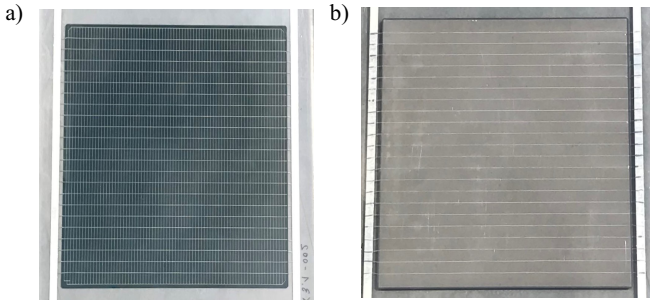

Figure 4.2: Frontside (a) and backside (b) of the single-cell module, used for the measurements in this work. [32]

4.1.2 Coloring of the nonwoven fabrics

Two different printers were used for coloring the samples. Most samples were printed with an inkjet hybrid printer Anapurna FB2540i LED from and by Agfa [2]. It uses cyan, magenta, yellow, black (CMYK) and white inks to print a wide color space. The printer prints on substrates with a width of up to 3.2 m for outdoor and indoor applications. It works with the halftone technique (see sec. 2.2.1) and creates a homogeneous

color impression by printing the individual basic colors in a dot pattern. Figure 4.3 shows that the size and density of the dots varies depending on the print coverage and the required color impression. As an alternative, the printing of certain samples was performed with an offset printing system. This was done by a local print shop, which could not give me any further information about the printing system.

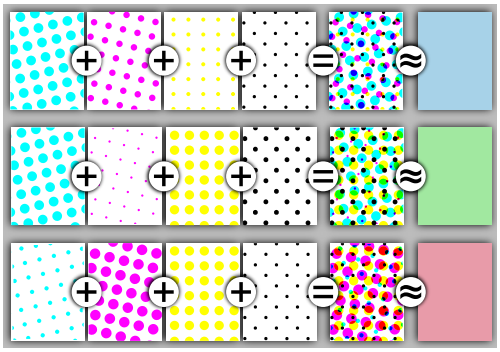

Figure 4.3: Principle of the halftone printing process. The combination of the primary colors, printed in different dot sizes and densities, create a homogeneous appearance. Illustration taken from [89].

For the purpose of comparison, offset printing, also in halftone and CMYK system, was selected as the second printing process. In offset printing, the ink is transferred from the print plate to a rubber blanket and then to the surface of the printing material. In offset printing, the desired color pattern is transferred via printing plates to a blanket cylinder and from there to the printed material.

4.1.3 Durability tests

To test the durability of the CoTex setup, two single-cell modules were fabricated according to the setup presented in 4.1.1. On one module a FPLD50 is permanently laminated. The second module is not covered with a CoTex layer and serves as a reference.
Referring to the IEC 61215 standard [6], we expose both modules to 1200 h damp-heat and 200 humidity-freeze cycles of 12 h duration each and temperatures from -40 °C to +85 °C to test the durability under climatic conditions. I measure the *EQE* and reflectance before the start of the test and after every 50 cycles. I compare the effects of the durability test between CoTex and reference module in terms of the J_{SC} and the eventual change in appearance. However, the main focus of this test is on the durability of the CoTex structure. I define as the criterion for passing the test that no damage or delamination of the top layer is apparent by eye inspection.

4.1.4 UV-stability test

An irradiation chamber generates Ultraviolet (UV) light of 210 W/m² ± 20 W/m² in the wavelength range between 280 nm and 450 nm using four *Hoenle* UVASpot lamps with a broad spectral irradiance between 300 nm and 450 nm and a *Philips TL20W/01* UVB313 with a peak at 313 nm. [90] Figure 4.4 shows the normalized spectral irradiance of the UVASpots and the UVB313 lamp.

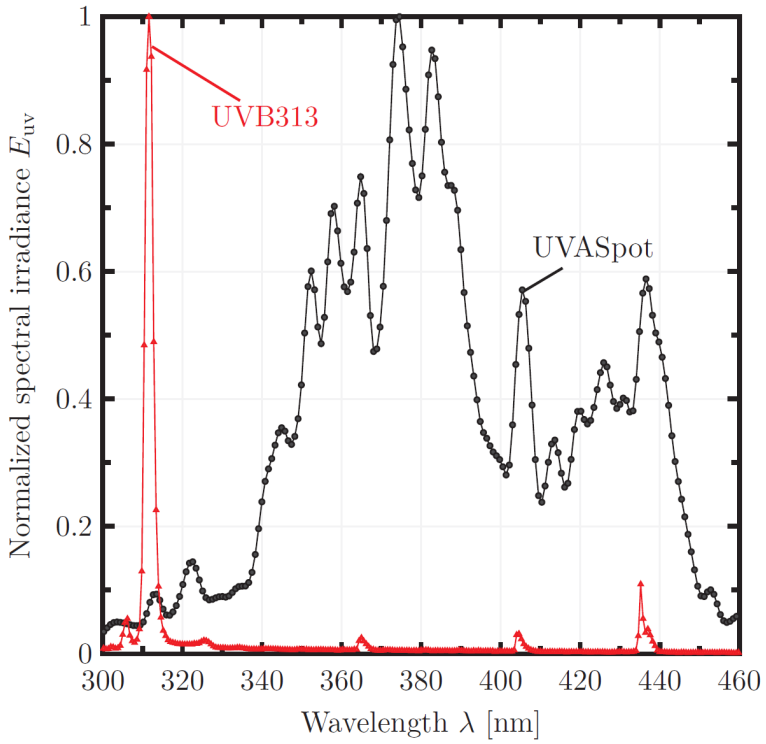

Figure 4.4: Normalized spectral irradiance $E_{UV}(\lambda)$ of the UVASpot and UVB313 light sources used for the UV-stability test. The lines are a guide for the eye. Figure taken from reference [90].

For a UV-stability test, one single-cell module is fabricated according to the setup presented in 4.1.1. The CoTex layer is permanently laminated and contains a printed FPLD50. Figure 4.5 shows the printed colors A1, A2, A3, C5, C6, C7, E8 and E9. Each box indicates the respective print coverage of the inks cyan (c), magenta (m), and yellow (y). In one box, the PV module is covered with a CoTex layer, but without a textile. This area serves as a reference (Ref.). The module is irradiated for 3250 hours in the UV chamber, which is a total irradiation of 682.5 kWh/m² and comparable to the UV dose of 20 years in Germany [28]. The temperature of the CoTex module during irradiation is 58°C. Before and after UV irradiation, the *EQE* and reflectance are measured and the J_{SC} and XYZ color coordinates are determined from the measurements. I compare the J_{SC} and the color of the eight color patches and the reference area. I use the color difference ΔE_{00} to evaluate the visual difference before and after the UV irradiation.

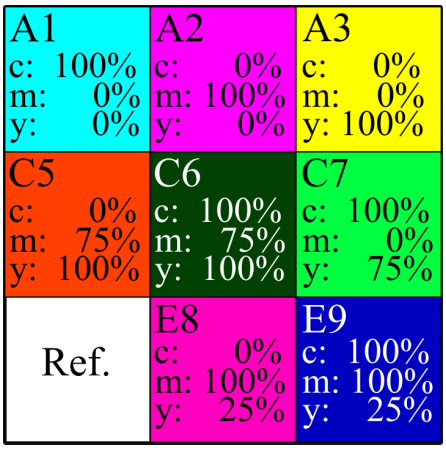

Figure 4.5: Print sample for the UV-stability test, printed on a FPLD50 for a single cell CoTex module. The CoTex layer is permanently laminated onto the module. Each box indicates the respective print coverage of the inks cyan (c), magenta (m), and yellow (y). The box at the bottom left does not contain FPLD50 and is used as a reference (Ref.).

4.1.5 Measurement of the reflection spectrum

I measure the reflection spectrum in a wavelength range from 360 nm to 830 nm in 1 nm steps using a photospectrometer (Cary 5000, Agilent Technologies, CA, USA) with an integrating sphere. The illumination angle is 7° to the normal of the sample and the illuminating spot has a radius of 18 mm. For calibration, a 0% baseline, i.e. with open sample entrance in complete darkness, and a 100% baseline with a strongly diffusely scattering spectralon are captured before the measurement. The reflection spectrum R_{sample} of a sample is calculated with the baseline reflections $R_{100\%}$ and $R_{0\%}$ and with the measured reflection spectrum R_{meas} of the respective sample:

$$R_{\text{sample}} = \frac{R_{\text{meas}} - R_{0\%}}{R_{100\%} - R_{0\%}} \cdot r_{\text{spectralon}} \tag{4.1}$$

The spectralon is used for calibration in our measuring device. The reflection of the spectralon $r_{\text{spectralon}}$ was therefore determined in an external calibration laboratory.

4.1.6 Measurement of the external quantum efficiency

I perform spectrally resolved *EQE* measurements at a wavelength range from 300 nm to 1200 nm in 10 nm steps using the LOANA system (PV-Tools GmbH, Hamelin, Germany) in order to determine the performance losses caused by the colored top layer. The illumination direction is perpendicular to the sample and the illuminated spot is 20×20 mm^2. Following the IEC 60904-8 standard [16], the LOANA system uses a bias background illumination to measure the solar cell at the working level of 300 W/m^2.

4.1.7 Measurement of the short-circuit current density

For the measurement of the J_{SC}, we use a commercial class AAA flash solar simulator (h.a.l.m. Elektronik GmbH, Frankfurt, Germany) and measure with STC at an irradiance of 1000 W/m².

4.1.8 Measurements at the outdoor façade test facility

Figure 4.6 shows the test stand on a south façade at the ISFH, which I already presented in reference [34]. Here, the parameters, which are required for investigations into yield calculations, are measured at one-minute intervals. The irradiance is measured with pyranometers of the type CM11 (Kipp & Zonen). One pyranometer measures the Global Vertical Irradiance (GVI) (1) at the façade, one the Diffuse Vertical Irradiance (DVI) (2) and a third one the global horizontal irradiance (GHI) (3) on the roof. In addition, the diffuse horizontal irradiance (DHI) is measured every five minutes with a similar pyranometer elsewhere at ISFH in another test facility. The pyranometers are calibrated every two years according to the ISO 9847 standard [29]. Various Pt100 sensors measure the ambient temperature (4) and the module temperature (6, 7). The sensor for the ambient temperature is located in a ventilated housing. The temperature of the modules is measured with two sensors, one in the middle and one at the edge, on the back of the modules. A first class anemometer (Thies Clima) measures the wind speed directly on the façade in horizontal direction (5). All environmental conditions are recorded with the 34970A (Agilent) data logger.

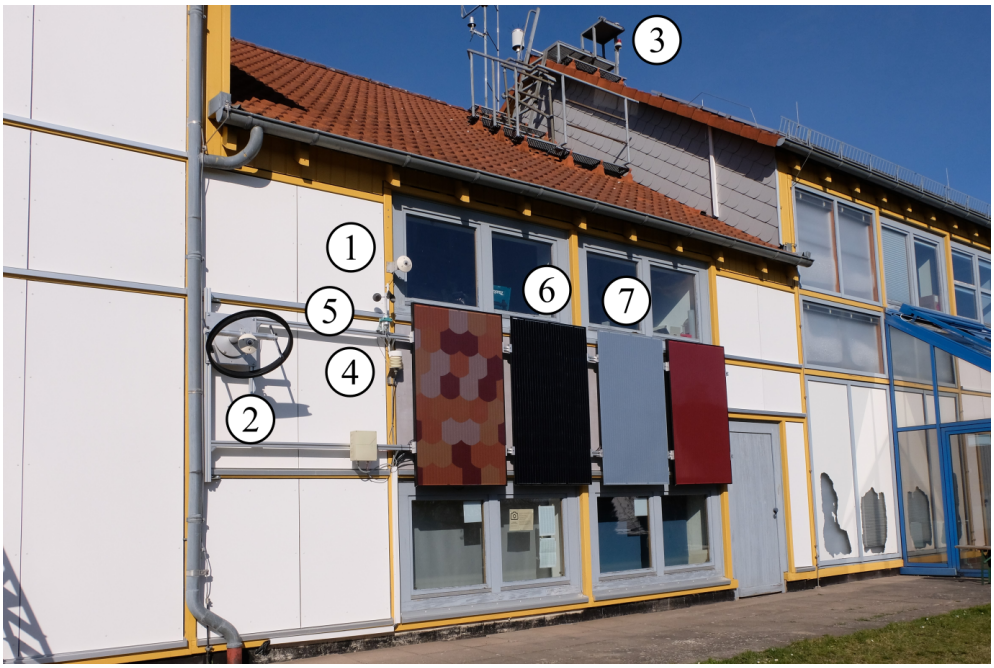

Figure 4.6: Outdoor test facility on a south façade at ISFH. Measurements of GVI (1), DVI (2), GHI (3), ambient temperature (4), wind speed (5) and the I-V-characteristic curve of a standard PV module (6) and a CoTex PV module (7) are carried out every minute.

In addition, the characteristic I-V-curve and the temperature of two PV modules are recorded every minute since June 2019. The modules are 60-cell monocrystalline c-Si PV modules (Standard M.60-B-300, SoliTek) with black a backsheet (Table 4.1). The standard module (6) achieves an output of 300 W at STC. The second module is a CoTex module, with the same module type (Standard M.60-B-300, SoliTek) as a base but, permanently laminated with an unprinted FPLD65 (7). The STC power is 259 W. The I-V curve of the two PV modules is measured with electronic loads (one for each module) of type ESL-Solar 500 (ET Instrumente GmbH) at minute intervals (sweeping time approximately 10 seconds). Between these measurements, the modules are kept at the Maximum Power Point (MPP), which represents realistic operating conditions. The I_{SC}, V_{OC} and the P_{MPP} are determined from the I-V curve. The eletronic loads are connected to the modules via a four-wire connection for independent current and voltage measurements.

Table 4.1: Module data of the Solitek Standard M.60-B-300 PV module. Adopted from the manufacturer's data sheet. [81]

Electrical parameters		Mechanical parameters	
P_{MPP}	300 Wp	Cell size	156.75 mm x 156.75 mm
V_{MPP}	32.13 V	Number of cells	60
I_{MPP}	9.34 A	Front side glass	3.2 mm tempered solar glass
V_{OC}	40.46 V	Dimensions (L x W x H)	1640 mm x 992 mm x 35 mm
I_{SC}	9.89 A	Cable Length	0.8 m - 1.1 m
Power tolerance	0 to 5 W	Cable cross section size	4 mm^2
Module efficiency	18.44%	Number of diodes	3

4.2 Analysis of the appearance, energy yield and durability of CoTex PV modules

First, I examine the appearance and energy yield when using different textiles for CoTex modules. In particular, I investigate in detail the influence on appearance and energy yield when printing on FPLD with different colors, printing techniques and ink coverages.
Subsequently, I will address practical questions about CoTex modules. For this purpose, I am analyzing CoTex modules for their durability, UV stability and behavior under real conditions.

4.2.1 Position of the textile

Figure 4.7 sketches a single-cell PV module which contains a textile under the front glass in the left third and above the front glass in the right third. In the middle there is no textile, this corresponds to the standard structure of a PV module. As described

in section 4.1.1, we use the setup shown in the right third, where we place the textile onto the front glass of the PV module. It would also be possible to position it between the front glass and the solar cell. In such a setup, the expected current yield would be higher because two layers - the weather-resistant top layer and an encapsulation layer - would not be needed. However, this position would have two major disadvantages. First, the lateral scattering of light between the textile and the solar cell would be significantly lower if the light first passes through the 4-mm-thick glass plate and is scattered afterwards. The consequence is that the masking effect due to the textile is lower, so the solar cell is more noticeable. Secondly, it would then no longer be possible to apply textiles to photovoltaic modules that have already been manufactured. This work focuses on the setup in the right third because it facilitates the optical modification of arbitrary industrially manufactured PV modules, which is a major advantage of the CoTeX method.

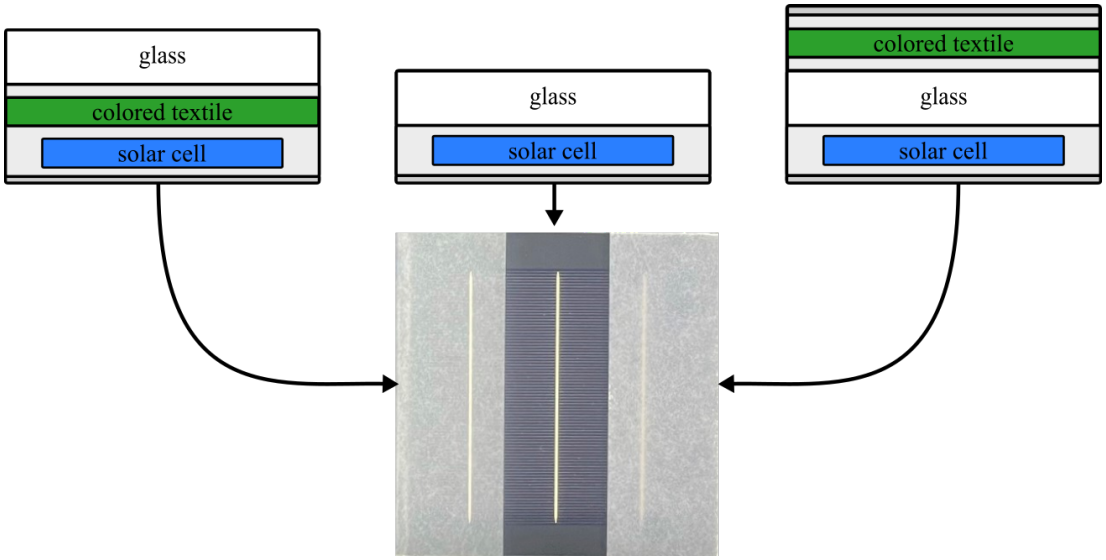

Figure 4.7: Schematic and photograph of a single-cell PV module with a textile under the front glass (left), without a textile (middle) and with a textile on the front glass (right).

4.2.2 Visual assessment of the samples

The appearance is a decisive criterion for the evaluation of colored BIPV modules. Therefore, in this section we will first of all look at the appearance of PV modules whose appearance has been changed with different textiles. Figure 4.8 shows the photographs of a selection of single-cell modules that are permanently laminated with different textiles. Photos a) to e) show homogeneous, white textiles, which give the solar cell a more or less homogeneous, white or grayish appearance, depending on the material. Pictures d) and e) show structured textiles. These structures make the solar cell appear more inconspicuous in the background. Photograph f) shows a single-cell module covered with green gauze. The structure of the solar cell shines through at close range, but with some distance a homogeneous green color impression is created. The CoTex technique allows the use of a large number of different textiles, fabrics and other thin

materials. Depending on individual requirements, a specific material can be chosen, which has a certain color impression and masking of the solar cell.

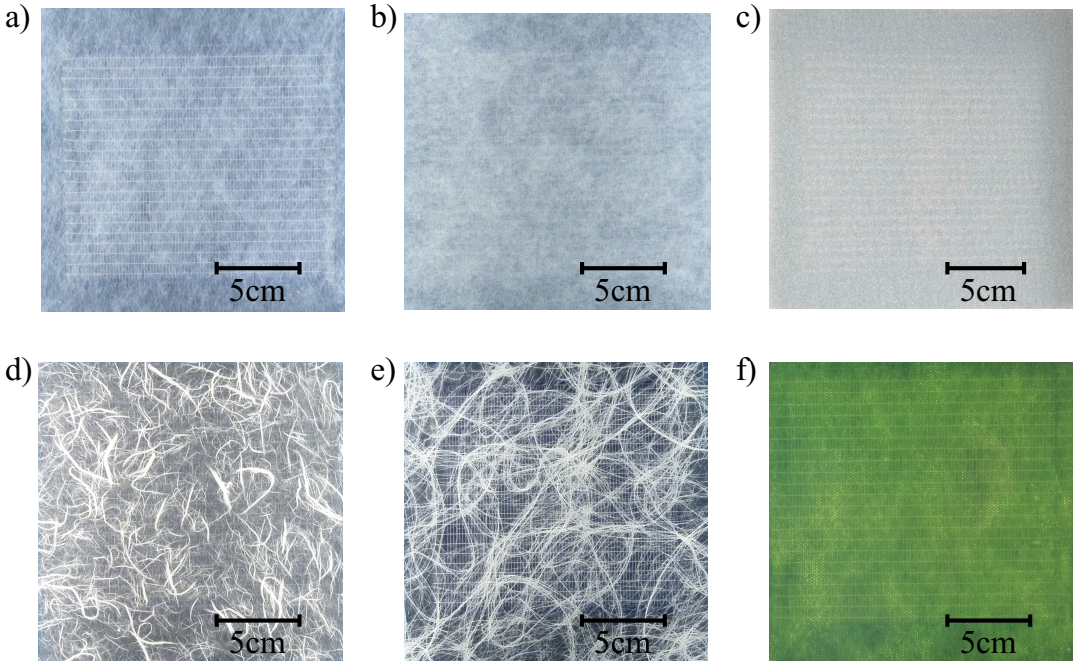

Figure 4.8: Single-cell modules, covered with a) a nonwoven fabric, b) two layers of nonwoven fabrics, c) a FPLD65, d) a Japanese paper, e) a sisal fabric and f) 6 layers of a green gauze.

A simple and quick customization can be achieved by printing an appropriate material. We select the FPLD (Fig. 4.8 c)) in different densities for printing. Figure 4.9 shows photos of nine samples, imprinted with an inktjet printer. In Fig. 4.9 a) through c) the three basic colors cyan, magenta and yellow are printed with 100% coverage on the thinnest textile, the FPLD40. Due to the 100% print coverage, the masking impression is high. The dark blue color of the solar cell shines through, making the colors appear rather dark. This is because the nonwoven fabric is thin.
Samples shown in figure 4.9 d) through f) demonstrate the effect of the different thicknesses of the nonwoven fabric. The fabrics FPLD40 (d), FPLD50 (e) and FPLD65 (f) are all printed in yellow with a coverage of 100%. The yellow color tone becomes stronger with thicker FPLD. More striking, however, is that with FPLD40 the fingers are still shining through, with FPLD50 they can only be guessed and with FPLD65 they are no longer visible. Note, however, that the sample in figure 4.9 f) has two wide busbars, which can still be discerned. The CoTex method is therefore better suited for multi-busbar or even busbarless interconnection. Figure 4.9 g) through i) demonstrates that an increase in print coverage makes the color impression stronger. Here, the FPLD50 is printed with magenta in coverages of 50% (g), 70% (h) and 100% (i). The solar cell appears completely masked at a print coverage of 50%. For comparison: Fig. 4.9 b) shows the FPLD40, printed with magenta in 100% print coverage. There, the fingers of the solar cell still shine through the top layer. In the case of figure 4.9

g)-i), the masking is not improved by an increased print coverage. With inks that are not as opaque, or with solar cells that have busbars, the degree of masking can be improved by increasing the print coverage. [36]

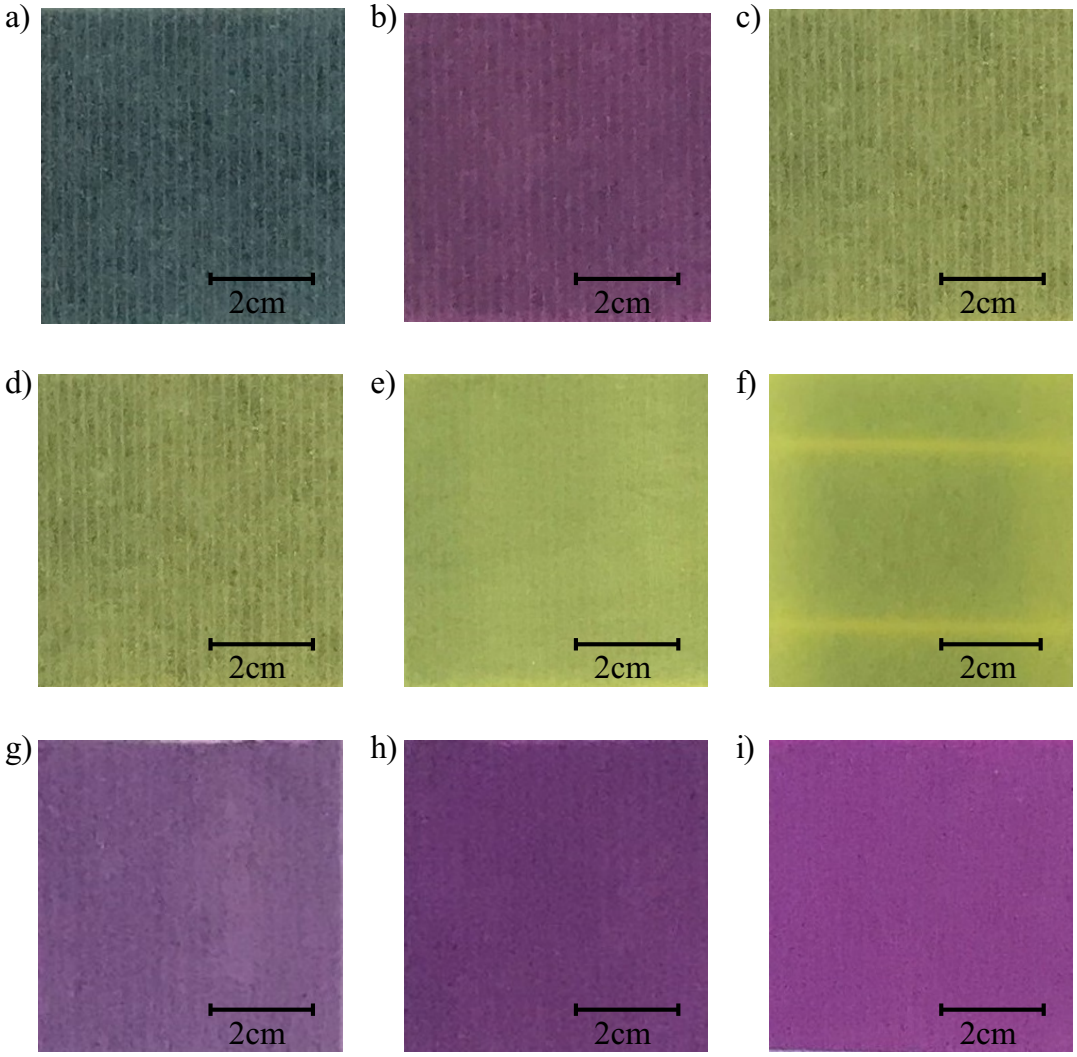

Figure 4.9: FPLD40 imprinted with (a) cyan, (b) magenta and (c) yellow in 100% print coverage; (d) FPLD40, (e) the FPLD50 and (f) the FPLD65 all imprinted with yellow in 100% print coverage; FPLD50 imprinted with magenta in (g) 50%, (h) 70% and (i) 100% print coverage. [36]

However, the appearance of the PV modules does not only depend on the textile and the selected print coverage. Fig. 4.10 and 4.11 clarify that not only the printing parameters, but also the printing technology and the inks used are important. Figure 4.10 shows photographs of PV modules covered with the FPLP50 and printed in the three basic colors and 100% print coverage. (a) to (c) were printed with an inkjet printer, (d) to (f) using an offset printer. The colors of the CoTex modules printed with the offset printer look darker and also more inhomogeneous.

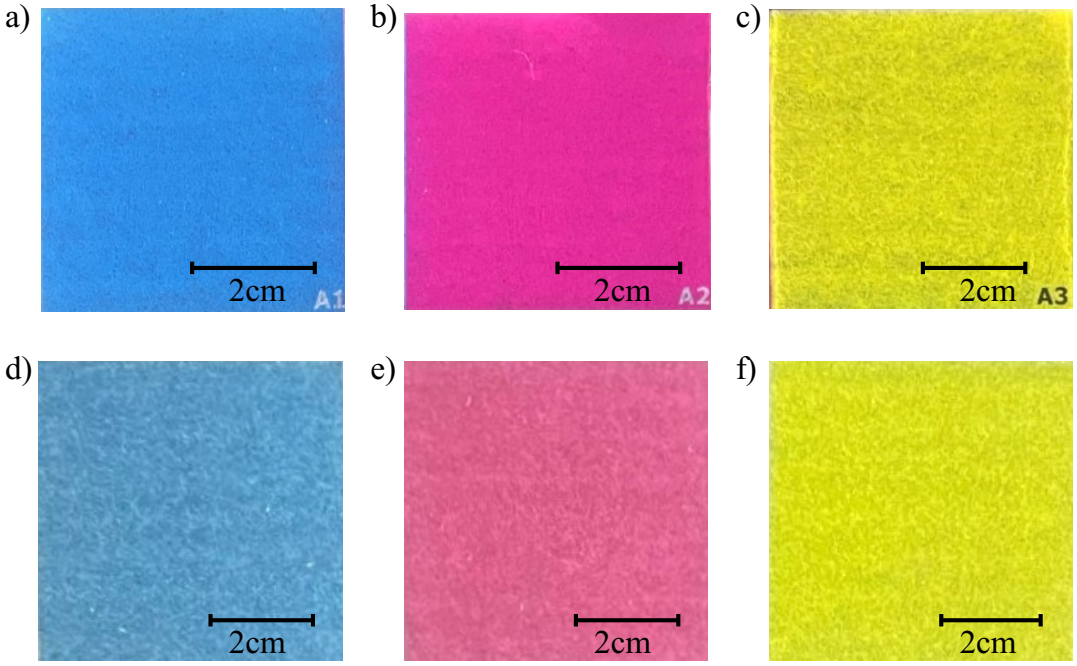

Figure 4.10: Single-cell PV modules covered with a FPLD50 and imprinted in 100% print coverage using an inkjet printer with (a) cyan, (b) magenta and (c) yellow and using an offset printer with (d) cyan, (e) magenta and (f) yellow.

Figure 4.11 shows the reflectance spectra of the samples from Fig. 4.10 and details the differences between the printing techniques and inks used by the inkjet and the offset printer. The overall shape of the spectra for the respective inks is comparable but there are notable deviations. For example, in Fig. 4.11 a), the reflectance maximum for both cyan samples is in the range between 400 nm and 500 nm and the reflectance is low in the range between 550 nm and 750 nm. However, the two spectra show a difference of up to 0.02 (Fig. 4.11 a). The maximum observed deviations for magenta (Fig. 4.11 b) and yellow (Fig. 4.11 c) are even higher at 0.04 and 0.05, respectively.

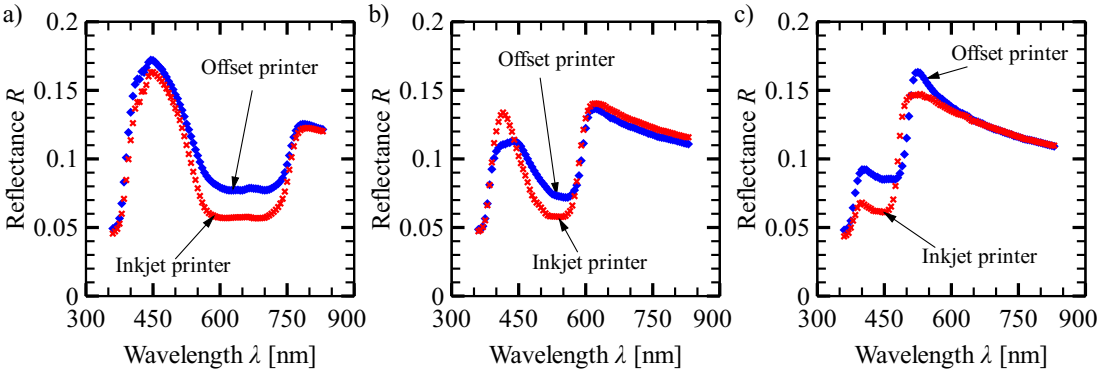

Figure 4.11: Measured reflectance spectra of a single-cell PV module covered with a FPLD50 and imprinted in 100% print coverage (a) cyan, (b) magenta and (c) yellow using an inkjet (red crosses) and an offset (blue diamonds) printer.

This study shows that using different inks and printing techniques results in slightly

different appearances and in particular reflectance spectra for nominally identical printing parameters such as 100% coverage of yellow. If an unknown printer or ink is used for imprinting textiles for CoTex modules, a variation of different test modules should therefore be made and analyzed again so that there are no surprises in the result of the targeted CoTex modules.

4.2.3 EQE and short-circuit current of customized modules

Along with the appearance of the colored PV modules, the energy yield is of decisive importance for architects, homeowner and other stakeholders. In this section, the effect on energy yield of different materials, print coverage and printing techniques is investigated by measuring the *EQE* or the short-circuit current of different CoTex modules.

For this purpose, 27 inket printed samples were analyzed. These are the FPLD40, FPLD50 and FPLD65 materials which were printed with cyan, magenta and yellow respectively at 100%, 70% and 50%. All samples were non-permanently bonded to the same single-cell PV module for each measurement. I measure the *EQE*s of all samples and calculate the J_{SC} according to Eq. 2.18.

Figure 4.12 shows the measured *EQE* of CoTex modules with different colors on the FPLD40 with 100% print coverage (a), different print coverages of magenta with the FPLD50 (b) and different material densities without printing (c), compared to a PV module without a CoTex layer (reference). In the visible wavelength range, the *EQE* depends on the printed color, whereas in the near infrared range, the values of the measured *EQE*s differ by less than 0.02 (a). This wavelength range is apparently not affected by the inks. It is evident, that an increase in print coverage (b) or material density (c) reduces the *EQE*.

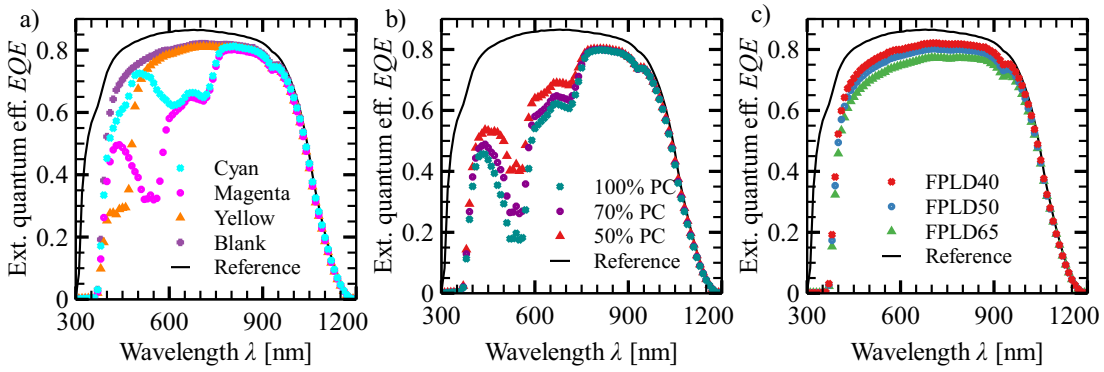

Figure 4.12: Comparison of the measured *EQE*s of the PV module laminated with a FPLD40, imprinted in different colors with 100% print coverage (a), laminated with a FPLD50 with different print coverages (PC) (b) and laminated with different textiles (c). The reference is the PV module without a top layer (black line).

Figure 4.13 shows the ratios of the calculated J_{SC} of all measured samples with regard to 37.17 mA cm^{-2}, the calculated J_{SC} of the single cell module without a CoTex layer. The calculated J_{SC} of the PV module with a top layer system, but no textile

(Ref. 2), shows a loss of 2% compared to the reference. A further 6% (FPLD40), 8% (FPLD50) or 11% (FPLD65) of the J_{SC} is lost by the addition of an unprinted nonwoven fabric. Printing a color results in additional losses of the J_{SC}. Printing cyan in 100% print coverage drops the current by 21%, magenta by 32% and yellow by 14% of the initial J_{SC}.

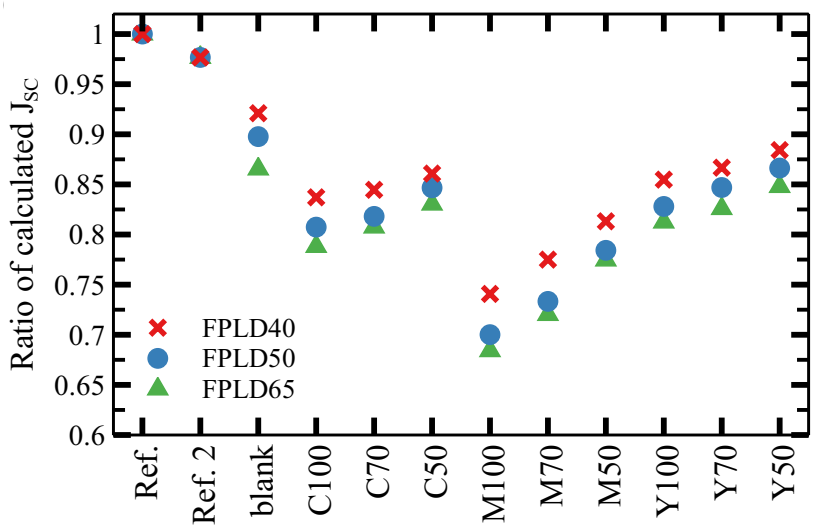

Figure 4.13: Ratios of the calculated short-circuit current density of the PV module covered with a top layer, but without a textile (Ref. 2) and FPLDs 40, 50 and 65, blank and imprinted with cyan (C), magenta (M), yellow (Y) in print coverages of 100%, 70% and 50% with regard to the single cell module without a CoTex layer (Ref.).

The reflectance measurements have already shown that, in addition to the selection of the material and the printing parameters, the printing technique and the inks must also be considered.

Equivalent to the reflectance measurements, the *EQE* was measured from a single-cell module that was non-permanently connected with a FPLD50 printed by an inkjet and an offset printing system in 100% cyan, magenta and yellow (Fig. 4.10). Figure 4.14 shows the measured *EQE*s of the six samples. The areas where the samples printed using the offset print showed lower reflectance have higher *EQE* than the samples printed using an inkjet printer. This means that these samples can generate a weaker color impression but a higher energy yield.

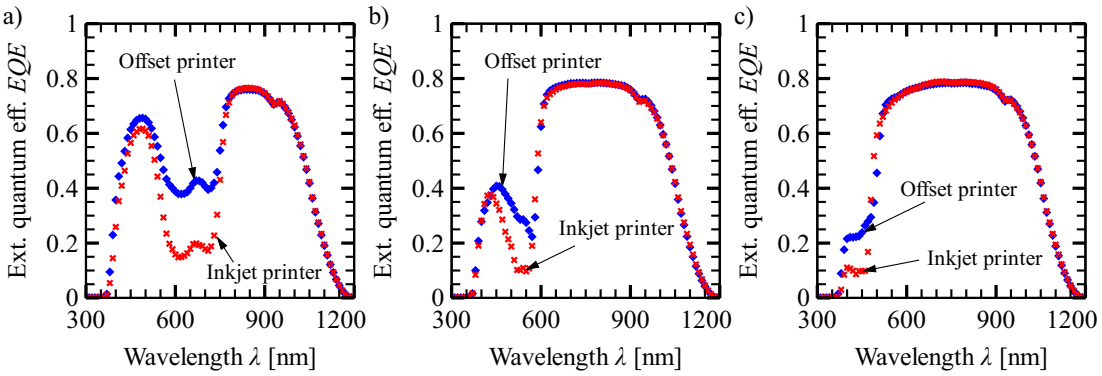

Figure 4.14: Measured *EQE* of a single-cell PV module covered with a FPLD50 and imprinted in 100% print coverage (a) cyan, (b) magenta and (c) yellow using an inkjet (red crosses) and an offset printing system (blue diamonds).

Figure 4.15 summarizes the results from this section, showing once again the photographs from figures 4.8-4.10, this time with the respective relative short-circuit current densities compared to the single-cell module without a CoTex layer. The J_{SC} of the CoTex modules in fig. 4.15 d) and e) was determined using a flasher. In this method, the entire area is illuminated, whereas in the *EQE* measurement only a 20×20 mm^2 area is illuminated. In the case of very inhomogeneous or structured materials, a measurement on a small partial area can lead to large deviations compared to the J_{SC} of the entire module.

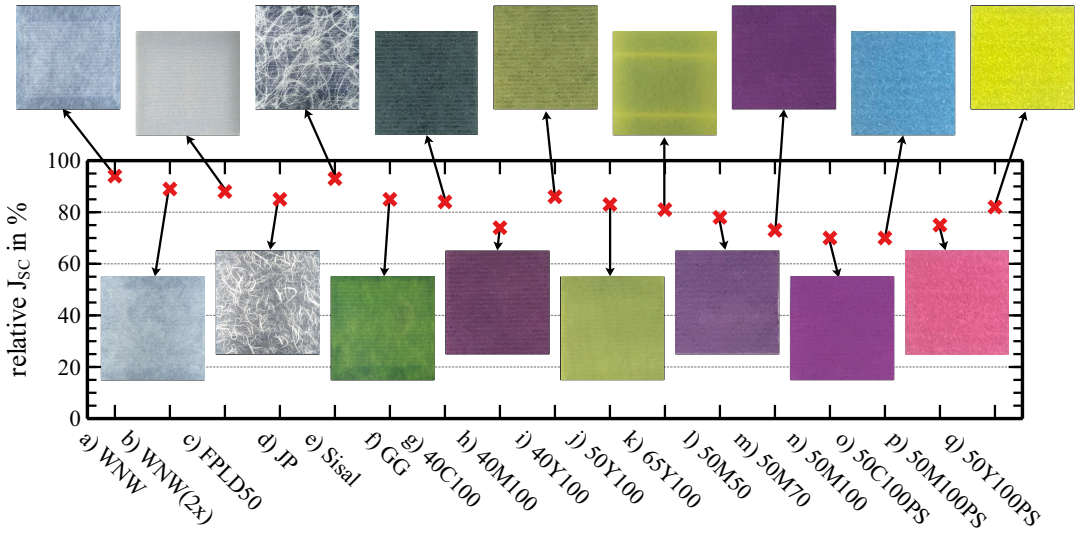

Figure 4.15: Shown are photographs and the respective relative short-circuit current density $J_{SC,rel}$ of CoTex modules fabricated with the following textiles: a) a white nonwoven fabric (WNW), b) 2 layers of a white nonwoven fabric, c) plain FPLD50, d) Japanese paper, e) sisal, f) 6 layers of green gauze, FPLD40 inkjet printed with g) cyan, h) magenta and i) yellow in 100% print coverage; j) FPLD50 and k) FPLD65 both imprinted using an inkjet printer with yellow in 100% print coverage; FPLD50 inkjet printed with magenta in l) 50%, m) 70% and n) 100% print coverage; FPLD50 imprinted using an offset printing system in 100% print coverage with o) cyan, p) magenta and q) yellow.

The studies on the appearance and J_{SC} of the different CoTex modules show two key aspects:

1. The CoTex technique allows the production of individual PV modules in any basic color and pattern with a reasonable loss of energy yield of less than 31.5% compared to a reference module.

2. Both the appearance and the PV yield depend strongly on the material used, the printing technique and the print coverage. Therefore, the simulation of the digital prototype presented in Chapter 5 is an important tool to prepare the fabrication of a CoTex module.

4.2.4 Durability and outdoor test

In addition to appearance and energy yield, the durability and performance of the CoTex PV modules in real outdoor operation is crucial, as the colored PV modules are expected to operate for at least 20 years. These aspects are investigated in this section.

Durability test in the climate chamber

The structure of CoTex BIPV modules needs to be weather-resistant enough to remain stable after years of field exposure. A standard PV module usually guarantees a lifetime of more than 20 years [23].
I investigate with the damp-heat and humidity-freeze test if the permanently laminated CoTex layer is weather-resistant, which means that no delamination or other physical damage occurs. Additionally, I analyze the influence of the test on appearance and energy yield of the CoTex module and compare it to a reference module.
Figure 4.16 shows photos of the two modules before the start of the durability test and after 1200 hours of damp-heat and 200 humidity-freeze cycles (see sec. 4.1.3). The reference module has changed significantly due to glass corrosion. The vertical line of glass corrosion on the right side of the module was caused by the sample holder during testing. No glass corrosion occurs on the CoTex module because the front glass is protected by the CoTex layer. However, the white tone of the CoTex module appears faded and more translucent after the durability test.

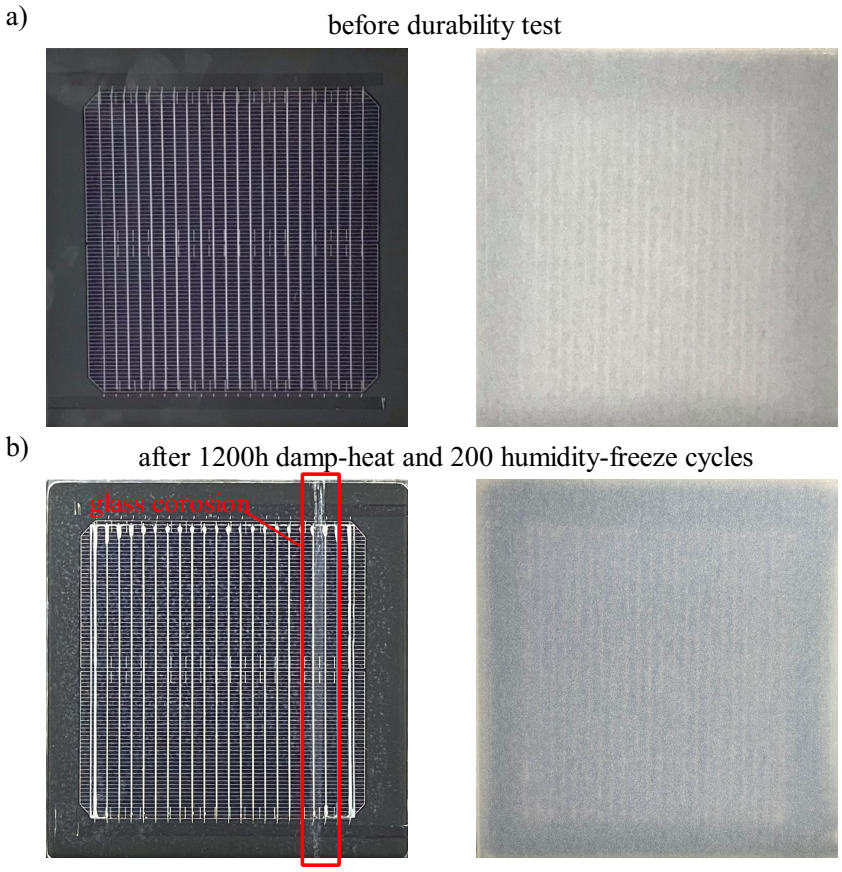

Figure 4.16: Pictures of two identical single-cell PV modules, one is permanently laminated with a CoTex layer which contains a blank FPLD50. a) shows the modules before the durability test in the climate chamber and b) shows the modules after 1200 h damp-heat and 200 humidity-freeze cycles.

The *EQE* of the reference module is hardly changed by the durability test, the *EQE* of the CoTex module decreases slightly in the range from 300 nm to 550 nm (Fig. 4.17 a). It becomes more obvious by considering the ratio of the measured *EQE*s before and after the durability test (Fig. 4.17 b). The ratio $r_{\mathrm{EQE,\,ref.}}$ of the *EQE*s of the reference module scatters only in the UV and the Infrared (IR) range, but there the *EQE* is also close to zero. With the ratio $r_{\mathrm{EQE,\,CoTex}}$ of the CoTex module, in addition to the scattering in the UV and the IR range, significantly lower *EQE* values can be observed. At a wavelength of 400 nm, the *EQE* is 10% lower after the durability test. The difference decreases until the ratio of the measured *EQE* reaches the value 0.99 at a wavelength of 660 nm. It is conspicuous that $r_{\mathrm{EQE,\,ref.}}$ attains values above one from a wavelength of 700 nm and $r_{\mathrm{EQE,\,CoTex}}$ from 1000 nm. It is apparent from Fig. 4.17 a) that the *EQE*s of both, the reference and the CoTex samples, before and after the durability test decrease sharply in this range and approach zero. There are a few values above one in Fig. 4.17 b) at a wavelength range between 330 nm and 370 nm and above 1050 nm. Here, the EQE is low and due to the small signal strength the noise is proportionally larger. Therefore, I interpret the values of $r_{\mathrm{EQE}} > 1$ as a result of the measurement inaccuracy.

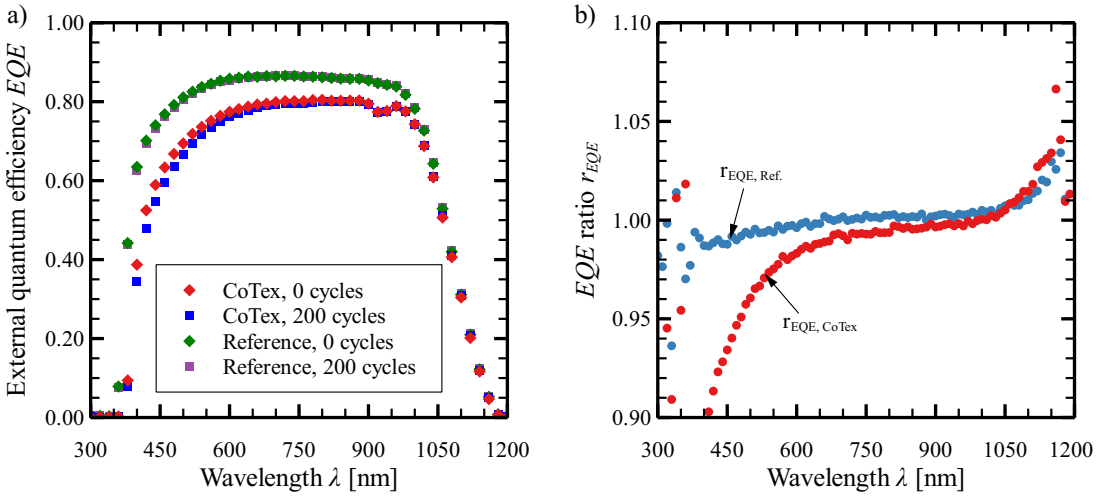

Figure 4.17: a) Measured *EQE*s of the reference and CoTex module before and after completing the durability test. b) Ratio r_{EQE} of *EQE*s shown in a).

Table 4.2 shows the J_{SC} calculated from the *EQE* measurements. As can already be seen in Fig. 4.17, hardly any changes occur in the reference module due to the durability test, the J_{SC} is reduced by 0.006 mA/m² only. In contrast, the slightly lower *EQE* in the wavelength range below 750 nm reduces the J_{SC} of the CoTex module by 0.56 mA/m² compared to the J_{SC} before the durability test. The ratio between the CoTex and the reference module decreases by 1.6% by the durability test.

Table 4.2: Comparison of the calculated J_{SC} before and after the durability test in the climate chamber. The bottom row shows the ratio between the calculated J_{SC} of CoTex and reference module.

Sample	J_{SC} calc. before	J_{SC} calc. after	Reduction
Reference module	34.58 mA/m²	34.58 mA/m²	0.006 mA/m²
CoTex module	31.37 mA/m²	30.81 mA/m²	0.56 mA/m²
Ratio	0.907	0.891	0.016

Although the CoTex module experiences a significantly higher drop in J_{SC} due to exposure in the climatic chamber, I rate it to have passed the durability test as there was no delamination, no bubble formation between the front glass of the module and the CoTex layer, and no other physical damage.

4.2.5 UV-stability

Since the main reason for the development and purchase of colored PV modules is their attractive appearance, the aesthetics of these PV modules is of particular importance to stakeholders. Therefore, it has to be guaranteed that the colors of the modules do not change even after years of UV exposure.
The UV-curable inks of Anapurna FB2540i LED printer, which were used for the inkjet printing, have been designed for outdoor usage and are therefore based on light-stable

color pigments. In addition, the UV dose reaching the pigments is reduced by the UV-absorbing encapsulation material that we use to mount the imprinted nonwoven fabrics onto the PV module. As a result, there is barely any change in color detectable after exposure to a UV dose equivalent to 20 years outdoor exposure in Potsdam.
Figure 4.18 shows pictures before (a) and after (b) UV exposure of the single-cell PV module on which the UV stability test was carried out. After UV exposure the colors appear slightly more translucent, as the fingers of the solar cell are slightly more visible underneath the CoTex layer.

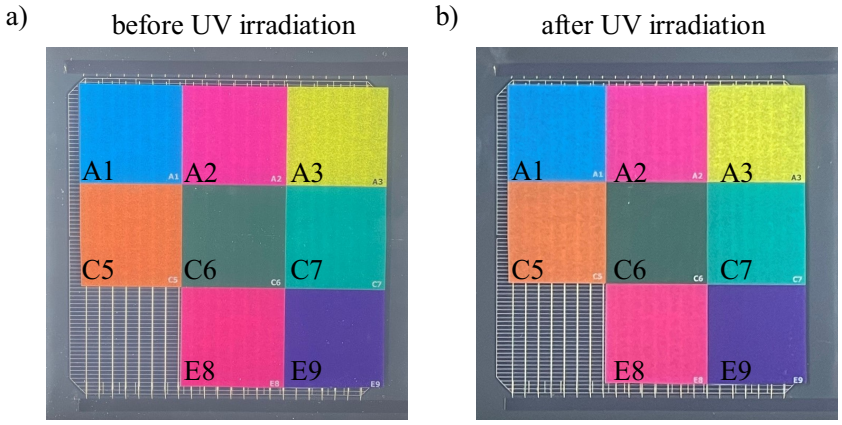

Figure 4.18: a) Before the start of the UV test. b) After 3250 hours UV exposure in the UV chamber.

Figure 4.19 shows the measured reflectances R before and after UV irradiation of the nine colored boxes examined. In most areas there are hardly any differences between the two reflectance spectra. Differences above 0.01 only appear for three samples and at wavelengths around 400 nm, these are a maximum of 0.018 for sample A1 (Fig. 4.19 a), 0.021 for sample A2 (Fig. 4.19 b) and 0.017 for sample E8 (Fig. 4.19 h).

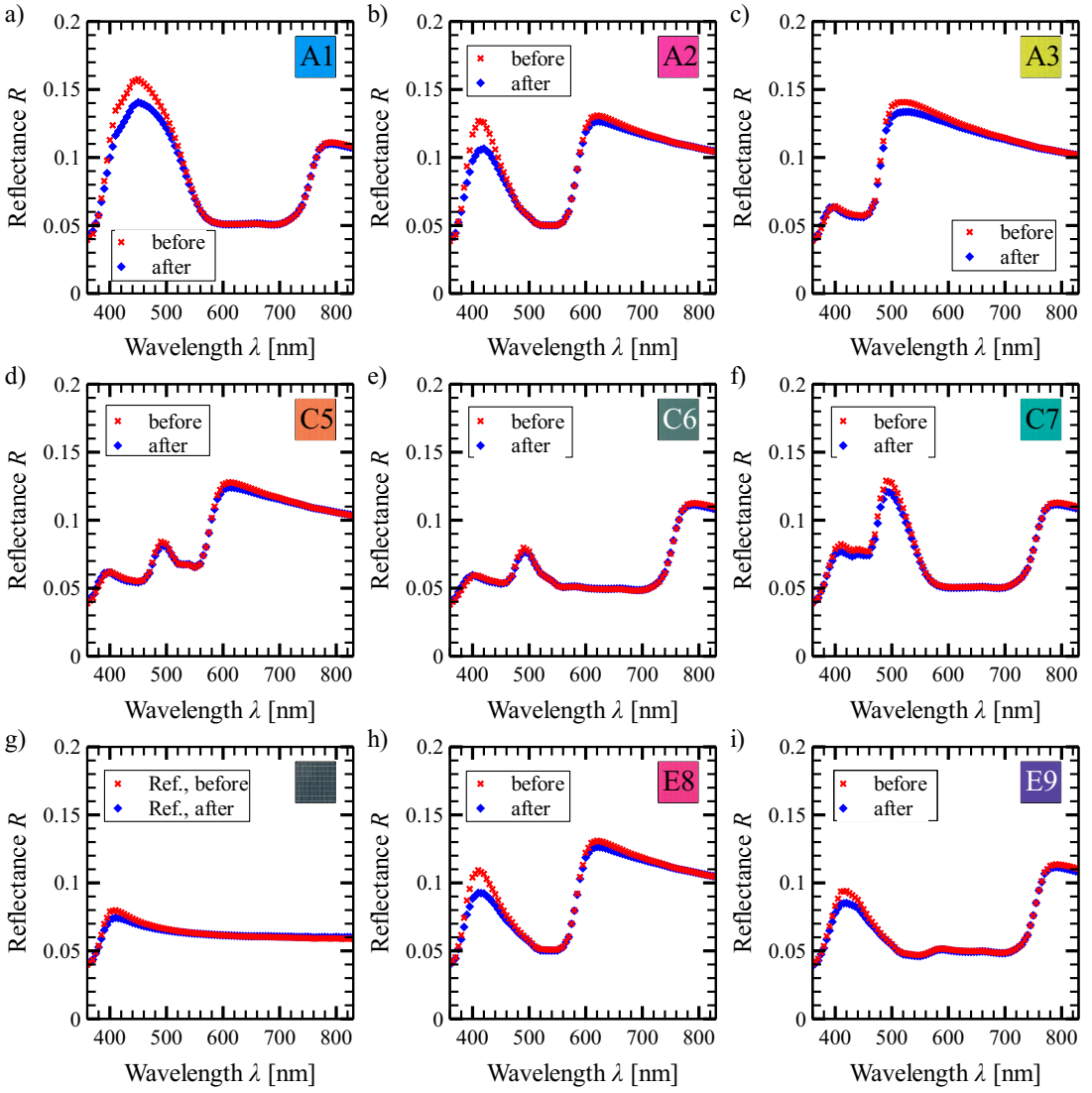

Figure 4.19: The measured reflection spectra before the start of the UV test (red crosses) and after 3250 hours in the UV chamber (blue diamands) of a CoTex PV module, imprinted with colors a) A1, b) A2 c) A3, d) C5, e) C6, f) C7, h) E8, i) E9. As control, one box of the PV module was covered with the CoTex stack but without an imprinted textile (g). The colored square in the lower right corner shows photographs of the printed samples before the UV test or, in the case of the reference, a cutout of the solar cell.

Figure 4.20 shows the measured *EQE*s before and after UV irradiation of the single-cell module with the nine different boxes. Similar to the reflectance measurements, the *EQE*s show only small differences. After UV irradiation, the *EQE*s for the colored boxes in Figure 4.20 are below the *EQE* measured before UV irradiation in the entire wavelength range examined. On average, the difference is 0.0023. Larger differences are evident in the area around a wavelength of 400 nm for colors A1 and E8 with a maximum difference of 0.06 and 0.11, respectively. The *EQE* of the box without a textile also decreased in the entire wavelength range after UV irradiation, but only by 0.0018 on average.

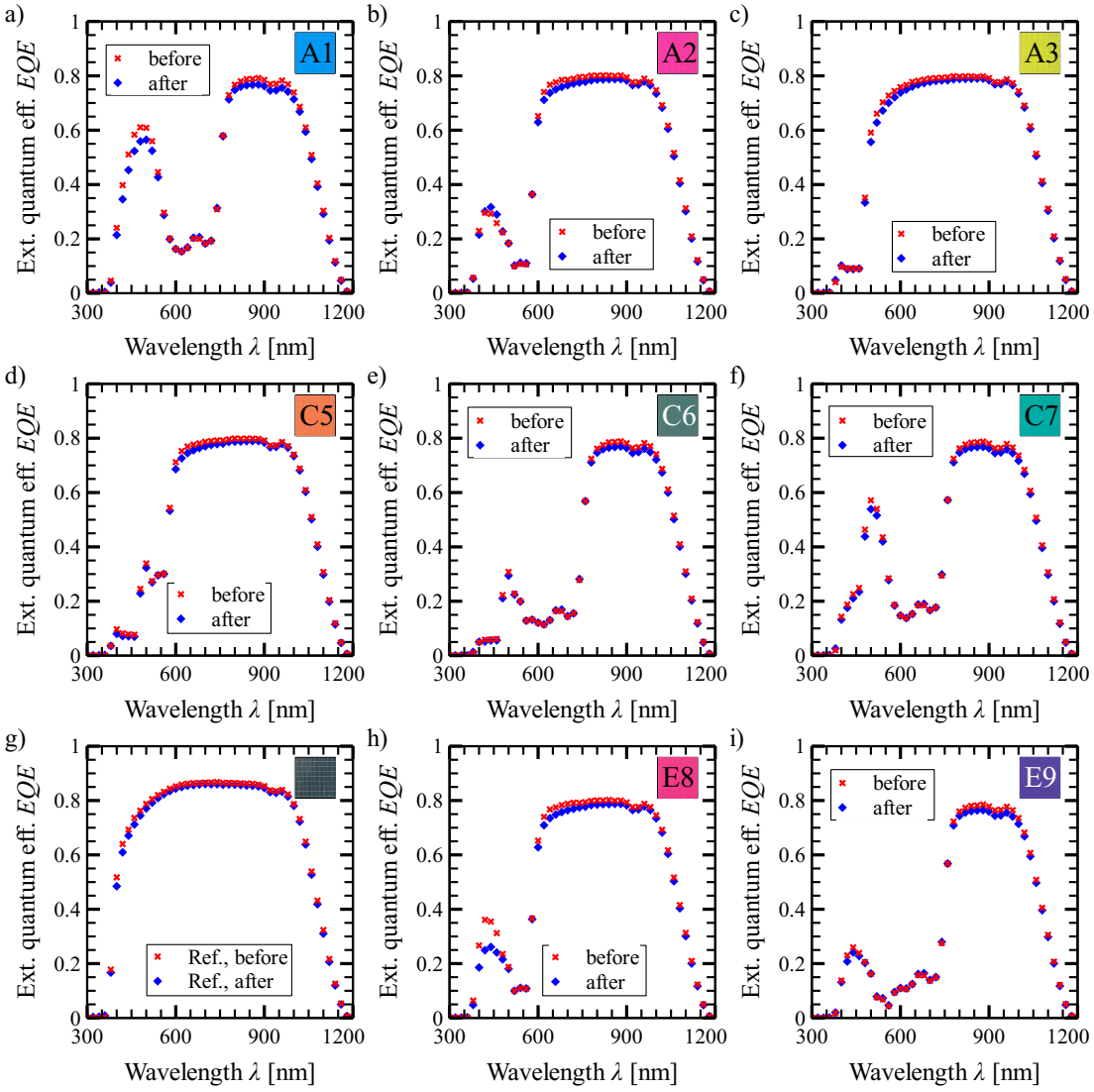

Figure 4.20: The measured *EQE* before the start of the UV test (red crosses) and after 3250 hours of UV exposure (blue diamands) of a CoTex PV module, imprinted with colors a) A1, b) A2 c) A3, d) C5, e) C6, f) C7, h) E8, i) E9. As control, one box of the PV module was covered with the CoTex stack but without an imprinted textile (g). The colored square in the top right corner shows photographs of the printed samples before the UV test or, in the case of the reference, a cutout of the solar cell.

Figure 4.21 a) shows the color differences ΔE_{00} calculated from the reflection spectra of the nine boxes before and after UV exposure. From the reflection measurements in Fig. 4.19 it was already evident that the greatest differences are to be expected in the boxes A1, A2 and E8. This is confirmed by the color differences $\Delta E_{A1} = 1.57$, $\Delta E_{A2} = 1.45$ and $\Delta E_{E8} = 1.18$. The average color difference of the eight colored boxes is $\overline{\Delta E}_{00} = 0.99$ and thus below the color difference $\Delta E_{Ref.} = 1.18$ of the reference patch. The respective J_{SC} of a color box was determined from the measured *EQE*s. Figure 4.21 b) shows the ratio $r_{J_{SC}} = \frac{J_{SC,\,after\,UV\,exp.}}{J_{SC,\,before\,UV\,exp.}}$ between the J_{SC} before and after UV irradiation. Color box A1 and E8 show the largest J_{SC} losses with a ratio of $r_{J_{SC},\,A1} = 0.965$ and $r_{J_{SC},\,E8} = 0.965$. On average, the ratio of the colored boxes is $\overline{r_{J_{SC}}} = 0.976$, which is significantly lower than the J_{SC} ratio $r_{J_{SC},\,Ref.} = 0.987$ of the reference box.

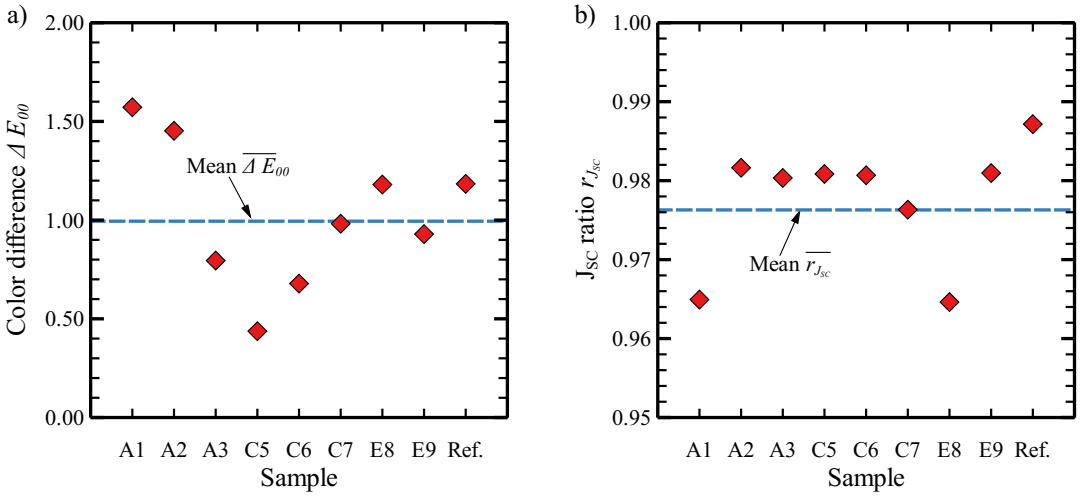

Figure 4.21: a) Color difference ΔE_{00} and b) J_{SC} ratio $r_{J_{SC}}$ of the nine measured boxes on the single-cell CoTex module before and after UV irradiation. In addition to the results of the individual boxes (red diamonds), the mean values $\overline{\Delta E_{00}}$ of the eight colored boxes are plotted (dashed blue line).

This test was primarily concerned with the question of whether the appearance of the colored CoTex modules changes significantly due to UV irradiation. With $\overline{\Delta E_{00}} = 0.99$ on average, the color difference is hardly noticeable, so the CoTex module passed this test.

4.2.6 Long-term outdoor application

To verify whether the laboratory measurements on the single cell modules are transferable to commercial standard modules, a CoTex module is compared with a standard PV module and the single cell module. Figure 4.22 shows a greyish CoTex module (marked 2) and an identical standard module (marked 1) on the façade.

Figure 4.22: Standard PV module (1) and a greyish CoTex module (2) on a façade.

Table 4.3 compares the J_{SC} and energy yield of single cell modules with and without

a white FPLD65 CoTex layer and commercial standard modules with and without a white FPLD65 CoTex layer (Fig. 4.22 (1) and (2)). The modules without a CoTex layer are the reference modules. Using the measured *EQE* of a single cell module non-permanently attached to a white, laminated FPLD65, the J_{SC} loss due to the CoTex layer was determined to be 14.1%. The comparison of the flasher measurement resulted in a power loss of 14% of the CoTex module. The outdoor measurement of a time period of 12 months (09.2019 - 08.2020) found a 14.5% lower energy yield of the CoTex module.

Table 4.3: Comparison between a CoTex module and a reference module in terms of: 1. the short-circuit current density J_{SC} *calc.* calculated from the measured EQE using single-cell modules, 2. the energy yield in measured in a flasher 60-cell-modules, and 3. the cumulative energy yield after a 12-month outdoor measurement of the 60-cell modules.

Sample	J_{SC} calc.	Flasher	Outdoor
Reference module	34.4 mA	299.56 W	179.8 kWh
CoTex module	29.56 mA	257.58 W	153.7 kWh
Reduction	14.1%	14%	14.5%

The results of the power losses through this CoTex layer differ by less than 0.5% when comparing flasher and outdoor measurements. This shows that the *EQE* measurements on single-cell modules are transferable to standard modules and also that optical coupling using liquid Paraffin instead of permanent lamination does not lead to significant deviations.

Figure 4.23 a) shows the cumulative energy yield of the reference E_{ref} and the CoTex module E_{CoTex}, measured from June 2019 to March 2021 and plotted with respect to time of the day. Especially during midday, the reference module produces significantly more energy than the CoTex module. By inspecting the monthly ratio $r_{CoTex/ref} = \frac{E_{CoTex}}{E_{ref}}$, an angular dependence of the ratio is evident. $r_{\mathrm{CoTex/ref}}$ varies periodically between 0.82 and 0.88 (blue dashed), exactly opposite to the periodic variation of the sun position dependent AOI (green dashed). In the winter months, when the sun's incidence is shallow, the AOI on the vertically mounted façade modules is smaller and E_{CoTex} is larger. In the summer months, E_{CoTex} is smaller with a larger AOI. This result on angle dependence which is important for the yield prediction will be discussed in chapter 6.

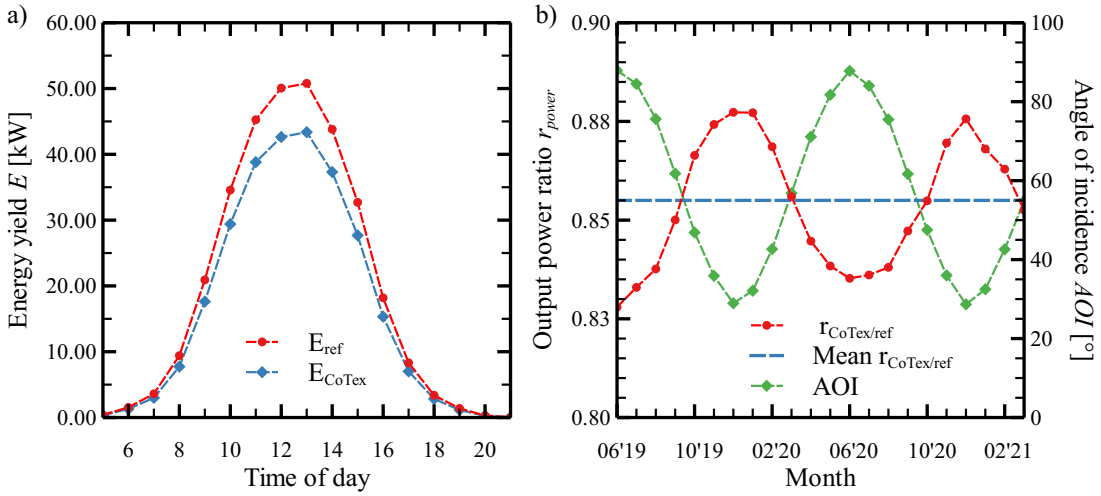

Figure 4.23: a) Cumulated energy yield of a greyish CoTex (blue dashed) and a reference (red dashed) module, measured over a period of 22 months. b) Ratio of the measured energy yield of the CoTex and the reference module (red dashed), the overall mean ratio (blue dashed) and the AOI (green dashed).

4.2.7 Cost estimation

For an application in the industry, the costs are also decisive. The additional material costs for CoTex modules depend on the choice of the textile and whether it is printed or blank. In addition to the textile, two layers of encapsulation material and the weather-resistant top layer are required. For a conventional glass-glass module with a black backsheet, the manufacturing prices are 66.83 €/m^2 and 0.34 €/Wp [55]. Depending on the design, the costs for the CoTex layer are 7 €/m^2 to 15.2 €/m^2 and would thus increase the material costs of a conventional module by 11% to 23%. If a greyish CoTex design with a J_{SC} loss of 11% is chosen, the power production costs (€/Wp) increase by 35%. [36] However, this calculation is rather conservative and considers prices for the production of a single module. In particular, the necessary material and printing costs would drop significantly for larger quantities.

4.3 Conclusion of Chapter 4

The CoTex method allows to alter the appearance of PV modules by laminating any textile. The use of imprinted textiles enables a high degree of individualization and opens the door to printing complex graphics. Appearance and yield are highly interdependent. With the CoTex method it is possible to balance between them by varying the material and the print coverage. For example, the use of FPLD40 allows a high energy yield, but the solar cells are not completely masked. When using FPLD65, the solar cells are fully masked and the colors are richer, but the loss in J_{SC} is in the range of 13.9% to 31.5%. The lowest loss in the J_{SC} observed in this work was 7.9% for a blank FPLD40, which resulted in a greyish appearance that could be attractive for BIPV. The outdoor durability was demonstrated in terms of stability of the lamination, functionality and appearance.

Chapter 5

Simulation of a digital prototype

The appearance of building-integrated PV modules is being altered to meet the needs of homeowners or other stakeholders. Accordingly, the purpose of this modification is only fulfilled if the requirements of the stakeholders are met. For commercial application of the CoTex technique, it is necessary that appearance and yield can be adjusted and predicted as accurately as possible even before production. Figure 5.1 shows how the appearance of an imprinted textile changes after lamination and again after application onto a PV module. Even though this process is completed in one step in the production of CoTex modules, the illustration shows that the appearance is changed by two factors: First, the optical properties of the printed material are changed by the lamination process. Second, the printed material appears significantly darker after it has been laminated onto the PV module due to the solar cells in the background. This alteration in appearance means that it is not straightforward to know what a particular printed color will look like as a finished CoTex module. The simulation of a digital prototype presented in this chapter allows the prediction of the appearance and energy yield of CoTex modules with different textiles printed in any combination of the three primary colors cyan, magenta, and yellow.
I have already published the methods and the results of the simulation using the offset-printed FPLD50 samples in reference [35].

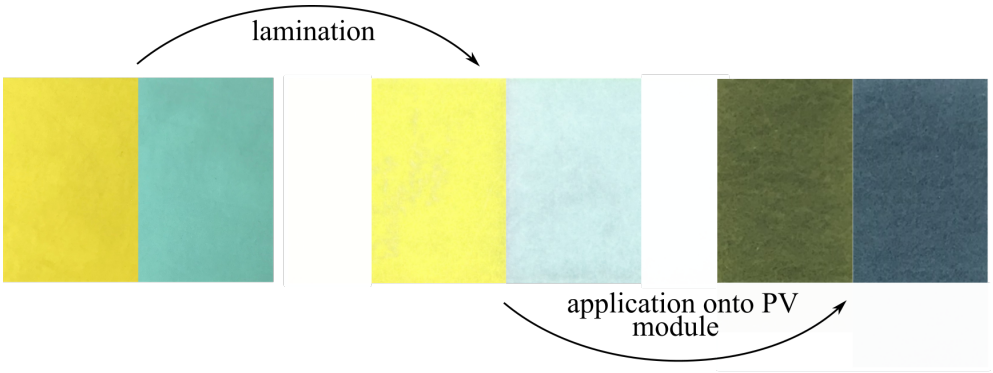

Figure 5.1: Photographs of a FPLD65 imprinted with cyan and yellow in 100% print coverage directly after printing (left), laminated (center) and permanently laminated onto a PV module (right).

The accuracy and transferability of the simulation is examined using FPLD40 and FPLD50 imprinted using an inkjet printer, a FPLD50 imprinted with an offset printer and a colored semitransparent foil.
The chapter is divided into four sections, presenting respectively the measurements and the simulations for inkjet-printed FPLD40 (I40), the inkjet-printed FPLD50 (I50), the FPLD50 imprinted by an offset printer (O50) and the colored foil (CF).

5.1 Sample preparation and simulation methods

In this section, the procedure and methods for the simulations of the digital prototype are presented. The precise explanations of the simulations can be found in the theory section 2.2.

5.1.1 Coloring of the samples

In addition to the printing techniques for printing the FPLD presented in Chapter 4.1.2, a semi-transparent film made of polypropylene is now printed as a further sample. I used a Samsung XPress C410W laser printer for imprinting the semi-transparent foil. Figure 5.2 shows a color pattern with 59 different colors, which I print on the materials used. These are different combinations of the primary colors cyan, magenta and yellow with the respective print coverages of 0%, 25%, 50%, 75% and 100%. The eight colors in row A provide the basis for the simulation of the digital prototype. The other 51 color variations are used for experimental validation of the simulation.

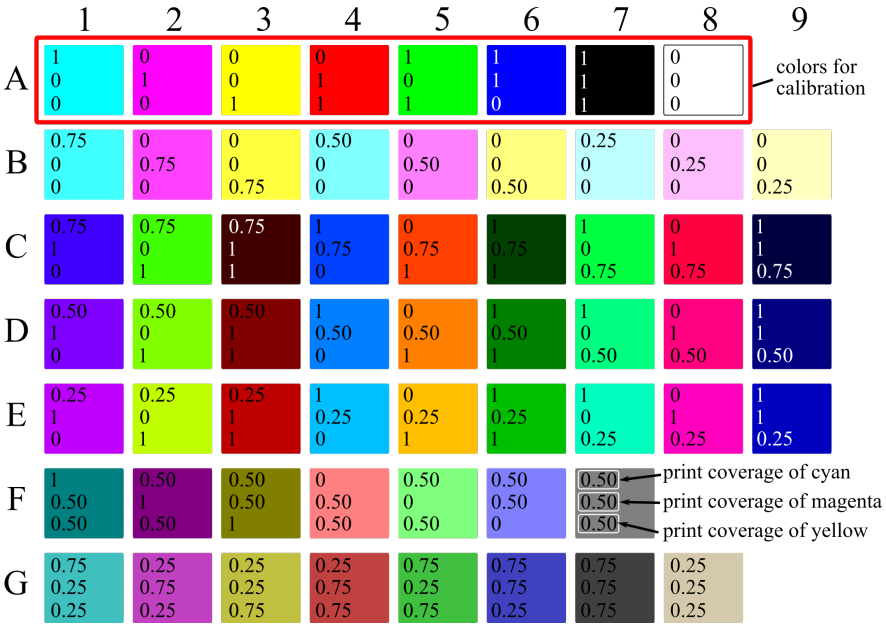

Figure 5.2: Print pattern for the calibration and the validation of the simulation. The numbers in the colored boxes indicate the print coverage of the individual inks. The upper number denotes the print coverage of cyan ink, the middle number for magenta, and the lower number for yellow.

5.1.2 Simulation of the digital prototype of colored BIPV modules

The appearance and yield simulations are based on the equations presented in section 2.2. Figure 5.3 shows the procedure of the simulations. For preparation, the reflectance and *EQE* of the eight colored samples from row A (fig. 5.2) must be measured. The measurement methods are equal to those presented in chapter 4.1.
Based on the measurement of those eight colored samples, the appearance and PV yield can be simulated for any combination of the print parameters CMY. The print parameters refer to the degree of print coverage of the inks cyan (C), magenta (M) and yellow (Y). The print coverage ranges from 0% to 100%. The *EQE* and the reflectance are simulated for the selected print parameters and material. From the *EQE*, the relative J_{SC} with respect to the J_{SC} of a reference module is determined and thereby the expected energy yield is estimated (see sec. 2.2.3). Using equation (2.1) and the simulated reflectance, I determine the color coordinates in XYZ and L*a*b* color space.

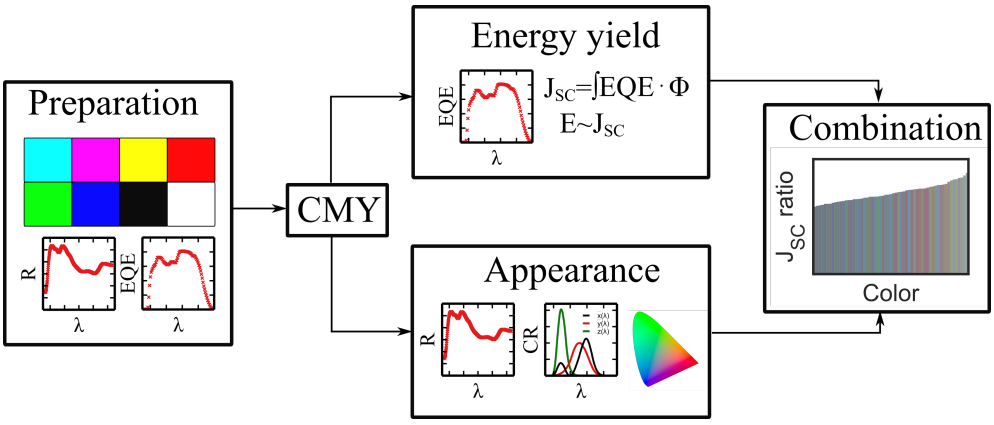

Figure 5.3: Procedure of the simulation of the appearance and energy yield of colored BIPV modules.

We are able to simulate the appearance and short-circuit current density for all possible combinations of the three inks cyan, magenta and yellow printed on a textile and attached to the single-cell module. To get a small overview only, I simulate the appearance and J_{SC} for all combinations of cyan, magenta, and yellow in 0%, 25%, 50%, 75%, and 100% print coverage, resulting in 125 different colors for each sample type. I plot the relative short-circuit current density $J_{SC,\ rel.} = \frac{J_{SC,\ CoTex\ color}}{J_{SC,\ reference}}$, with $J_{SC,\ reference}$ of the the single-cell module without a CoTex layer in a bar plot, where the bars have the specific color.
To get a larger picture of the potential colors, I also simulate all combinations of the three inks for each sample type with print coverage from 0% to 100% in 10% steps, resulting in 1331 colors.

5.1.3 Correction of ink spreading

Ink spreading can cause the print result to deviate from the planned print. If the effects of ink spreading are known, the ink spreading can be taken into account by correction functions when setting the print parameters. I use the model of Hersch *et al.* [43] to determine the correction functions. Thus, I use the reflectance measurements of the samples from row B to E, where in each case the print coverage a_i of one ink varies between 25%, 50%, or 75%, and the print coverage a_j and a_l of the other two inks are printed fixed at 0% or 100%. For each of these 36 colors, I check with which printing parameters a_i', a_j', a_l' the simulated reflectance spectrum best matches the measured reflectance spectrum. Here, the print coverage of the ink a_i' is varied with the parameter q between 0% and 100% in 1% steps. The print coverage of the other two inks remains at 0% and 100% respectively as for the manufactured samples, accordingly $a_j' = a_j$ and $a_l' = a_l$. We find the best match by considering the color difference ΔE_{00} between measured and simulated reflectance spectra:

$$a_i' = \underset{0 \leq q \leq 1}{\arg\min}\, \Delta E_{00}\big(R_{\text{sim}}(q, a_j, a_l, \lambda), R_{\text{meas}}(a_i, a_j, a_l, \lambda)\big) \tag{5.1}$$

These 36 effective print coverages a_i' are grouped into 12 sets of three a_i' each. From these sets, 12 continuous ink spreading functions f_i are created using linear interpolation. It is assumed that effective and planned print coverage are identical at the values 0% and 100%. With the help of these functions, the planned printing parameters can be corrected in order to achieve the smallest possible deviation between the printed color and the target color. I investigate the effects of ink spread correction solely on the inkjet-printed FPLD50 samples.

5.2 Visual assessment of the samples

Figure 5.4 shows the optical microscope image (top row) and a camera shot (bottom row) of samples printed with 50% magenta and 50% yellow of the four sample variations I investigated. A significant difference can be seen in the microscope images: In offset-printed samples the typical halftone printing pattern is clearly recognizable. The inkjet-printed samples show a partially permeable layer on top of the fabric. Only underneath this permeable layer does the halftone print pattern become noticeable. However, this is not as distinctly symmetrical as in the offset-printed samples. In the case of the printed foil, the ink blobs are much smaller and a stripe pattern is visible. In the images in the bottom row, similar colors can be seen in samples a) to c). The printed film is much more transparent than the FPLD, so the structure of the solar cell underneath is visible. Since the halftone printing process is significantly more evident in the samples printed using an offset printing system and the colored foil than in the inkjet-printed samples, it is to be expected that the simulation will also achieve higher accuracy with these samples.

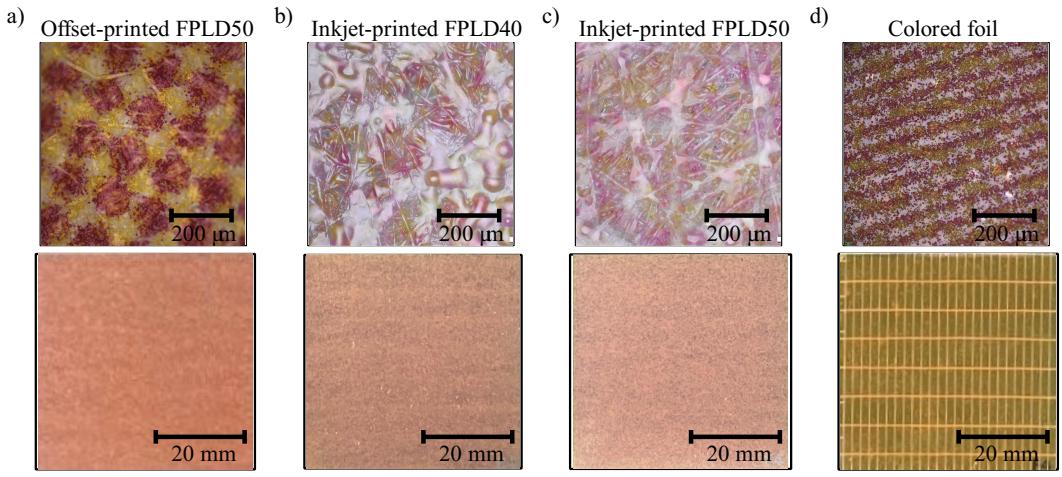

Figure 5.4: Images of the a) O50 [35], b) I40, c) I50 and d) CF samples, imprinted with 50% magenta and 50% yellow. First row shows images obtained with an optical microscope, images in the second row are obtained with a digital camera.

Figure 5.5 shows photos of the four groups of samples. In the case of the I40, I50 and CF samples, all 59 colors of the print pattern (Fig. 5.2) were examined. In the case of the O50 samples, only 37 colored samples were available. These are colors A1-A8, B1-B9, C1-C4, D1-D4, E1-E4, F1-F4 and G1-G4 from the print pattern shown in Fig. 5.2.

Please note that the samples were attached to the silicon half-cell module for this overview only. The FPLDs were non-permanently bonded to the module with Paraffin, and the printed film is self-adhesive. As described above, all measurements are performed with the single-cell module (Fig. 4.2).

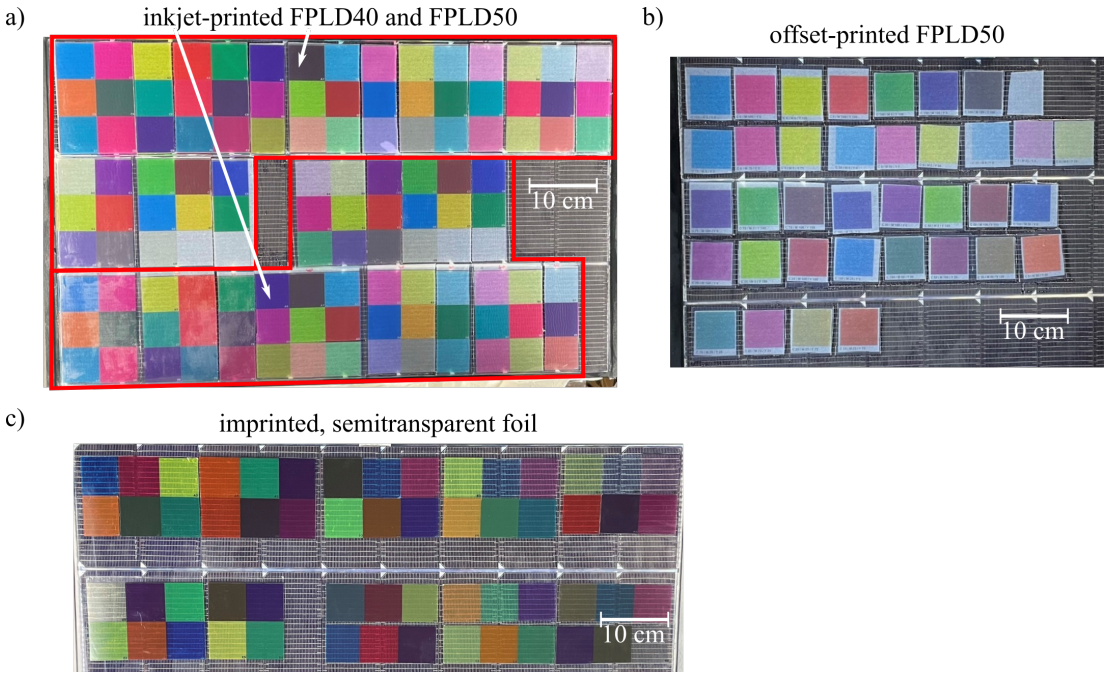

Figure 5.5: Photos of the colored samples used to calibrate and validate the simulation of the digital prototype. a) shows the FPLD40 and FPLD50 printed by an inkjet printer, b) the FPLD50 printed using an offset printer [35], and c) the colored semitransparent film.

5.3 Simulation of the digital prototype

In this section, the simulation of the digital prototype is presented and, in particular, the accuracy of the simulation is investigated. The procedure for each of the four sample types is as follows:

1. The reflectance and *EQE* of all samples are measured (see section 4.1).

2. The measurement results for the colors from row A in Figure 5.2 are used to calibrate the simulation of reflectance, *EQE* and color of CoTex modules (or modules covered with the colored foil) (see section 2.2).

3. The measurement results for all colors except those in row A are used to validate the simulations. The simulated *EQE*s and reflectance spectra are compared with the measured ones. The color distance ΔE_{00} is used for assessing the accuracy of the color prediction. The ratio $r_{J_{\mathrm{SC}}}$ and the deviation $\Delta r_{J_{\mathrm{SC}}}$ from J_{SC} between measurement and simulation is used to estimate the accuracy of the energy yield simulation. I determine $r_{J_{\mathrm{SC}}}$ and $\Delta r_{J_{\mathrm{SC}}}$ with

$$r_{J_{SC}} = \frac{J_{\mathrm{SC,\,simulated}}}{J_{\mathrm{SC,\,measured}}}, \qquad \Delta r_{\mathrm{J_{SC}}} = |1 - r_{J_{SC}}|\,. \tag{5.2}$$

4. A color diagram with 125 colors and the corresponding J_{SC} is simulated to give an overview of which colors are possible with the respective material and printing technique and with which energy yield. I plot the relative short-circuit current

density $J_{\mathrm{SC,\ rel.}} = \frac{J_{\mathrm{SC,\ CoTex\ color}}}{J_{\mathrm{SC,\ reference}}}$, with $J_{\mathrm{SC,\,reference}} = 33.93$ mA/cm² of the single-cell module (Fig. 4.2) without a CoTex layer.

Table 5.1 shows the fit parameter f_1 and f_2 for the simulation of the EQE, which I determined by comparing the results for $\Delta r_{J_{SC}}$ of the eight colorants:

$$\begin{aligned} f_1 &= \underset{0\leq f_1\leq 1}{\arg\min}\, \Delta r_{J_{SC}}(EQE_{\mathrm{sim}}(colorant, f_1), EQE_{\mathrm{meas}}(colorant, f_1)) \\ f_2 &= \underset{0\leq f_2\leq 1}{\arg\min}\, \Delta r_{J_{SC}}(EQE_{\mathrm{sim}}(colorant, f_2), EQE_{\mathrm{meas}}(colorant, f_2)). \end{aligned} \tag{5.3}$$

This overview shows that there are significant differences due to the type of printing and the choice of ink. For the inkjet-printed samples I40 and I50, the fit parameters differ only by 0.038-0.058 and by 0.022-0.025 from $f_{1,\mathrm{CF}}$ and $f_{2,\mathrm{CF}}$ for CF, respectively. There is a striking contrast to $f_{1,\mathrm{O50}}$ and $f_{2,\mathrm{O50}}$. In this case, the chosen parameters are identical to their counterparts from the reflection model r_{s} and r_{int}.

Table 5.1: Chosen fit parameter f_1 and f_2 for the simulation of the EQE of arbitrary colors.

Samples	I40	I50	O50	CF
f_1	0.937	0.917	0.04	0.975
f_2	0.001	0.004	0.596	0.026

5.3.1 Investigation of samples I40

Figure 5.6 shows the ΔE_{00} between measured and simulated color of the CoTex module with inkjet-printed FPLD40 samples. The mean color difference over all samples is $\overline{\Delta E}_{\mathrm{I40}} = 1.7$. It is striking that the simulation of the colors where only one ink was used (Fig. 5.2, row B) has the smallest distribution with a standard deviation of $\sigma_{\mathrm{I40,\,1}} = 0.57$, but there the highest mean value is reached with $\overline{\Delta E}_{\mathrm{I40,\,1}} = 1.87$. When two inks are used, I determine the variance $\sigma_{\mathrm{I40,\,2}} = 1.09$ and the mean $\overline{\Delta E}_{\mathrm{I40,\,2}} = 1.47$. For three inks, a mean of $\overline{\Delta E}_{\mathrm{I40,\,3}} = 1.84$ is obtained with a variance of $\sigma_{\mathrm{I40,\,3}} = 1.12$.

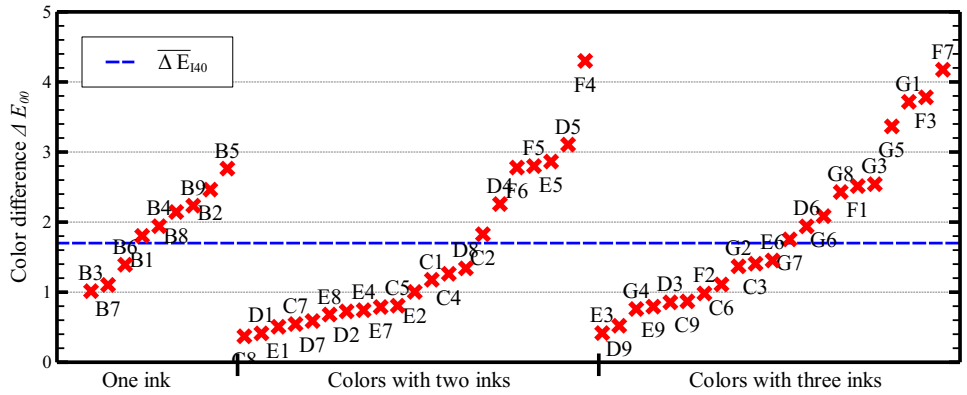

Figure 5.6: Color distance ΔE_{00} between measured and simulated colors of the I40 samples. The labels of the colors refer to the colors in Figure 5.2. The blue-dashed line shows the average $\overline{\Delta E}_{\mathrm{I40}} = 1.7$.

Figure 5.7 shows the measured (blue crosses) and simulated (dotted red line) reflectance spectra of the colors with a) the lowest, b) a moderate and c) the highest ΔE_{00}. The background color of the area below the measured reflectance spectrum represents the measured color, the background color of the area above the simulated reflectance spectrum represents the corresponding simulated color. In Figure 5.7 a) with $\Delta E_{\mathrm{I40,\,C8}} = 0.37$, the measured and simulated reflectance spectra of the color C8 (C: 0, M: 1, Y: 0.75) lie almost exactly on top of each other and no difference between the two colors is perceptible. In Figure 5.7 b), with $\Delta E_{\mathrm{I40,\,B1}} = 1.8$, only small deviations of up to 0.006 between the two reflectance spectra can be observed and no difference can be perceived between measured and simulated color. Figure 5.7 c) shows the largest difference between measurement and simulation with $\Delta E_{\mathrm{I40,\,F4}} = 4.3$. The simulated reflectance spectrum in the range between 460 nm and 520 nm is up to 0.016 higher than the measured reflectance spectrum. Despite the differences in the reflectance spectra, the perceivable color difference is small. The simulated color appears slightly darker than the measured one.

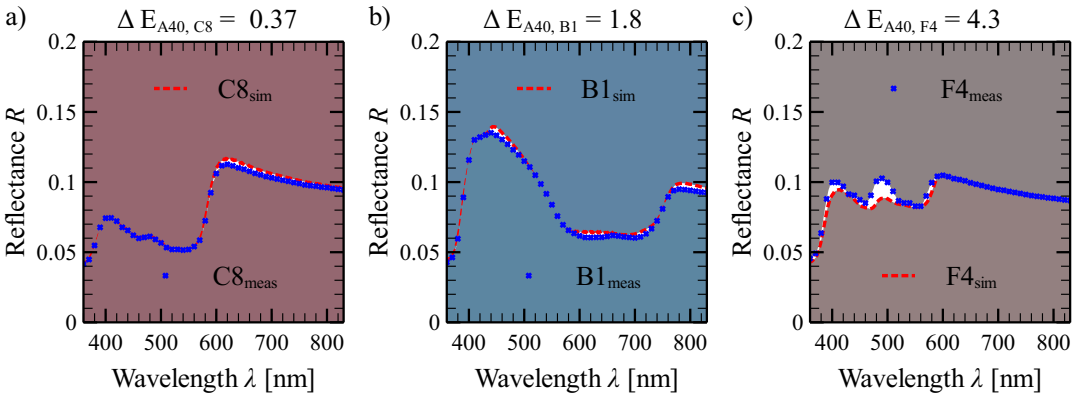

Figure 5.7: Measured and simulated reflectance spectra of samples I40 with the a) lowest, b) a moderate and c) the highest ΔE_{I40}. The background above and below the respective curve is colored in the color determined from the reflectance spectrum. This illustrates the difference between measured and simulated color.

Figure 5.8 shows the deviations of the J_{SC} between measurement and simulation for the inkjet-printed FPLD40 samples. Unlike the color difference in Figure 5.6, the standard and the mean deviation between measurement and simulation for the J_{SC} increase with the number of inks. With one ink only, the mean deviation is $\overline{\Delta r}_{\mathrm{I40,\,1}} = 0.007$ with a standard deviation of $\sigma_{\mathrm{I40,\,1}} = 0.005$. Using two inks, we found a mean deviation of $\overline{\Delta r}_{\mathrm{I40,\,2}} = 0.012$ with $\sigma_{\mathrm{I40,\,2}} = 0.009$. For three inks, the mean deviation increases to $\overline{\Delta r}_{\mathrm{I40,\,3}} = 0.016$ with $\sigma_{\mathrm{I40,\,3}} = 0.012$. Over all samples, the mean deviation is $\overline{\Delta r}_{\mathrm{I40}} = 0.013$ with a standard deviation of $\sigma_{\mathrm{I40}} = 0.01$. The mean ratio is $\overline{r}_{J_{SC},\,I40} = 0.99$.

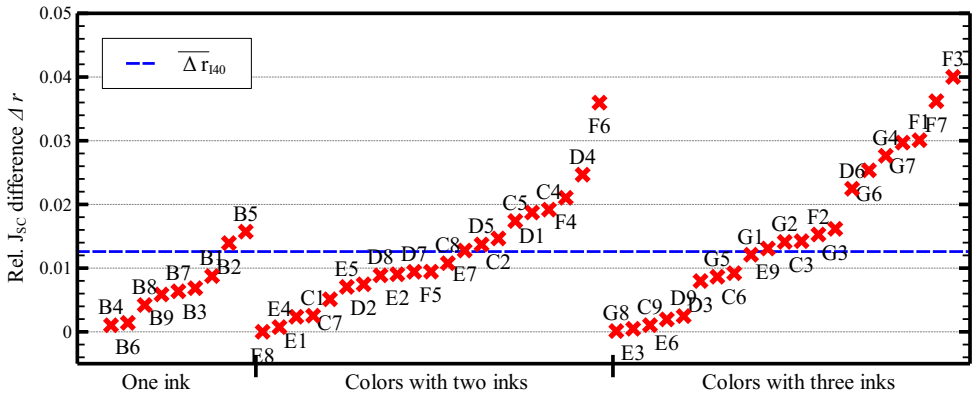

Figure 5.8: Deviations $\Delta r_{J_{SC}}$ of the J_{SC}-ratios r of measured and simulated colors of the I40 samples. The labels of the colors refer to the colors in Figure 5.2. The blue-dashed line shows the average deviation $\overline{\Delta r} = 0.013$.

Figure 5.9 shows the measured and simulated *EQE*s of the single-cell PV module covered with FPLD40 in the colors with the smallest, a moderate and the largest deviation Δr. With $\Delta r_{I40,\,E8} = 0.00001$ and $\Delta r_{I40,\,E7} = 0.013$ the *EQE*s in Fig. 5.9 a) and b) of the colors E8 and E7 lie almost exactly on top of each other. In Fig. 5.9 c) the measured and simulated *EQE* of color F3 are plotted. There, a larger deviation of up to 0.12 can be observed in the wavelength range from 470 nm to 610 nm. The resulting discrepancy of the calculated J_{SC}s is $\Delta r_{F3} = 0.04$.

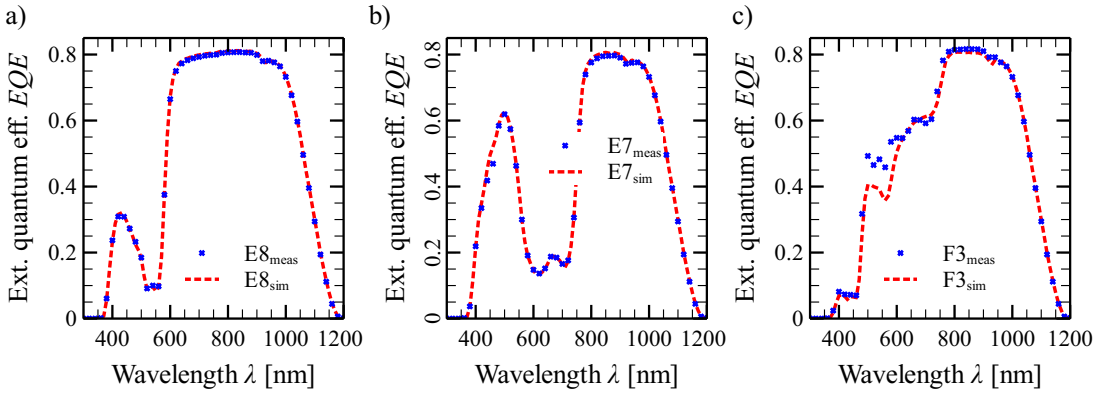

Figure 5.9: Measured and simulated *EQE*s of three different I40 samples, including a) the best, b) a moderate and c) the worst congruence between simulation and measurement.

Figure 5.10 a) shows the 125 simulated colors with their corresponding relative J_{SC} that are feasible for CoTex modules using an inkjet-printed FPLD40. With $J_{SC,rel.} = 0.48$, the color black, where all three inks are printed with 100% print coverage, has the lowest J_{SC}. The highest relative J_{SC} with $J_{SC,rel.} = 0.92$ is reached with a blank FPLD40, resulting in a grayish color impression. In Figure 5.10 b), the 15 simulated colors that have the highest $J_{SC,rel.}$ are shown enlarged.

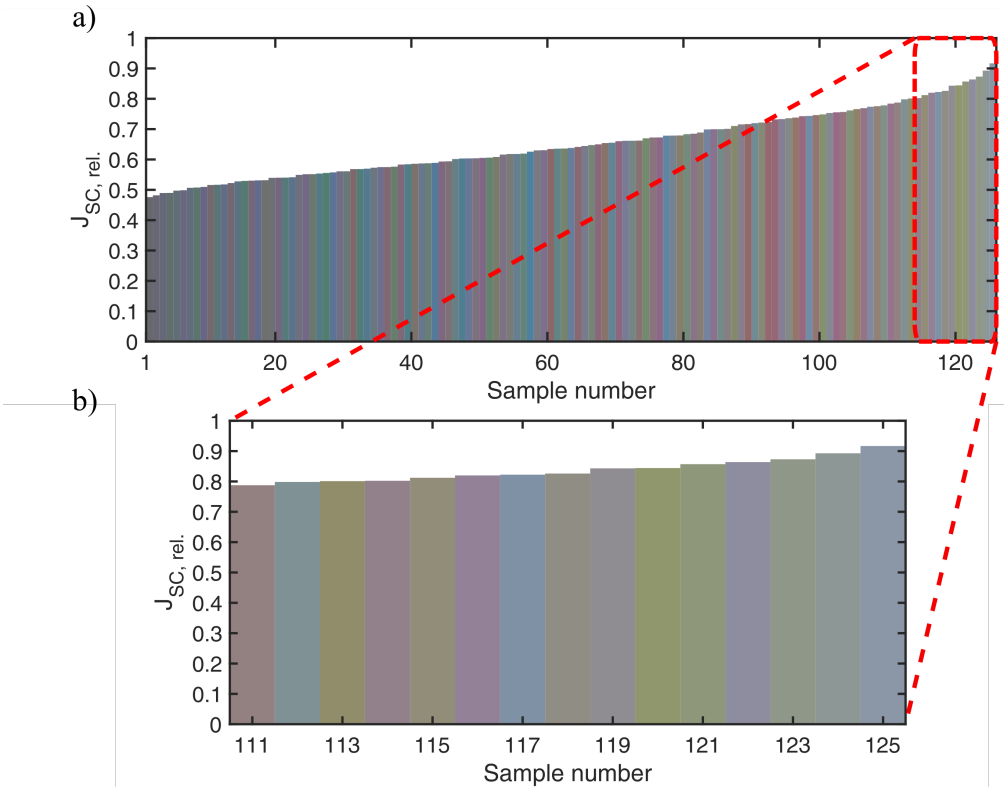

Figure 5.10: a) 125 simulated colors of the inkjet-printed FPLD40 with the respective $J_{SC,\ CoTex\ color}$ relative to the $J_{SC,\ reference}$ of the single-cell module without a CoTex layer. b) Enlarged view of the 15 colors with the highest $J_{SC,rel.}$.

5.3.2 Investigation of the samples I50

Figure 5.11 shows the ΔE_{00} between measured and simulated color of the CoTex module with inkjet-printed FPLD50 samples. The mean color difference over all samples is $\overline{\Delta E}_{\mathrm{I50}} = 2.01$. In contrast to the inkjet-printed FPLD40, the largest difference between simulated and measured color is observed for the FPLD50 with $\overline{\Delta E}_{\mathrm{I50},3} = 2.48$ when all three inks are used. When using one ink, a color difference of $\overline{\Delta E}_{\mathrm{I50},1} = 2.13$ is achieved on average and $\overline{\Delta E}_{\mathrm{I50},2} = 1.51$ with two inks. With $\sigma_{\mathrm{I50},3} = 1.35$, the standard deviation is significantly higher when using three inks than when using only one ($\sigma_{\mathrm{I50},1} = 0.7$) or two inks ($\sigma_{\mathrm{I50},2} = 0.68$).

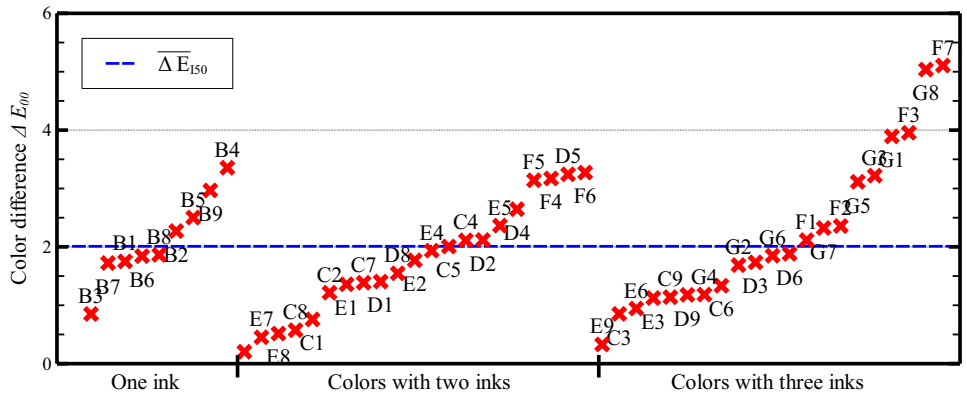

Figure 5.11: Color distance ΔE_{00} between measured and simulated colors of the I50 samples. The labels of the colors refer to the colors in Figure 5.2. The blue-dashed line shows the average $\overline{\Delta E}_{\mathrm{I50}} = 2.01$.

Figure 5.12 shows the measured (blue crosses) and simulated (dotted red line) reflectance spectra of the colors with a) the lowest, b) a moderate and c) the highest ΔE_{00}. In Fig. 5.12 a) there is a close accordance between measured and simulated reflectance spectrum of color D7 with $\Delta E_{\mathrm{I50,\,D7}} = 0.2$ and no difference between the colors resulting from the reflectance spectra is perceptible. In Figure 5.12 b), with $\Delta E_{\mathrm{I50,\,C5}} = 2.01$, the two reflectance spectra deviate by up to 0.015 in the wavelength range from 500 nm to 600 nm. However, no difference can be perceived between measured and simulated color. Figure 5.12 c) shows the largest difference between measurement and simulation with $\Delta E_{\mathrm{I50,\,F7}} = 5.11$. The simulated reflectance spectrum is up to 0.032 lower than the measured reflectance spectrum. The difference between the two colors is small, but noticeable: the simulated color is more greyish, whereas the measured color has a more greenish appearance.

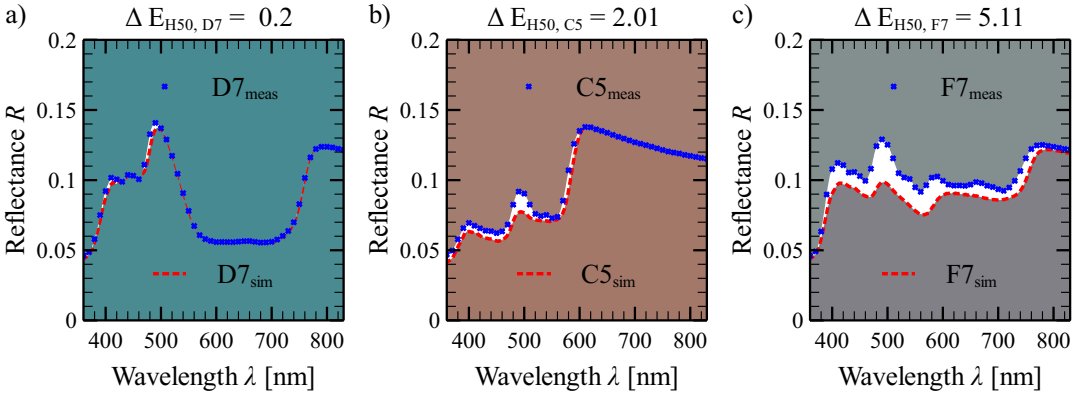

Figure 5.12: Measured and simulated reflectance spectra of samples I50 with the a) lowest, b) a moderate and c) the highest ΔE_{I50}. The background above and below the respective curve is colored in the color determined from the reflectance spectrum. This illustrates the difference between measured and simulated color.

Figure 5.13 shows the deviations of the J_{SC} between measurement and simulation for the inkjet-printed FPLD50 samples. The arithmetic mean of the ratios of all samples is $\overline{r}_{J_{SC},I50} = 0.99$ and the mean deviation is $\overline{\Delta r}_{\mathrm{I50}} = 0.011$ with a standard deviation

of $\sigma_{\mathrm{I50}} = 0.009$. Considering the results in relation to the number of inks used in each individual sample, a steady increase in the deviation with increasing number of inks becomes apparent. For prints with only one ink $\overline{\Delta r}_{\mathrm{I50,\,1}} = 0.007$ with a standard deviation of $\sigma_{\mathrm{I50,\,1}} = 0.005$ is achieved, for two inks $\overline{\Delta r}_{\mathrm{I50,\,2}} = 0.01$ and $\sigma_{\mathrm{I50,\,2}} = 0.008$ and for three inks $\overline{\Delta r}_{\mathrm{I50,\,3}} = 0.014$ and $\sigma_{\mathrm{I50,\,3}} = 0.01$.

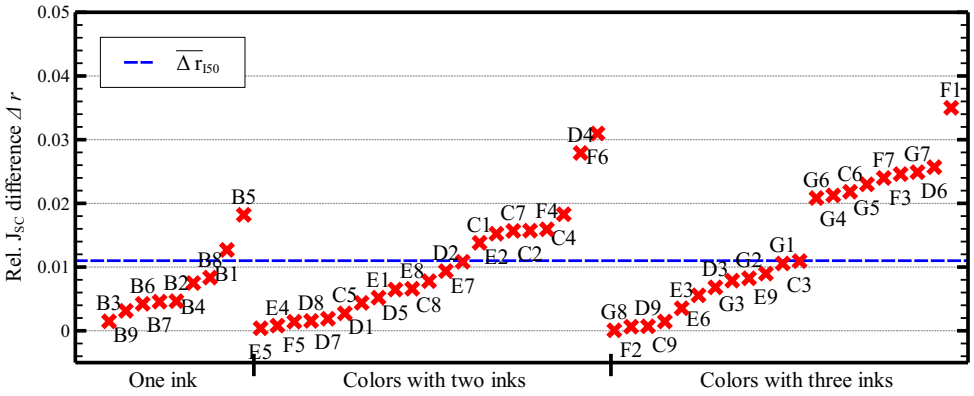

Figure 5.13: Deviations $\Delta r_{J_{\mathrm{SC}}}$ of the J_{SC}-ratios r of measured and simulated colors of the I50 samples. The labels of the colors refer to the colors in Figure 5.2. The blue-dashed line shows the average deviation $\overline{\Delta r}_{\mathrm{I50}} = 0.011$.

Figure 5.14 shows the measured and simulated *EQE*s of the colors with the smallest, a moderate and the largest deviation Δr. For color E5, simulation and measurement of the *EQE* are almost identical, the deviation is $\Delta r_{I50,\,E5} = 0.0004$ (Fig. 5.14 a). Figure 5.14 b) shows the measured and simulated *EQE* of color C3. From 610 nm to 730 nm, the simulated *EQE* is up to 0.04 higher than the measured *EQE*. This difference results in a deviation between the measured and the simulated J_{SC} of $\Delta r_{I50,\,C3} = 0.011$. In Figure 5.14 c) the simulated *EQE* is lower than the measured *EQE* by up to 0.11 at 480 nm. The result is a deviation of $\Delta r_{I50,\,F1} = 0.035$.

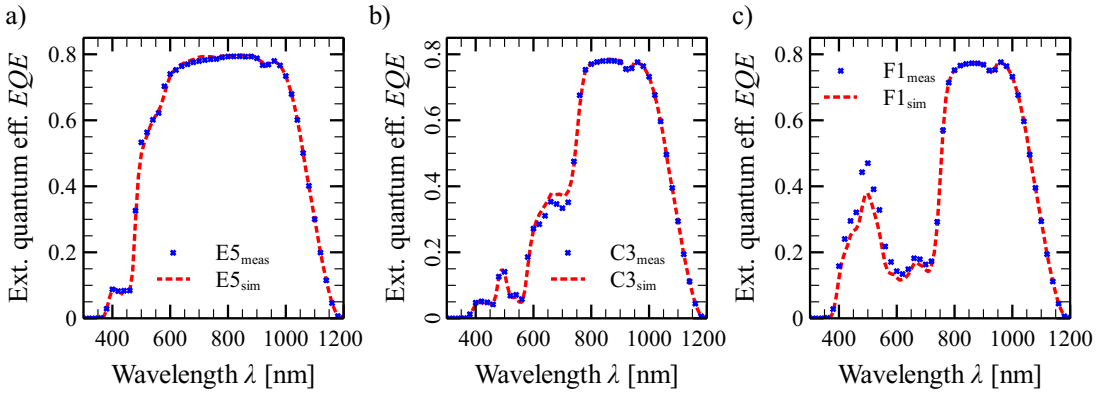

Figure 5.14: Measured and simulated *EQE*s of three different I50 samples, including a) the best, b) a moderate and c) the worst congruence between simulation and measurement.

Figure 5.15 a) shows the color table with 125 colors and the corresponding relative J_{SC} that a CoTex module can adopt when using an inkjet-printed FPLD50. The achievable J_{SC} ranges from a black printed FPLD50 using all three inks with 100%

print coverage with $J_{SC,rel.} = 0.47$ to $J_{SC,rel.} = 0.89$ for the unprinted FPLD50, which gives the CoTex module a grayish appearance. In Figure 5.15 b), the 15 simulated colors that have the highest $J_{SC,rel.}$ are shown enlarged again.

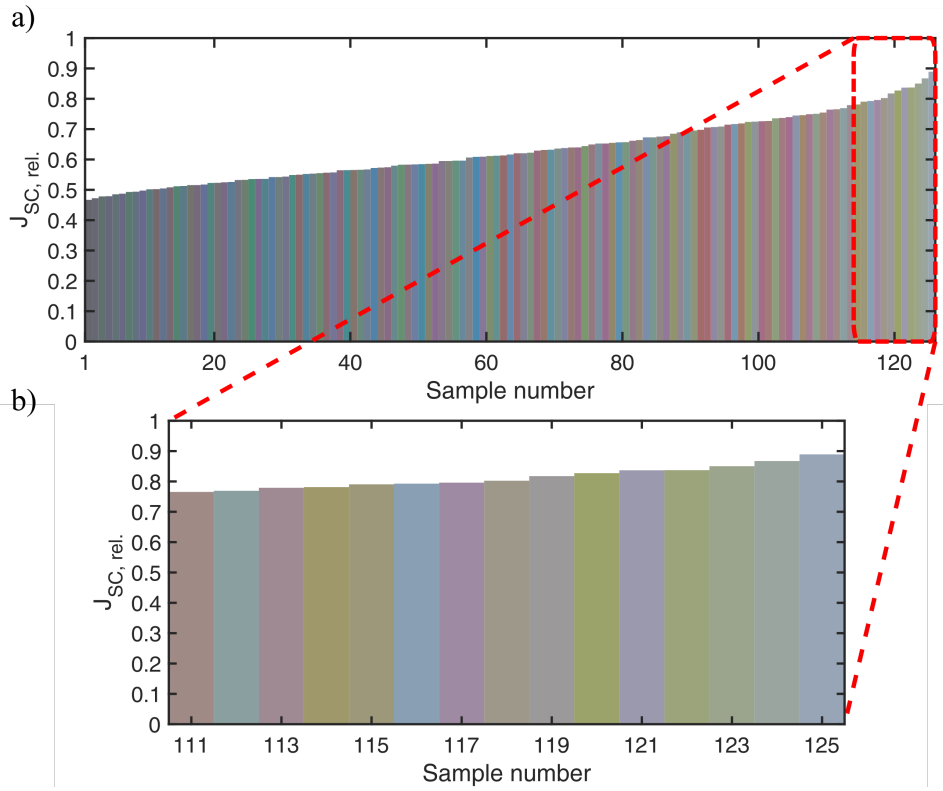

Figure 5.15: a) Simulated colors of the inkjet-printed FPLD50 with the respective $J_{SC,\ CoTex\ color}$ relative to the $J_{SC,\ reference}$ of the single-cell module without a CoTex layer. b) Enlarged view of the 15 colors with the highest $J_{SC,rel.}$.

5.3.3 Investigation of the samples O50

Figure 5.16 shows the accuracy of the simulation of the appearance for CoTex modules using a offset-printed FPLD50. The arithmetic mean of the color difference between simulated and measured color is $\overline{\Delta E}_{\mathrm{O50}} = 1.34$ with a standard deviation of $\sigma_{\mathrm{O50}} = 0.54$. The simulation of colors using three inks with $\overline{\Delta E}_{\mathrm{O50,3}} = 1.58$ is significantly worse than using only one ($\overline{\Delta E}_{\mathrm{O50,1}} = 1.21$) or two inks ($\overline{\Delta E}_{\mathrm{O50,2}} = 1.22$). The number of inks used does not have a great impact on the standard deviation. The standard deviation when using one ink is $\sigma_{\mathrm{O50,1}} = 0.47$, in case of two inks $\sigma_{\mathrm{O50,2}} = 0.45$ and in case of three inks $\sigma_{\mathrm{O50,3}} = 0.6$.

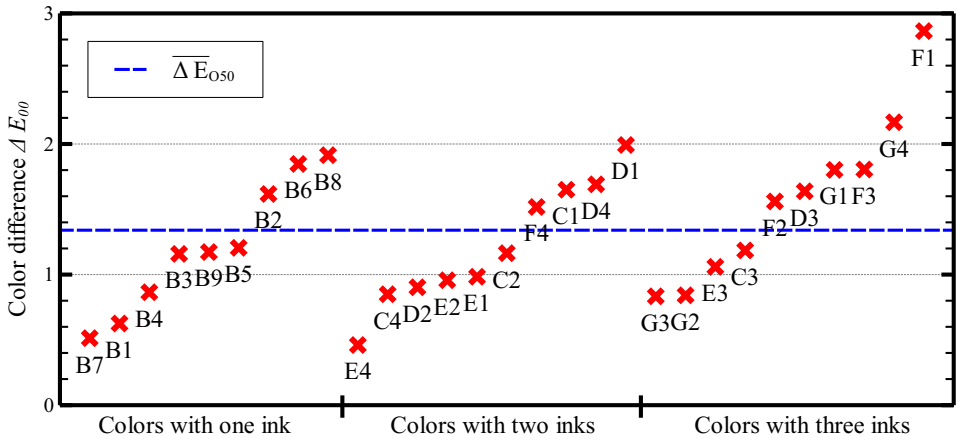

Figure 5.16: Color distance ΔE_{00} between measured and simulated colors of the offset-printed FPLD50. The labels of the colors refer to the colors in Figure 5.2. The blue-dashed line shows the average $\overline{\Delta E}_{O50} = 1.34$.

Figure 5.17 shows the measured (blue crosses) and simulated (dotted red line) reflectance spectra of the colors with a) the lowest, b) a moderate and c) the highest ΔE_{00}. In Figure 5.17 a) with $\Delta E_{O50,\,E4} = 0.46$, the reflectance spectra of the color E4 (C: 1, M: 0.25, Y: 0) lie exactly on top of each other and no difference between the two colors is perceptible. In Figure 5.17 b), with $\Delta E_{O50,\,B5} = 1.21$, the two reflectance spectra deviate by up to 0.007 in the wavelength range from 500 nm to 600 nm. However, no difference can be perceived between measured and simulated color. Figure 5.17 c) shows the largest difference between measurement and simulation with $\Delta E_{O50,\,F1} = 2.86$. The simulated reflectance spectrum in the range between 400 nm and 500 nm is up to 0.016 higher than the measured reflectance spectrum. Despite the differences in the reflectance spectra, the perceivable color difference is very small. The simulated color appears slightly brighter than the measured one.

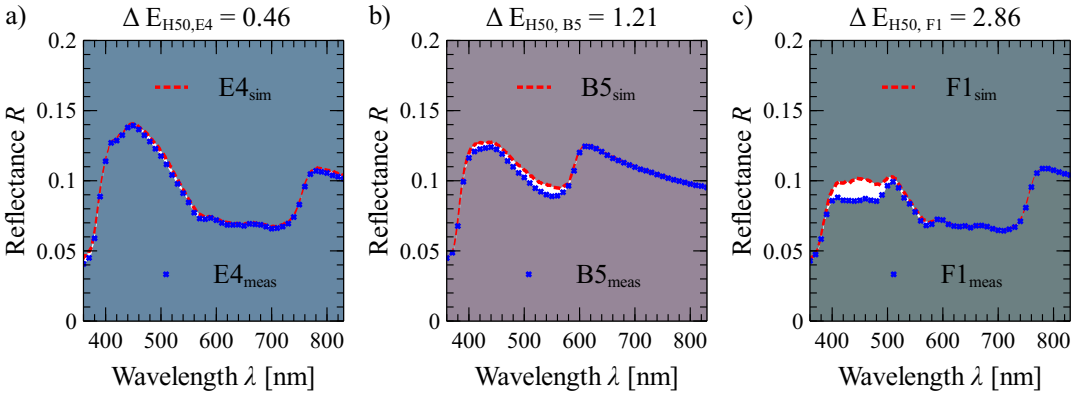

Figure 5.17: Measured and simulated reflectance spectra of samples O50 with the a) lowest, b) a moderate and c) the highest ΔE_{O50}. The background above and below the respective curve is colored in the color determined from the reflectance spectrum. This illustrates the difference between measured and simulated color.

Figure 5.18 shows the deviations between measured and simulated J_{SC} of the offset-printed FPLD50 samples. Except for two outliers F4 and G4, the deviation is below

0.02 for all samples, the arithmetic mean is $\overline{\Delta r}_{\mathrm{O50}} = 0.008$ with the standard deviation $\sigma_{\mathrm{O50}} = 0.0085$. When only one ink is used, the mean deviation is $\overline{\Delta r}_{\mathrm{O50,1}} = 0.006$ with $\sigma_{\mathrm{O50,1}} = 0.0043$. This increases significantly when using two inks to $\overline{\Delta r}_{\mathrm{O50,2}} = 0.0095$ with $\sigma_{\mathrm{O50,2}} = 0.0087$ and to $\overline{\Delta r}_{\mathrm{O50,3}} = 0.0087$ with $\sigma_{\mathrm{O50,3}} = 0.0106$ for colors created by using three inks.

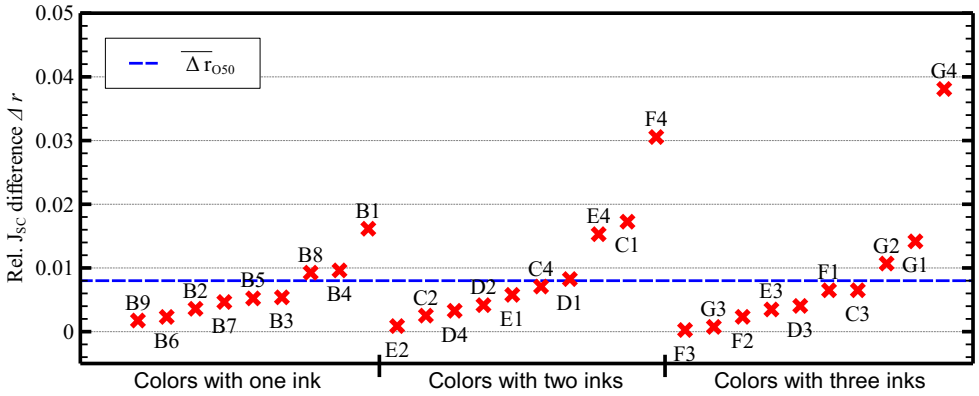

Figure 5.18: Deviation Δr of the J_{SC}-ratios r of measured and simulated colors of the O50 samples. The labels of the colors refer to the colors in Figure 5.2. The blue-dashed line shows the average $\overline{\Delta r}_{\mathrm{O50}} = 0.008$.

In Figure 5.19, differences in certain wavelength ranges become apparent when comparing measured (blue crosses) and simulated (dotted red line) *EQE*s. Figure 5.19 a) shows the *EQE* of sample F3 (C: 0.5, M: 0.5, Y: 1), the color with the smallest deviation between measurement and simulation. Both curves are almost identical, the maximum deviation is 0.03. With $\Delta r_{O50,\,D1} = 0.008$ the deviation of the sample C5 (C: 0.5, M: 1, Y: 0) in Fig. 5.19 b) is on average. Here the simulated *EQE* in the range between 400 nm and 600 nm is lower than the measured *EQE* with a maximum deviation of 0.032 and higher in the range of 600 nm to 800 nm by up to 0.015. Fig. 5.19 c) shows the *EQE* of sample G4 (C: 0.25, M: 0.75, Y: 0.75), with $\Delta r_{O50,\,G4} = 0.009$ the highest deviation between simulation and measurement. The simulated *EQE* is overestimated by up to 0.08 in the range between 400 nm and 750 nm. Remarkably, the inks have an influence on the visible wavelength range only. From 780 nm to 1200 nm the *EQE* is identical for all colors.

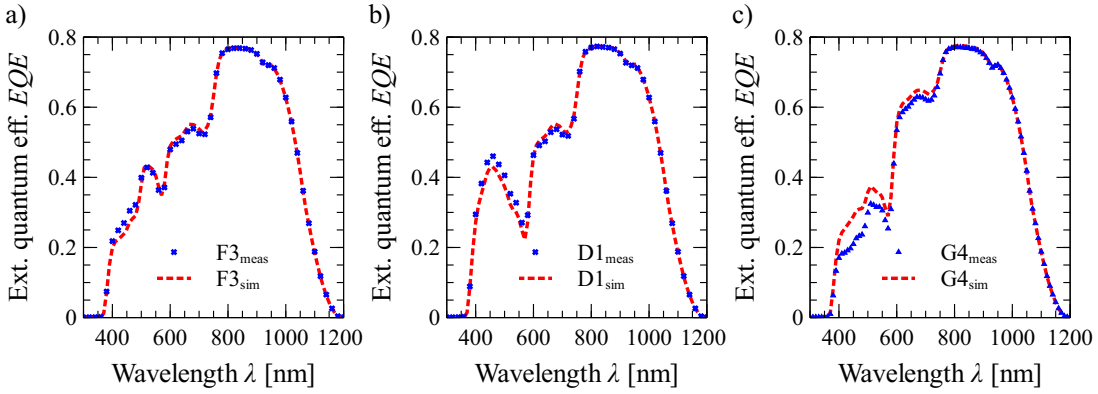

Figure 5.19: Measured and simulated *EQE*s of three different O50 samples, including a) the best, b) a moderate and c) the worst congruence between simulation and measurement.

Figure 5.20 shows 125 simulated colors with the respective J_{SC} that CoTex modules can achieve, when using an FPLD50 imprinted using an offset printing system. The achievable relative J_{SC} range from 0.6 for a black printed FPLD50 to 0.89 for a blank FPLD50. In Figure 5.20 b), the 15 simulated colors that have the highest $J_{SC,rel.}$ are shown enlarged again.

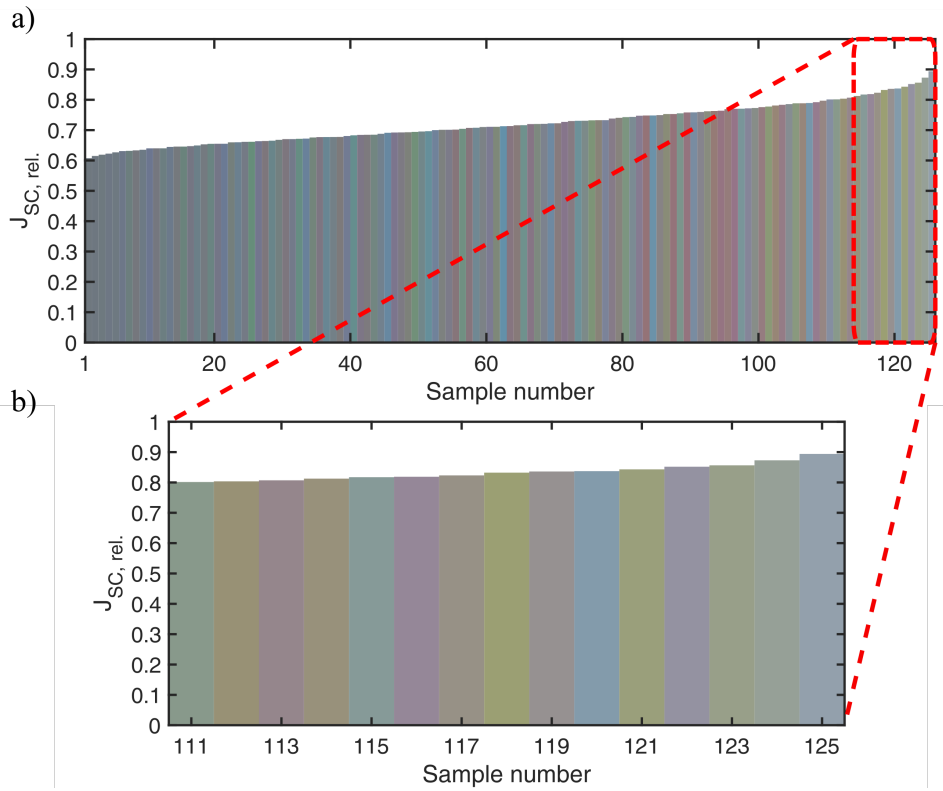

Figure 5.20: a) 125 simulated colors using an offset-printed FPLD50 with the respective $J_{SC,\ CoTex\ color}$ relative to the $J_{SC,\ reference}$ of the single-cell module without a CoTex layer. b) Enlarged view of the 15 colors with the highest $J_{SC,rel.}$.

5.3.4 Investigation of the samples CF

Figure 5.21 shows the accuracy of the simulation of the appearance for PV modules, that are covered with a colored, semitransparent foil. The arithmetic mean of the color difference between simulated and measured color is $\overline{\Delta E}_{\mathrm{CF}} = 1.22$ with a standard deviation of $\sigma_{\mathrm{CF}} = 0.53$. The smallest color differences between measured and simulated color are achieved with $\overline{\Delta E}_{\mathrm{CF},2} = 1.01$ when using two inks. Followed by colors with only one ink ($\overline{\Delta E}_{\mathrm{CF},1} = 1.3$) and with three inks ($\overline{\Delta E}_{\mathrm{CF},3} = 1.41$). The standard deviation increases with the number of inks from $\sigma_{\mathrm{CF},1} = 0.37$ with one ink, $\sigma_{\mathrm{CF},2} = 0.47$ with two and $\sigma_{\mathrm{CF},3} = 0.56$ with three inks.

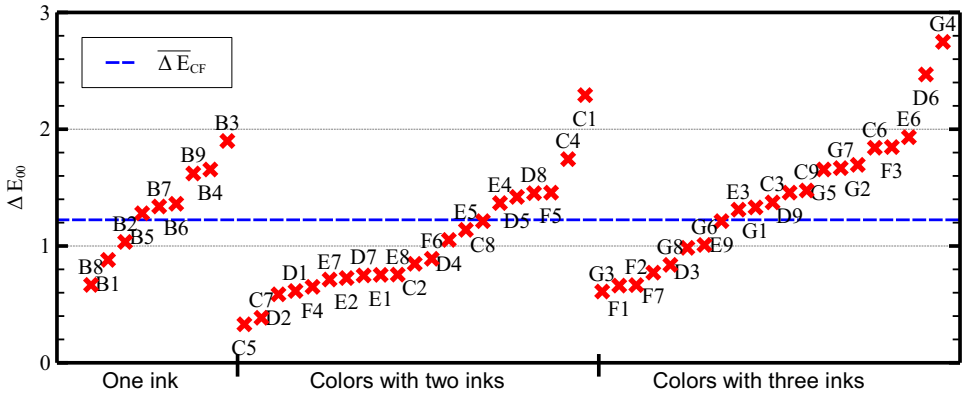

Figure 5.21: Color distance ΔE_{00} between measured and simulated colors of the semitransparent foil. The labels of the colors refer to the colors in Figure 5.2. The blue-dashed line shows the average $\overline{\Delta E}_{\mathrm{CF}} = 1.22$.

In Figure 5.22 a) with $\Delta E_{\mathrm{CF,\,C5}} = 0.33$, the simulated reflectance spectrum of the color C5 (C: 0, M: 0.75, Y: 1) is just below the measured reflectance spectrum in the entire wavelength range with a maximum difference of 0.003. In Figure 5.22 b) with $\Delta E_{\mathrm{CF,\,E9}} = 1.21$, the measured and simulated reflectance spectra of sample E9 are almost identical. Only from a wavelength of approx. 600 nm is the simulated reflectance higher than the measured one, the difference is maximum at $\lambda = 818$ nm with 0.007. Figure 5.22 c) shows the reflectance spectra of sample G4, where we calculate a color difference of $\Delta E_{\mathrm{CF,\,G4}} = 2.75$. The simulated reflectance exceeds the measured one in the range from 360 nm to 607 nm by up to 0.006. In none of the three cases in Figure 5.22 can colors, that are determined from the simulated and measured reflectance spectra, be distinguished by an observer. With a maximum reflectance of 0.08, the reflectance of the PV modules covered with a colored foil is significantly lower than that of the printed FPLD. There, a reflectance of up to 0.15 is achieved.

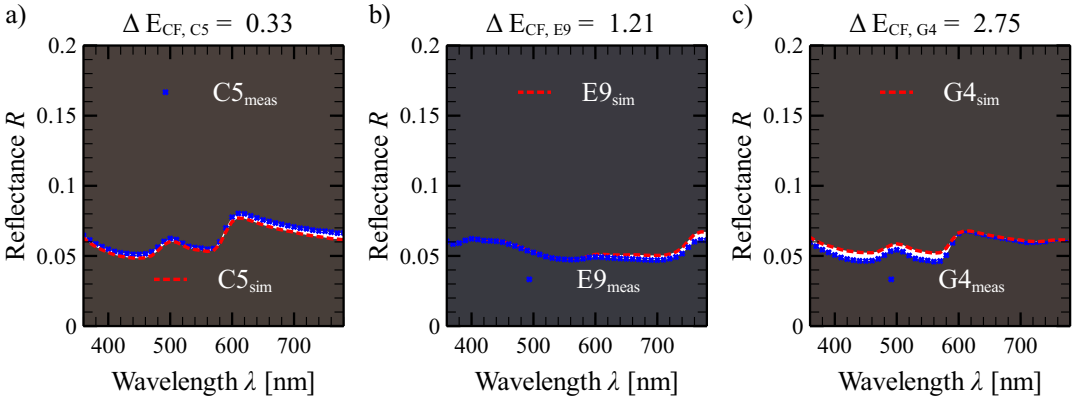

Figure 5.22: Measured and simulated reflectance spectra of samples O50 with the a) lowest, b) a moderate and c) the highest ΔE_{CF}. The background above and below the respective curve is colored in the color determined from the reflectance spectrum. This illustrates the difference between measured and simulated color.

Figure 5.23 shows the deviations between measured and simulated J_{SC} of the imprinted foil. Over all samples, the average deviation is $\overline{\Delta r}_{\mathrm{CF}} = 0.019$ with a standard deviation of $\sigma_{\mathrm{CF}} = 0.011$. With a $\overline{\Delta r}_{\mathrm{CF}} = 0.021$, the mean deviation is highest for colors using two inks, as is the standard deviation $\sigma_{\mathrm{CF},2} = 0.013$. For colors using three inks, $\overline{\Delta r}_{\mathrm{CF},3} = 0.019$ is obtained with $\sigma_{\mathrm{CF},3} = 0.011$. Significantly better is the simulation of J_{SC} when using only one ink, where $\overline{\Delta r}_{\mathrm{CF},1} = 0.013$ and $\sigma_{\mathrm{CF},1} = 0.007$.

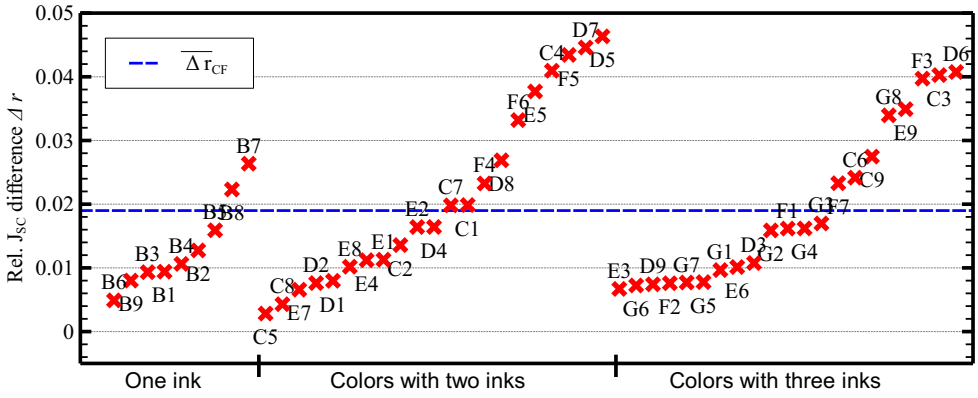

Figure 5.23: Deviation Δr of the J_{SC}-ratios r of measured and simulated colors of the colored foil samples. The labels of the colors refer to the colors in Figure 5.2. The blue-dashed line shows the average $\overline{\Delta r}_{\mathrm{CF}} = 0.019$.

Figure 5.24 shows the measured (blue crosses) and simulated (dotted red line) *EQE*s with the a) lowest, b) a moderate and c) the highest Δr_{CF}. In Figure 5.24 a) for sample C5 the two *EQE*s agree in large parts. Only in the range between 500 nm and 600 nm the simulated *EQE* is higher than the measured *EQE* by up to 0.07 and in the range between 610 nm and 780 nm it is lower than the measured *EQE* by up to 0.025. This results in $\Delta r_{\mathrm{CF,C5}} = 0.003$. In Figure 5.24 b) for sample C7, the simulation underestimates the *EQE* by up to 0.04 in the region between 500 nm and 750 nm, resulting in $\Delta r_{\mathrm{CF,C7}} = 0.02$. In the worst match with $\Delta r_{\mathrm{CF,D5}} = 0.046$, the measured *EQE* of sample D5 is higher than the simulated *EQE* by up to 0.12 in the range between

350 nm and 800 nm.

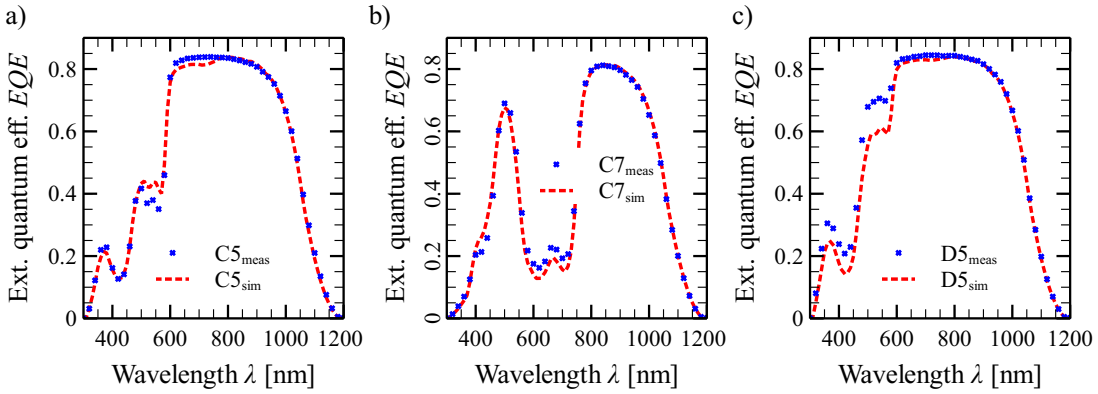

Figure 5.24: Measured and simulated *EQE*s of three different CF samples, including a) the best, b) a moderate and c) the worst congruence between simulation and measurement.

Figure 5.25 a) shows 125 simulated colors with the corresponding relative J_{SC} that PV modules achieve when they are covered with a printed foil in the respective colors. The relative J_{SC} varies depending on the color between 0.49 when all three inks are printed with 100% coverage and 0.98 when only the yellow ink is printed with 25% coverage. In Figure 5.25 b), the 15 simulated colors that have the highest $J_{SC,rel.}$ are shown enlarged again.

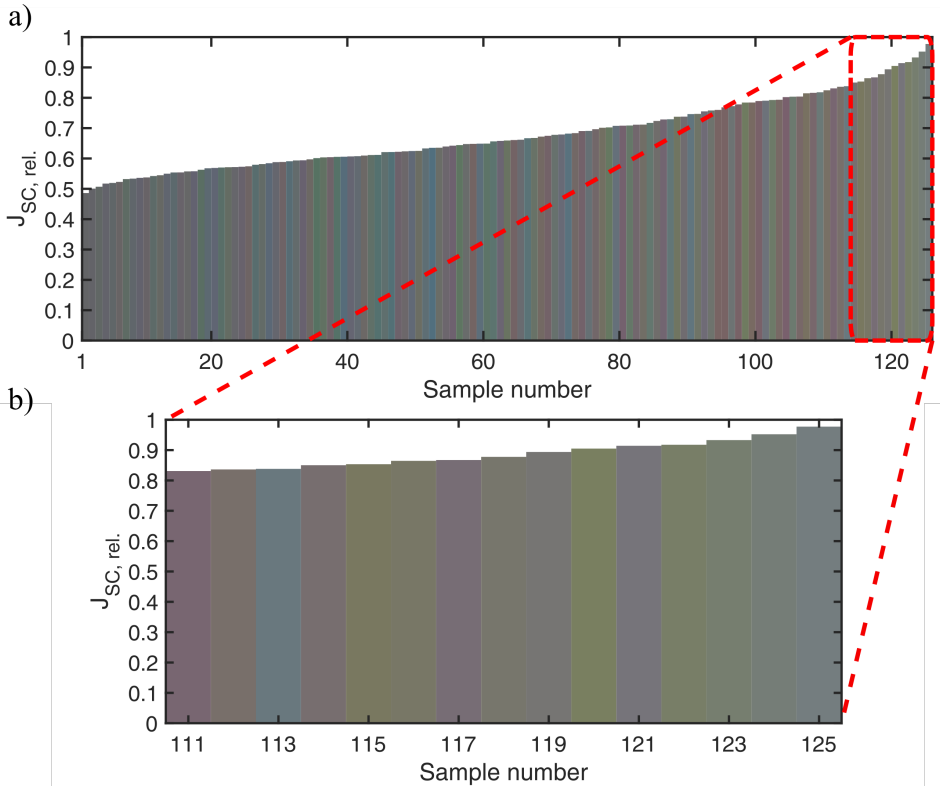

Figure 5.25: a) 125 simulated colors using a printed foil with the respective $J_{\mathrm{SC,\,rel.}}$ relative to the $J_{SC,\,reference}$ of the single-cell module without a colored layer. b) Enlarged view of the 15 colors with the highest $J_{SC,rel.}$.

5.4 Ink spreading correction

The planned print coverage of an ink can deviate from the effective print coverage after printing. This happens due to the spreading of the ink blob and is not only dependent on the printer, but especially also on the substrate. It therefore makes a difference whether an ink is printed on an unprinted surface or on an already fully printed surface. This dot gain affects the appearance of the print. To be able to print the desired color anyway, the planned print parameters must be corrected by ink spreading functions. To determine the ink spreading functions, each of the three basic inks is applied in 25%, 50% and 75% print coverage to an unprinted surface, to a surface covered with 100% print coverage of one of the other two inks and to a sample printed with both other inks at 100% print coverage each. Figure 5.26 shows the effective print coverage a_i' and the ink spreading functions of the respective ink determined by comparing simulation and measurement of the I50 samples. The lower right corner shows which color (filled circle) was printed on which background (filled square) in each case. For example, in case g) cyan was printed on a FPLD50, which was printed with yellow at 100% print coverage. In case j) cyan was printed on a red surface, accordingly the sample was printed with 100% magenta and 100% yellow. By using an ink spreading correction function f_{a_i',a_j,a_l}, the desired print result can be achieved more accurately.

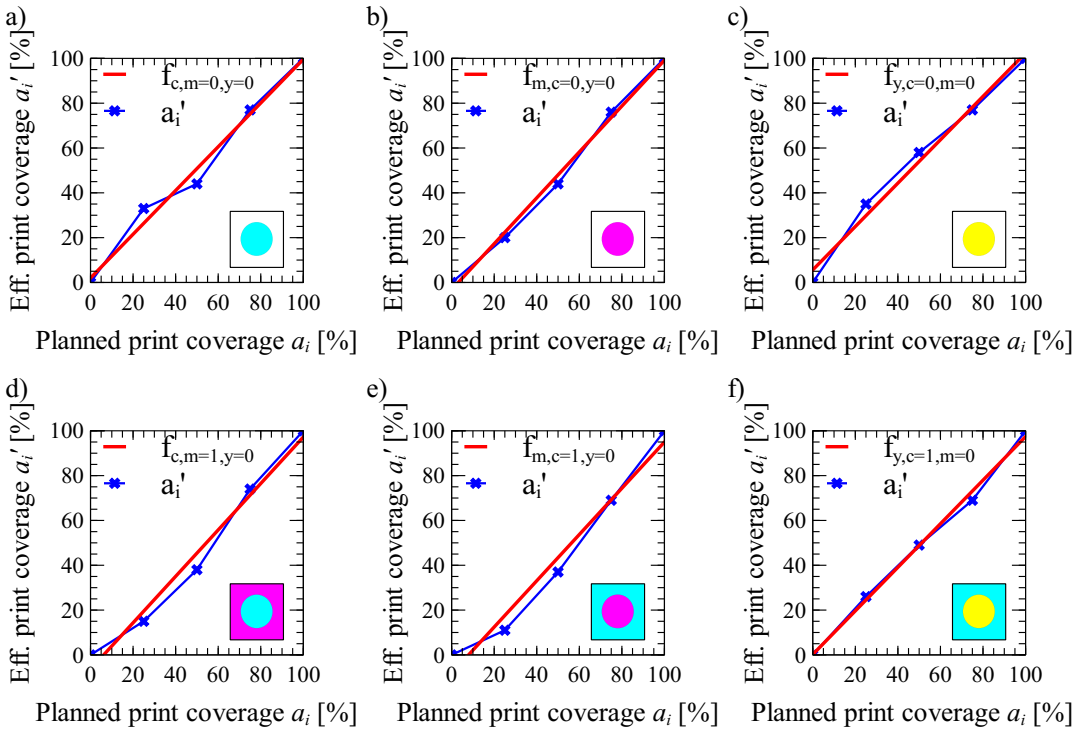

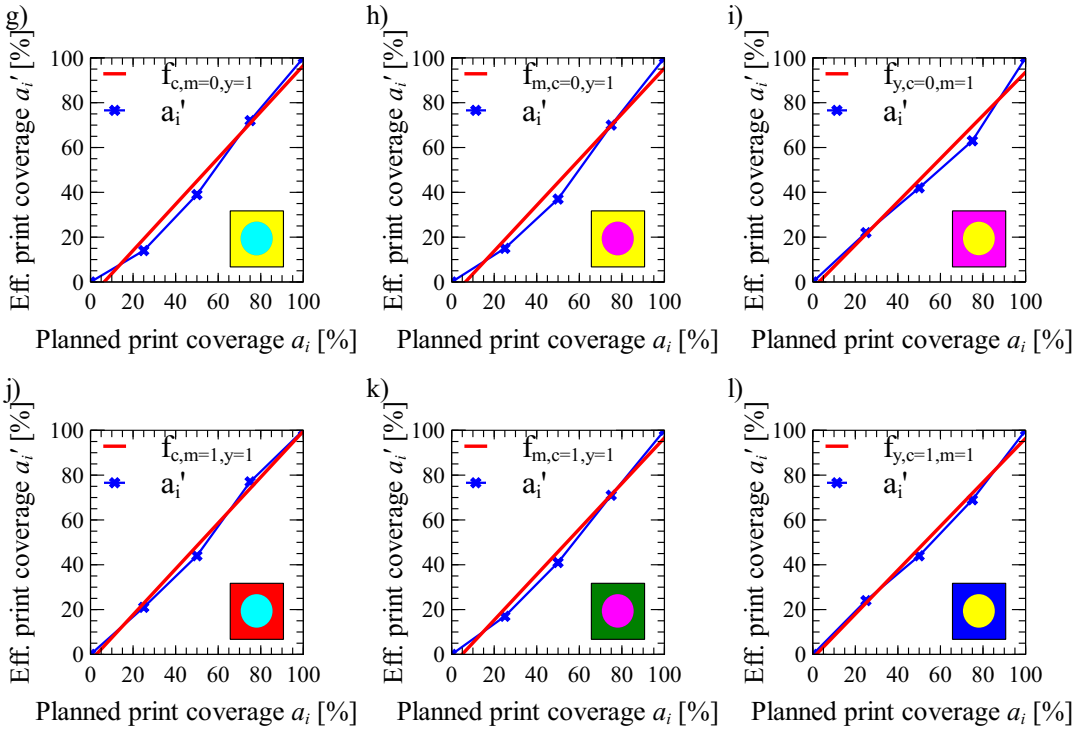

Figure 5.26: Shown are the effective print coverages a_i' and the resulting ink spreading functions f_{a_i',a_j,a_l} for the cases a) cyan, b) magenta and c) yellow on unprinted background, d) cyan on colorant magenta, e) magenta on the colorant cyan, f) yellow on colorant cyan, g) cyan on colorant yellow, h) magenta on colorant yellow, i) yellow on colorant magenta, j) cyan on colorant magenta and yellow, k) magenta on colorant cyan and yellow, and l) yellow on colorant cyan and magenta. The lower right corner shows which color (filled circle) was printed on which background (filled square) in each case.

Figure 5.27 shows the color distances ΔE_{00} between the colors determined from measured and simulated reflectance spectra, with (green diamonds) and without (red crosses) ink spreading correction. The ink spreading correction significantly reduces the color distances for most samples. Only for samples C1, C8 and D8 the color distance with the correction is 0.49, 0.45 and 0.28 higher, respectively, than without the correction.

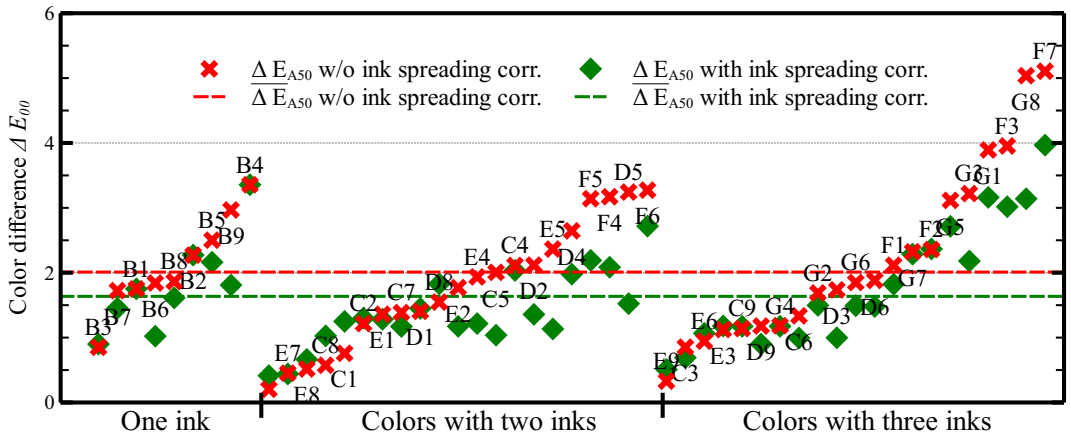

Figure 5.27: Color distance ΔE_{00} between measured and simulated colors of the I50 samples with and without ink spreading correction. The labels of the colors refer to the colors in Figure 5.2. The average ΔE_{00} without ink spreading correction is 2.01 (red dashed line) and with the correction 1.64 (green dashed line).

Using the ink spreading correction increases the accuracy of the simulation of the appearance of CoTex modules using inkjet-printed FPLD50 on average by 0.38 to $\overline{\Delta E}_{\mathrm{I50}} = 1.64$. To calibrate the simulation of the digital prototype only eight different colored samples have to be measured. If the ink spreading correction is to be applied, the reflectance spectrum of additional 36 different samples (rows A to E in Fig. 5.2) must be measured. Especially if a material and a printing process has already been proven for use in CoTex modules, the additional measurement effort is worthwhile in order to be able to make a more accurate prediction of the appearance of arbitrary colored CoTex modules.

5.5 Consequences of printing inaccuracies

I have simulated all combinations of cyan, magenta and yellow with print coverage in 10% steps from 0% to 100%, resulting in 1331 different colors. For each of these colors, 26 print accuracy variations were simulated. The variations consist of all possible combinations of the (0.97, 1, 1.03) triple for each of the three primary colors cyan, magenta and yellow. That means, I assess the impact if the respective ink is being printed with 97%, 100% or 103% of the planned print coverage.

Figure 5.28 a) shows the ΔE_{00} of all 26 variations in comparison to the planned color. For all printing accuracy variations and colors, ΔE_{00} is less than 1, the mean value is less than 0.5 for all variations. The highest mean value of $\Delta E_{00} = 0.47$ occurs in variation 20 with the triple (1.03 0.97 1.03). This means that cyan is printed with 103%, magenta with 97% and yellow with 103% of the planned print coverage. With ΔE_{00} values below 1, the difference between the requested and the printed color is not perceptible, even in the worst case. Printer inaccuracies of up to 3% can therefore be neglected. [35]

Figure 5.28 b) shows the ratio between the J_{SC} of the 26 variations and the J_{SC} of the

planned color. The mean value of the deviation is 0.006 in the worst case, the mean deviation over all colors and variations is only 0.003. Thus, the difference that can occur due to inaccuracies in the printing process is marginal. [35]

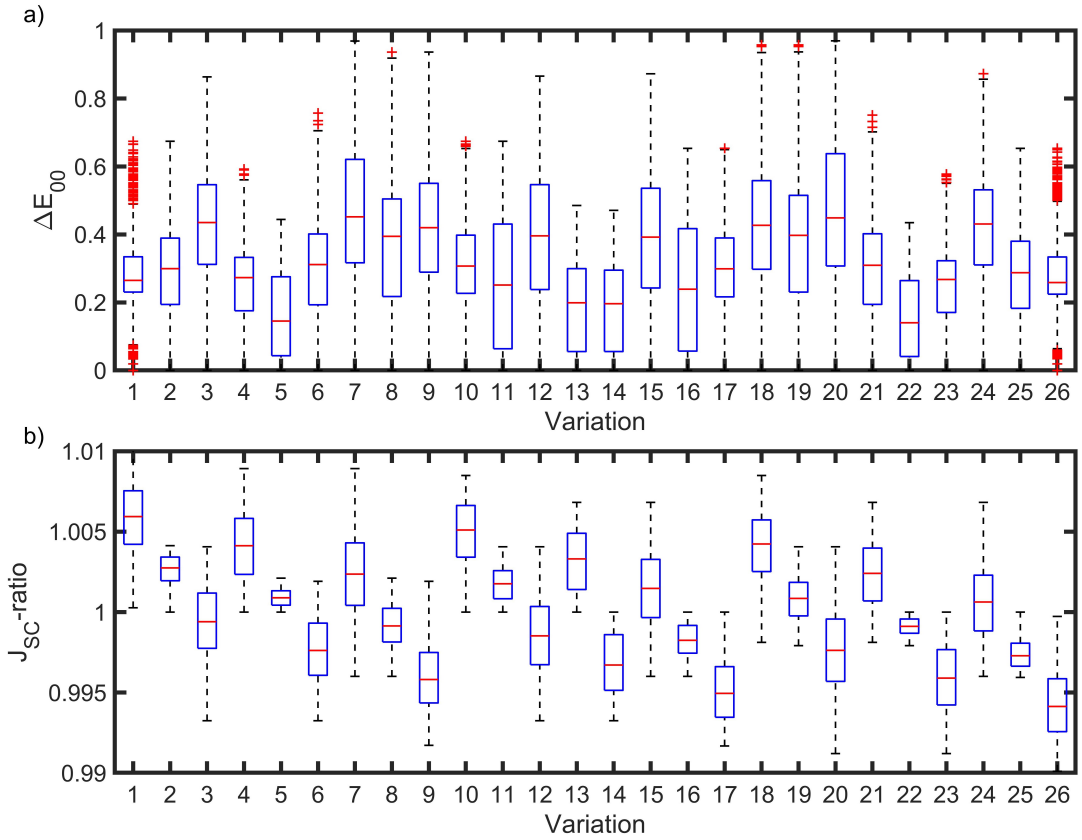

Figure 5.28: a) ΔE_{00} and b) J_{SC} ratio of 26 potential deviations with a printing inaccuracy per ink of maximum 3% compared to the print with the exact printing parameters. [35]

5.6 Conclusion of Chapter 5

Accuracy of the simulation of a digital prototype The simulations for creating a digital prototype were carried out for four sample types. These included, firstly, different material thicknesses with the same printing technique (inkjet-printed FPLD40 and FPLD50), the same material but with different printing techniques (FPLD50 printed using an inkjet and an offset printer) and two different coloring techniques (CoTex and the printed foil). To determine the accuracy of the simulation, 51 different colored samples were produced for all sample types, only for the offset-printed FPLD50 there were only 29 different colored samples.

Figure 5.29 shows the accuracy of the simulation of appearance (a) and J_{SC} (b). The best results are obtained with the offset-printed FPLD50. The reason for this can be found in the microscope images (Fig. 5.4): With the offset printing, the halftone pattern is most clearly and neatly visible as a single layer on the fabric. This is most consistent with the assumptions underlying the Clapper-Yule model used for the sim-

ulations. However, the mean color difference $\overline{\Delta E_{00}}$ is less than 2.5 for all four sample types, which corresponds to a barely perceptible color difference between simulation and measurement.

Among the sample types examined, the largest deviation in simulated J_{SC} is observed for the colored foil samples, which are imprinted with two inks. With a mean deviation $\overline{\Delta r}_{CF,2} = 0.021$ and a standard deviation of $\overline{\sigma}_{CF,2} = 0.012$ in the worst case, the accuracy of the simulation of the J_{SC} is also very high.

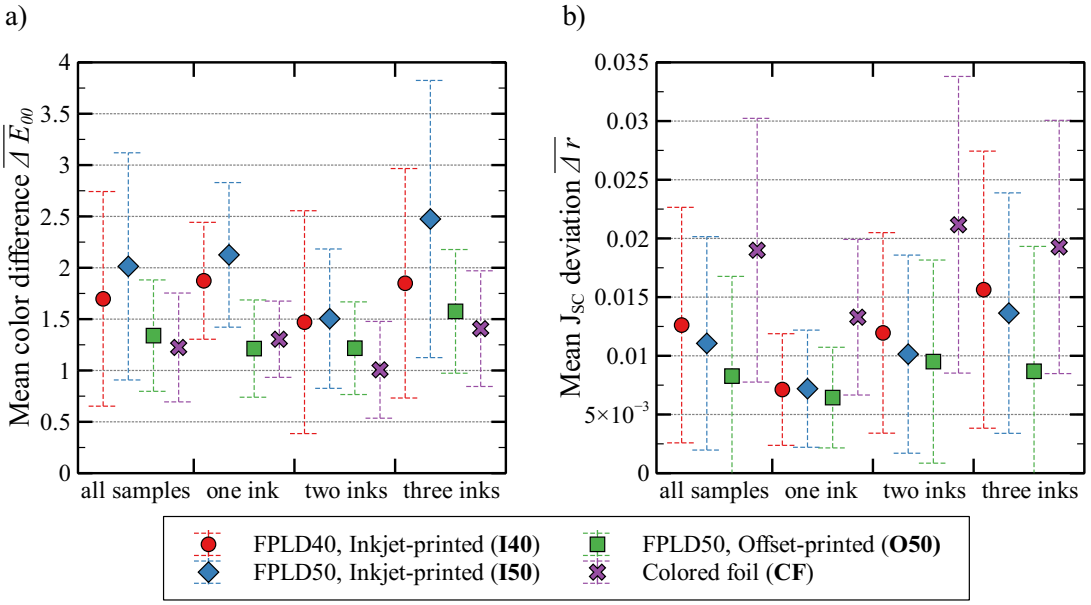

Figure 5.29: Accuracy of simulations of the color (a) and the J_{SC} (b) of the four sample types investigated, divided into all samples and samples where one, two or three inks were used. The error bars indicate the respective standard deviation σ.

Impact of inks, materials and printing technique With CoTex modules, the choice of material, ink and printing technique has a significant impact on the yield and appearance. With denser materials or more opaque inks, the dark blue or black solar cells shine less through the CoTex layer. As a result, more and richer colors are realizable. Figure 5.30 shows the CIE chromaticity diagram and in each case framed in black the gamut that is possible with the combination of material and printing. Figure 5.30 a) and b) show the potential colors of the inkjet-printed FPLD40 and FPLD50. With the FPLD50, a larger range of colors is possible. Figure 5.30 c) shows the color options for the FPLD50 printed using an offset printer. This gamut is significantly smaller than for the inkjet-printed FPLD40 and FPLD50. It therefore implies that the inks used by the offset printer have less opacity than the inks used by the inkjet printer.

Figure 5.30 d) shows the color gamut that can be created when a PV module's appearance is altered by a colored foil. The color gamut is small because the foil used is very transparent. With a less translucent foil, a larger color gamut would be possible, but this would also reduce the energy yield.

Please note, that the colors actually consist of three color coordinates, but in the chro-

maticity diagramm, colors are normalized to the two coordinates x and y (see chapter 2.1.3). Brightness and luminence of the colors are therefore not displayed in this diagram. The realizable colors with the materials investigated here are significantly darker due to the solar cells shining through.

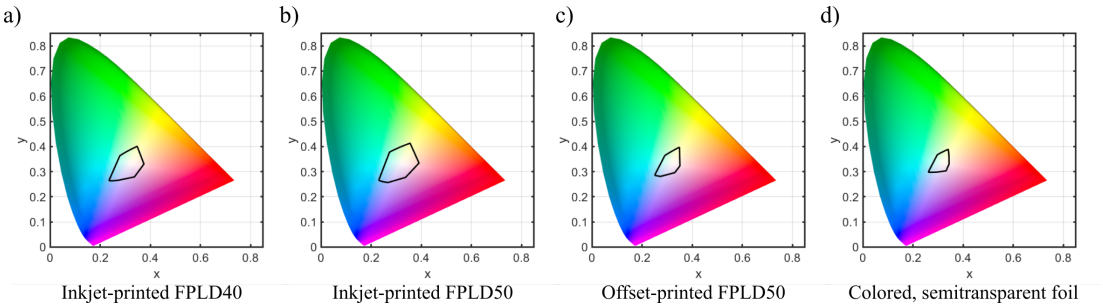

Figure 5.30: CIE chromaticity diagrams. Outlined in black is the color gamut that can be produced with the selection of ink and material in each case.

In order to get a better overview of which colors are possible with which material and which inks, I refer to the RAL 840-HR classic colors (RAL gGmbH, Bonn, Germany). These are standardized colors for the industry. Figure 5.31 illustrates the RAL colors of PV modules that we can produce with CoTex layers of inkjet-printed FPLD40 (a) and FPLD50 (b), offset-printed FPLD50 (c) and PV modules which appearance is altered by a colored foil (d). Most RAL colors can be produced with the inkjet-printed FPLD50, followed by the offset-printed FPLD50. In this overview it is also clear that a comparison between different materials and printing techniques is advisable. For example, the color RAL 7042 appears in Figure 5.31 a), b) and c). With the inkjet-printed FPLD40, RAL 7042 achieves $J_{SC,rel.} = 0.89$ by using only the yellow colored ink with 10% print coverage. Using the inkjet-printed FPLD50, 10% cyan, 30% magenta and 20% yellow are necessary to create an appearance of the color RAL 7042. The resulting short-circuit current density is $J_{SC,rel.} = 0.77$ only. With the offset-printed FPLD50, RAL 7042 with $J_{SC,rel.} = 0.84$ can be created by using 10% magenta and 10% yellow.

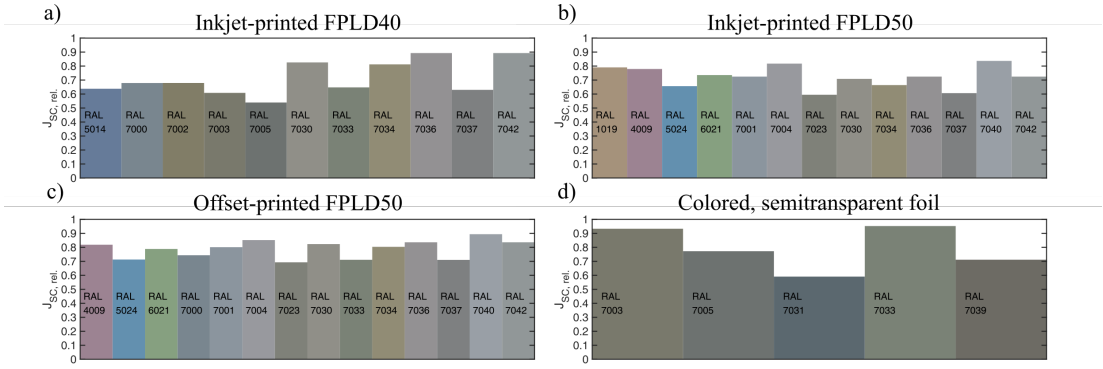

Figure 5.31: Simulated RAL colors and the corresponding short-circuit current densities of modules that can be produced using a) the inkjet-printed FPLD40, b) the inkjet-printed FPLD50, c) the offset-printed FPLD50 [35] or the colored foil.

An objective comparison between these materials can be made by considering the CPI (eq. 3.1) introduced by Røyset *et al.* [75]. The CPI is calculated from the ratio between the relative energy loss r_{power} and the brightness Y. Figure 5.32 shows the relative energy losses and the CPI for the four sample types. It is also evident from this diagram that PV modules in rather muted colors can be produced with the materials studied here. The luminosity of the possible colors ranges from 24 (Fig. 5.32 d) to 42 (Fig. 5.32 b) and the highest CPI of 1.4 is achieved with the inkjet-printed FPLD40. It is noticeable that the relative energy loss decreases with increasing luminosity. In the case of the colored PV modules studied by Røyset *et al.* this curve is exactly reversed (see Fig. 3.6). The reason for this behavior is that the unprinted material has the highest reflectance and at the same time the highest energy yield. By using subtractive color mixing, printing absorbs a part of the incident radiation. As a result, this part of the irradiation can contribute neither to the reflectance, i.e. the luminosity, nor to the energy yield.

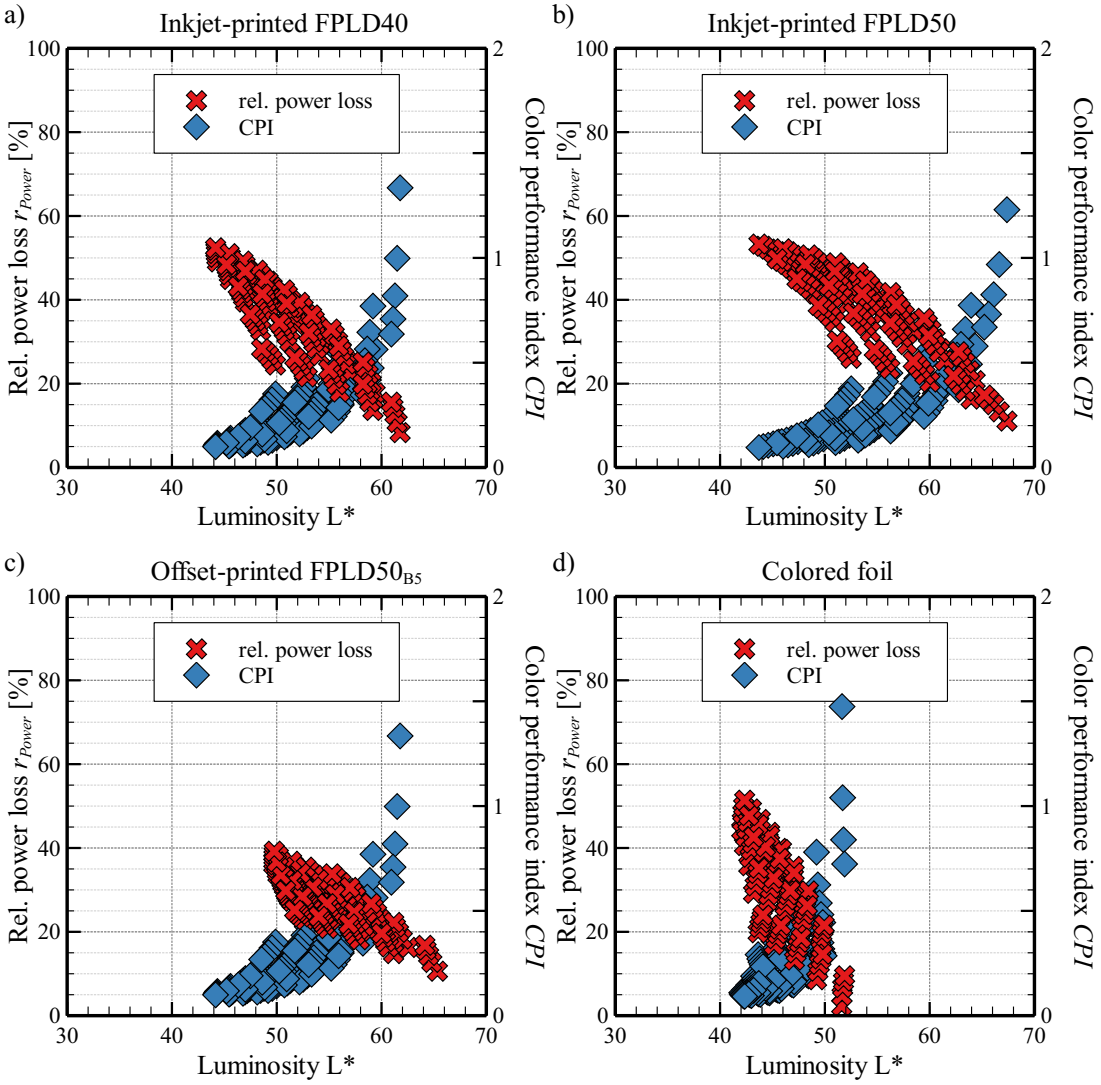

Figure 5.32: Simulated relative power losses (red crosses) and CPI (blue diamond) of the four sample types for 1331 colors.

Chapter 6

Energy yield calculation

The energy yield calculation of building-integrated PV modules is essential for a user to estimate how high his electricity generation costs are and how much of his energy demand he can cover with PV modules. In this chapter I present the energy yield estimation of standard and CoTex modules. Besides the unique feature of the colored layer of the CoTex modules, the focus in this chapter is on the use of a ground view factor (GVF) for a more accurate calculation of the irradiation reflected from the ground. I also compare five different models each for calculating diffuse from global irradiance and for transposing horizontal diffuse irradiance to the vertical plane.
In the first section, the methods used to calculate the energy yield, the procedure of the simulations and the measurement techniques are explained. Afterwards, the accuracy of the calculation of the irradiance in the vertical plane is analyzed by using different models and approaches. In the last section, I present the energy yield prognosis for standard and CoTex PV modules.
I have already published part of the method and results presented here on the ground view factor, as well as on the energy yield prediction of vertically mounted PV modules, in reference [33].

6.1 Methods for the energy yield calculation

I use the MATLAB toolbox PVLIB from the Sandia Laboratories, which provides a set of functions for simulating the performance of photovoltaic energy systems [82]. I use it to estimate the PV yield and to determine the required parameters like the position of the sun, the angle of incidence (AOI), the relative air mass and the extraterrestrial irradiance. Furthermore, I use different models to calculate the diffuse horizontal irradiance (DHI) and the direct normal irradiance (DNI) and to transpose irradiance from the horizontal to the vertical plane. Based on the irradiance in the plane of array (POA) and environmental parameters, I calculate the energy yield of a PV module using the Sandia photovoltaic array perfomance model [54].

6.1.1 Calculation of the diffuse and the direct irradiance fraction

I use measured and calculated DHI values. If I use the DHI measured at ISFH, I determine

$$DNI = \frac{GHI - DHI}{\cos(90° - \theta_{\mathrm{el}})}, \tag{6.1}$$

where θ_{el} represents the elevation angle of the sun. If no measured DHI is used, I calculate the DHI and DNI from the GHI. Several models exist in the literature which determine the ratio of diffuse to global irradiance using the ratio of extraterrestrial irradiance E_{A} to global irradiance. The basic idea of the methodology is, that when GHI is low and extraterrestrial irradiance is high, there must be more clouds and the diffuse irradiation has a larger share of the total irradiation. I apply five different, widely used models: The models of Erbs *et al.* [27], Reindl *et al.* [72], Orgill and Hollands [67], the DISC model [61] and the DIRINT model [47]. In all models, a factor k_{T} is defined, which is composed of GHI, E_{A} and the zenith angle of the sun θ_{Z}:

$$k_T = \frac{GHI}{E_A \cdot \cos\theta_Z} \tag{6.2}$$

In addition to k_{T}, the ratio of DHI to GHI is described in the models via the diffuse fraction k_{D}. Depending on the model, k_{D} is calculated as a function of k_{T} for different degrees of cloudiness. The formulas for k_{D} are empirical; in the model of Reindl *et al.*, for example, they are based on data measured in the USA and Europe. There, k_{D} is defined by:

$$k_D = \begin{cases} 1.02 - 0.248 k_T & \text{, if } k_T \leq 0.3 \text{ (heavy clouds)}, \\ 1.45 - 1.67 k_T & \text{, if } 0.3 < k_T < 0.78 \text{ (light cloudiness)}, \\ 0.147 & \text{, if } k_T \geq 0.78 \text{ (clear sky)}. \end{cases} \tag{6.3}$$

Using k_D, we are able to calculate the DHI with

$$DHI = k_D \cdot GHI. \tag{6.4}$$

6.1.2 Transposition of the diffuse insolation

I consider five different, widely used models for the transposition of the horizontal diffuse irradiance into the vertical POA. I use the isotropic model of Liu & Jordan [57] and the anisotropic models of Reindl *et al.* [73], Klucher *et al.* [52], Perez *et al.* [70, 71] and Hay and Davies [42]. Since I consider façade modules in a vertical plane, I calculate the diffuse vertical irradiance (DVI), thus the angle of inclination of the POA is always $\alpha = 90°$.

The isotropic model of Liu and Jordan calculates

$$DVI_{\mathrm{iso}} = DHI \frac{1 + \cos\alpha}{2}. \tag{6.5}$$

The anisotropic model of Hay and Davies divides the diffuse irradiance in the POA into an isotropic and a circumsolar part:

$$DVI_{\mathrm{H\&D}} = DHI \cdot A \cdot R_b + DHI(1-A)\frac{1+\cos\alpha}{2}, \tag{6.6}$$

where $A = \frac{DNI}{E_A}$ represents the transmittance of the beam through the atmosphere and R_b the ratio between the direct beam irradiance in the POA and the horizontal plane. The model of Klucher *et al.* considers three components: In addition to isotropic irradiance, an increased irradiance from the horizon and circumsolar region is included:

$$DVI_{\mathrm{Klucher}} = DHI\frac{1+\cos\alpha}{2}(1+F\sin^3\frac{\alpha}{2})\cdot(1+F\cos^2\theta\sin^3\theta_Z) \tag{6.7}$$

with a modulating function $F = 1-(\frac{DHI}{GHI})^2$. The model by Reindl *et al.* also takes into account horizontal and circumsolar brightening in addition to isotropic irradiation:

$$DVI_{\mathrm{Reindl}} = DHI\big[(1-A)\frac{1+\cos\alpha}{2}\cdot(1+f\sin^3\frac{\alpha}{2}) + A\cdot R_b\big], \tag{6.8}$$

with the horizontal brightening correction factor $f = \sqrt{\frac{I_{\mathrm{Direct}}}{GHI}}$. In the Perez model, these three components are also included:

$$DVI_{\mathrm{Perez}} = DHI\big[\frac{1}{2}(\cos\alpha)(1-F_1) + F_1\frac{a}{c} + F_2\sin\alpha\big] \tag{6.9}$$

with the solid angles corresponding to the circumsolar part as seen from the inclined plane a and the horizontal plane c, the circumsolar and the horizon brightness coefficients F_1 and F_2. Please see Appendix A.1 for further details of the calculation with the Perez model.

6.1.3 Accuracy of the GVI calculation

Figure 6.1 schematically shows the simulation procedure that I use to evaluate the accuracy of the global vertical irradiance (GVI) using different transposition models and with the ground reflection calculated with previously established and the GVF approach. The measured input parameters global horizontal irradiance (GHI) and diffuse horizontal irradiance (DHI) are outlined in blue. Since in practice often only GHI data are available, I performed the simulations not only with measured DHI but also with calculated DHI based on the GHI values, which is illustrated by the dashed red border. I determine the diffuse vertical irradiance (DVI) using GHI, DHI and different transposition models. I_{ground} is determined using the standard model (eq. 2.47) and the GVF with (eq. 2.46) and without ground shading (eq. 2.43). I_{direct} is derived from the DNI which in turn is derived from GHI and DHI. The GVI is the sum of DVI, I_{direct} and I_{ground}. To estimate the economic efficiency of PV systems, the annual yield

is decisive. Therefore, in addition to e (eq. 3.5), I consider the relative deviation

$$\Delta v_{\mathrm{GVI}} = \left| 1 - \frac{\sum_{i=1}^{N} GVI_{i,\mathrm{simulated}}}{\sum_{i=1}^{N} GVI_{i,\mathrm{measured}}} \right| \tag{6.10}$$

of the cumulated annual insolation. Where i indicates the individual values and N the total number of measured GVI_{measured} and simulated $GVI_{\mathrm{simulated}}$ global vertical irradiance values in a 12-month time period.

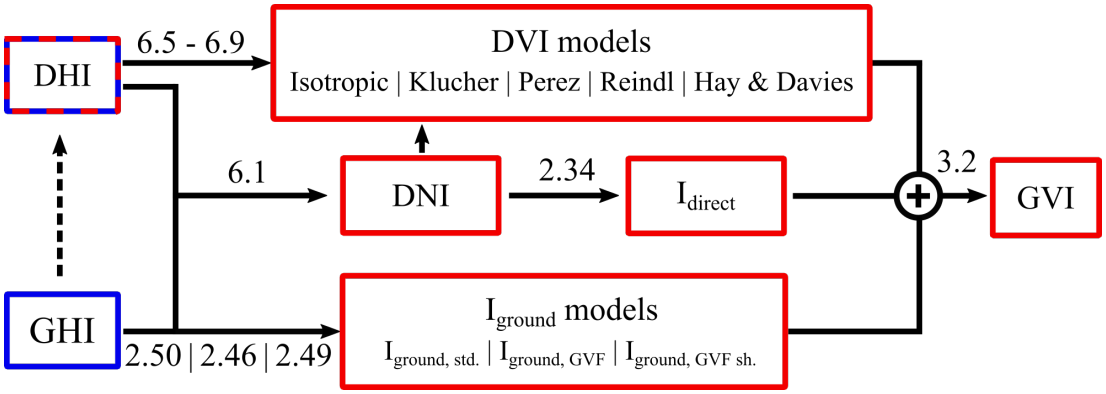

Figure 6.1: Scheme of the simulation series to determine the accuracy of the simulation of the GVI. Measured values are enclosed by a blue rectangle and calculated values by a red rectangle. We use measured GHI and measured or calculated DHI as input values. From this, the DVI, the DNI and I_{ground} are determined with the respective models and I_{direct} is calculated. The sum of DVI, I_{direct} and I_{ground} results in the GVI. The numbers above the arrows indicate the equations used in each case. [33]

I divide the determination of the accuracy of the GVI simulation into three steps. First, I only calculate the DHI and compare the calculated DHI with the measured one. In the second step, I determine the DVI and I_{ground} with the different models and compare the results with the measured DVI. The ground reflection is included in the measured DVI. In the last step, I compare the calculated GVI with the measured one.

6.1.4 Data for annual irradiance calculation

To evaluate the accuracy of the calculation of irradiance on vertical planes, I use four different data sets for comparison.
Figure 6.2 shows the test facility on a south façade at one of our buildings at the Institute for Solar Energy Research Hamelin (ISFH). We measure the irradiance with pyranometers of the type CM11 (Kipp & Zonen). One pyranometer measures the GVI (1) at the façade, one the DVI (2) and a third one the GHI (3) on the roof. I also use DHI values measured with a similar pyranometer at a different location at ISFH in a different test facility. The pyranometers are calibrated every two years according to the ISO 9847 standard [29]. All irradiance data are recorded with a 34970A (Agilent) data logger and a time resolution of one minute. Please see section 4.1.8 for more information about the outdoor test facility.

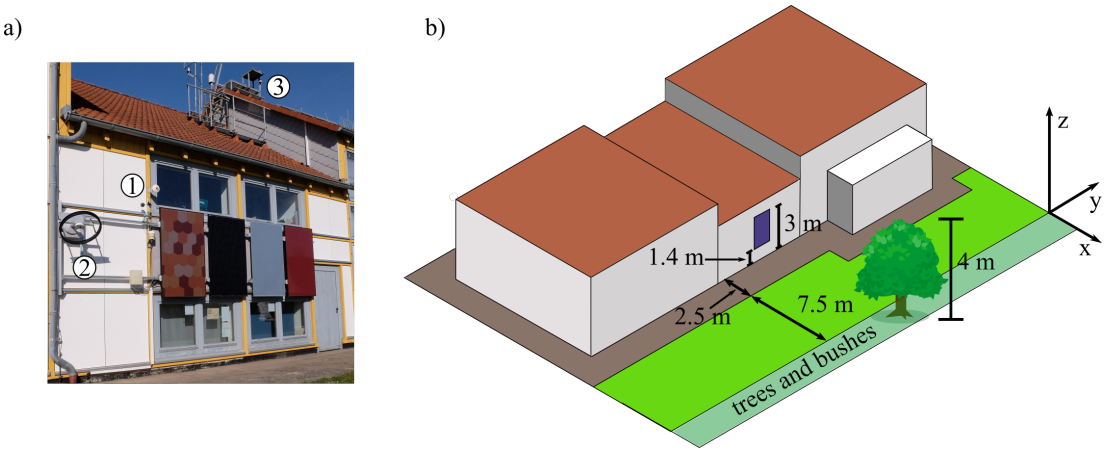

Figure 6.2: a) Picture of the outdoor test facility on a south façade at ISFH. Measurements of GVI (1), DVI (2) and DHI (3) are carried out every minute. b) Illustration of the outdoor test stand with indication of the distances required for the simulation. For a better overview, only one tree is drawn, but there are numerous trees and tall bushes on the area colored in dark green. [33]

One example where the assumption of an infinite open area in front of a PV module is far from true is an urban canyon, i.e. two long buildings of similar height facing each other. For this use case, I compare the GVF model with the results of the ray tracing software CityPV [10]. I simulate the insolation at three PV modules PV1, PV2 and PV3 on the south façade of a building with a height of 15 m in an urban canyon. Figure 6.3 shows the exact geometries of the simulation environment: the three PV modules have dimensions of 1.6 m × 1 m, and the centers are located at heights of 2.8 m, 8.3 m, and 13.8 m, respectively. On the opposite side there is a building of height 15 m, with a façade of albedo $\rho_3 = 0.18$. This albedo corresponds to concrete. The distance between the buildings is 13 m, and ground consists of two 3 m wide sidewalks with albedo $\rho_1 = 0.34$ and an asphalted road with albedo $\rho_2 = 0.08$. All geometries extend to a length of 150 m, with the PV modules located in the center. [33]

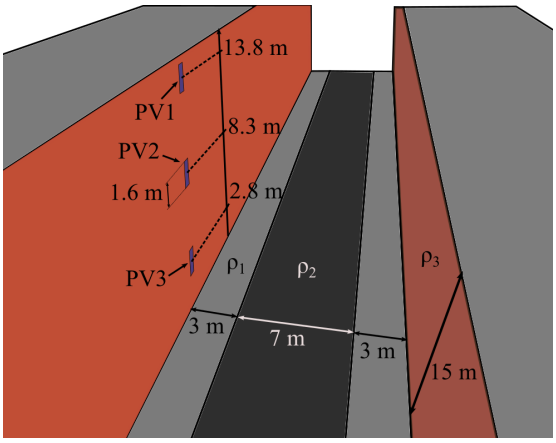

Figure 6.3: Simulation environment for the determination of the insolation on the three PV modules PV1, PV2 and PV3 on the south façade of a building in an urban canyon. [33]

As reference data, I simulate the hourly GVI for one year using the typical meteorological year for Hanover (period 2005 - 2014) [45] to compare it with calculated

GVI using the different ground reflection models. I use the annual insolation computed with CityPV and analytically calculate the radiation reflected from the ground onto the PV modules $I_{\text{ground, std.}}$, $I_{\text{ground, GVF}}$ and $I_{\text{ground, GVF sh.}}$ with equations (3.4), (2.43) and (2.46). I compare both the cumulative annual GVI at the modules, and the relative deviation Δv_{GVI} determined using eq. (6.10).

As a third source of reference data I use measured data, from the IMUK and a typical mean year (TMY). The measurement data from the IMUK include the GHI and GVI measured every minute in the south direction for the years 2016 to 2019. The irradiance is recorded with solar sensors based on silicon detectors on the roof of the institute building (Figure 6.4). The TMY for the ISFH site is obtained from Photovoltaic Geographical Information System (PVGIS) for the period from 2007 to 2016 [45]. Unlike the data measured at ISFH and IMUK, the TMY data is available on an hourly basis only.

Figure 6.4: Radiation sensors on the roof of the IMUK building. Image taken from [63].

Using CityPV as well as the measured data from IMUK and the TMY, I analyze only the deviations of the annual sums of the calculated irradiation and the reference data.

6.2 Dependence of I_{ground} on environmental parameters

First, I compare the influence of the different input parameters in eq. (2.43) on the calculation of the GVF for a façade module to estimate the reflected radiation I_{ground} incident on a PV module. Figure 6.5 a) shows the GVF for façade modules mounted at a height between 0 m and 10 m for three differently sized areas in front of the PV module. The position of the PV modules that are mounted at the ISFH is marked with a blue vertical line. In our test facility at ISFH, the open area A_{ISFH} is limited by a row of trees at a distance of 10 m in front of the façade (see Fig. 4.6 b). The GVF is highest for modules where the bottom edge touches the ground with $GVF_{\text{ISFH}} = 0.5$

and decreases to a value of 0.1 at a mounting height of $h = 10$ m (red dashed line). If a larger open area A_{limited} is assumed, where the open area in front of the façade is limited by an object after a distance of 25 m, the GVF decreases linearly from the maximum of 0.5 at $h = 0$ m, reaching a GVF of 0.3 at $h = 10$ m (blue dashed line). The GVF for an infinitely extended, open area is constant at 0.5 and independent of h (green dashed line). This value is identical to the factor from the typical calculation for ground reflection for vertically mounted PV modules in eq. (3.4). [33]

In Figure 6.5 b), I compare the calculated reflected GHI for two ways in which a ground made up of two different albedos is considered. Using eq. (2.43) we look at the area A_{ISFH}, which is 25% covered with concrete with an albedo of $\rho_{\text{concrete}} = 0.36$ and 75% covered with green grass with an albedo of $\rho_{\text{green grass}} = 0.27$ [87]. This results in an average albedo of $\rho_{\text{average}} \approx 0.29$ for the entire area (without view factor weighting). Figure 6.5 b) shows that using the average albedo (red dashed line) as opposed to two different albedos for the two sub-areas (blue dashed line) underestimates the fraction R_{ground} reflecting incident radiation onto a PV module for PV modules mounted lower than 4 m. This is because the area directly in front of the façade, which has a greater influence on low-mounted PV modules, has the higher albedo ρ_{concrete}. The calculated R_{ground} values for the average and separate albedo are almost identical for modules with a mounting height above 4 m. [33]

Please keep in mind that this is a theoretical consideration to illustrate the influence module mounting height and available open area have on the ground view factor. At the ISFH façade test facility, a module mounting height of more than 4 m would not be possible due to the building height. With a higher module position, the open area would also change, since the module would view over the trees.

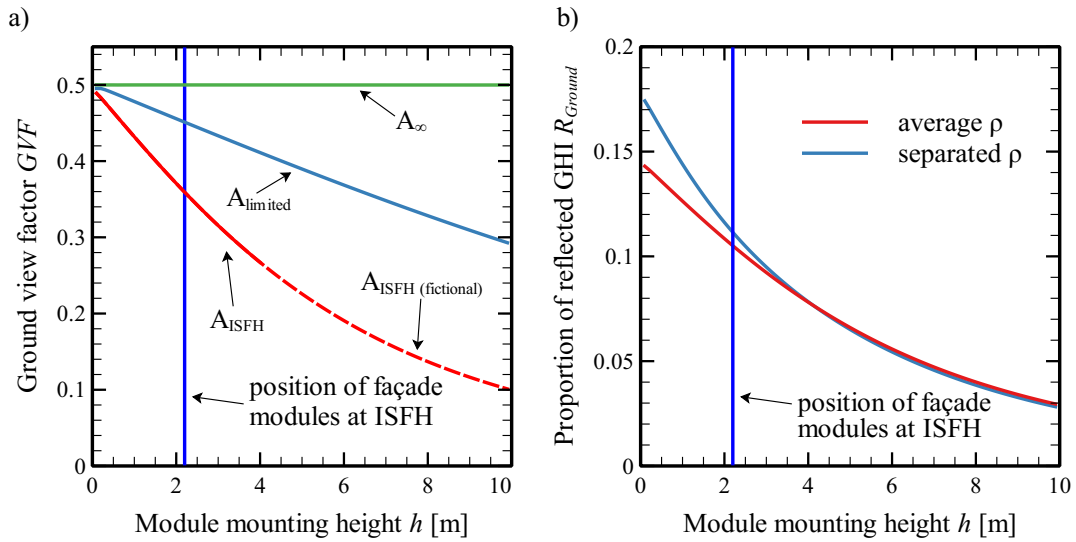

Figure 6.5: a) Calculated GVF for various open areas in front of PV modules mounted on a façade at heights between 0 m and 10 m. b) Calculated R_{ground} using an average (red dashed line) and separated (blue dashed line) albedos ρ for PV modules mounted on a façade at heights between 0 m and 10 m. The mounting position of the PV modules at ISFH is indicated by the dark blue line. [33]

6.3 Accuracy of various irradiation calculation models

In the following, I investigate the accuracy of models for calculating the diffuse radiation fraction from the GHI and models for transposing the diffuse horizontal irradiance to the vertical plane. Afterwards, I consider the accuracy of the calculation of GVI, which depends on the accuracy of each model. To evaluate the accuracy, I consider a 24-month period (04.2020 - 03.2022) during which we measured GHI, GVI, DVI, and DHI. I evaluate each model firstly by the relative deviation Δv of the cumulated calculated to the cumulated measured irradiance in the whole period and secondly by the relative root mean square error e.

6.3.1 Accuracy of decomposition models

When only the GHI is available, a decomposition model is used to determine the direct (DNI) and diffuse (DHI) components from the GHI. I use five models: the model of Erbs *et al.* [27], of Reindl *et al.* [72], the DISC model [61], the DIRINT model [47], and the model of Orgill and Hollands [67]. Figure 6.6 a) shows the relative deviation Δv of the cumulative calculated from the measured DHI and the corresponding e for the time period studied. With $\Delta v_{\mathrm{DISC}} = 0.03$ and $e_{\mathrm{DISC}} = 0.22$, the DISC model leads to the best result. The largest deviation $\Delta v_{\mathrm{O.\,\&\,H.}} = 0.1$ with $e_{\mathrm{O.\,\&\,H.}} = 0.28$ is observed for the model of Orgill and Hollands. Figure 6.6 b) shows the correlation between the DHI values calculated with the DISC model and the measured DHI values. In case of an exact match, all points would lie on the red straight line, but a significant dispersion is apparent. The calculated DHI values of the other four models are shown in the appendix in figure A.1.

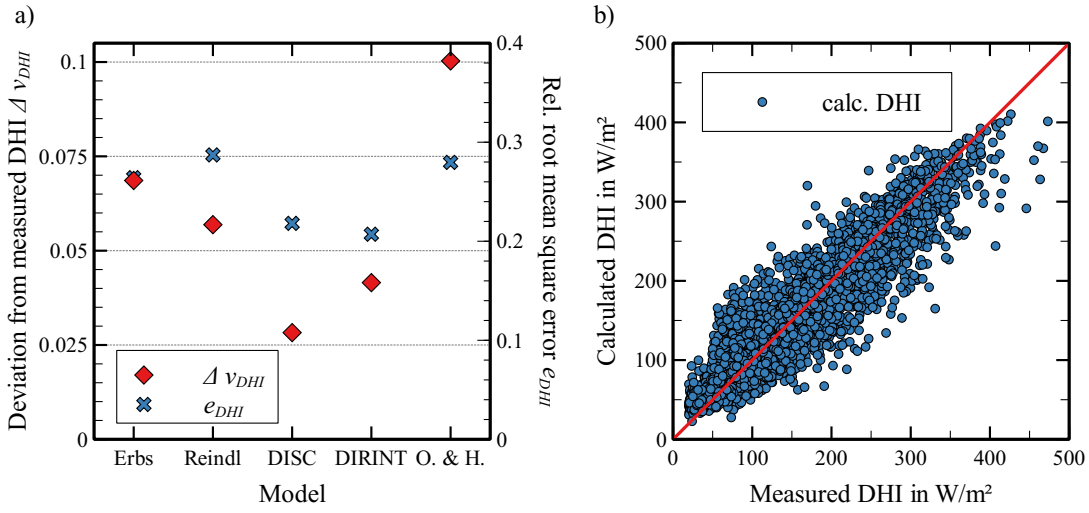

Figure 6.6: a) deviation Δv (red diamonds) and relative root mean square error e (blue crosses) between measured DHI and DHI calculated with five different models for a 24-month time period. b) Correlation between the calculated DHI using the DISC model and the measured DHI.

6.3.2 Accuracy of transposition models

The isotropic model of Liu and Jordan and the anisotropic models of Reindl *et al.*, Klucher *et al.*, Hay and Davies, and Perez *et al.* were tested to transpose the DHI to the vertical plane. Figure 6.7 a) shows the deviation between the cumulated measured and calculated DVI Δv_{DVI} and Figure 6.7 b) the relative root mean square error e_{DVI} of the respective models. A distinction is made in the input parameters. In addition to the measured GHI, I use on the one hand measured DHI (diamonds) and on the other hand DHI calculated with five different models (boxplots). The central horizontal line in the boxplots indicates the median and the cross indicates the mean. The upper and lower bound of the box mark the 25^{th} and 75^{th} percentile. The lower and upper ends of the error bar mark the minimum and maximum value. In addition, three methods for calculating ground reflectance are examined: $I_{\mathrm{ground,\,std.}}$ (blue), $I_{\mathrm{ground,\,GVF}}$ (green) and $I_{\mathrm{ground,\,GVF\,sh.}}$ (red).

With measured DHI, small deviations of $\Delta v_{\mathrm{DVI}} < 0.1$ between measured and calculated DVI can be obtained for the isotropic model and the model of Hay & Davies with $I_{\mathrm{ground,\,std.}}$ and for all models, except the isotropic one, using $I_{\mathrm{ground,\,GVF}}$ or $I_{\mathrm{ground,\,GVF\,sh.}}$. For all models, e_{DVI} ranges from 0.14 to 0.27, no matter which model for the calculation of the ground reflection is used.

When using calculated DHI, a similar situation is obtained: When DVI is calculated with $I_{\mathrm{ground,\,std.}}$, the best results, both in terms of deviation and e_{DVI}, are obtained with the isotropic model and the model of Hay & Davies. Exactly the other way around is the case when using $I_{\mathrm{ground,\,GVF}}$ and $I_{\mathrm{ground,\,GVF\,sh.}}$. It is noteworthy that Δv_{DVI} is significantly lower for the anisotropic models when using $I_{\mathrm{ground,\,GVF}}$ or $I_{\mathrm{ground,\,GVF\,sh.}}$. Only when using the model of Hay & Davies, v_{DVI} is lower when using $I_{\mathrm{ground,\,std.}}$. Furthermore, it is evident from Figure 6.7 b) that the different models used to calculate DHI have very little effect on e_{DVI}.

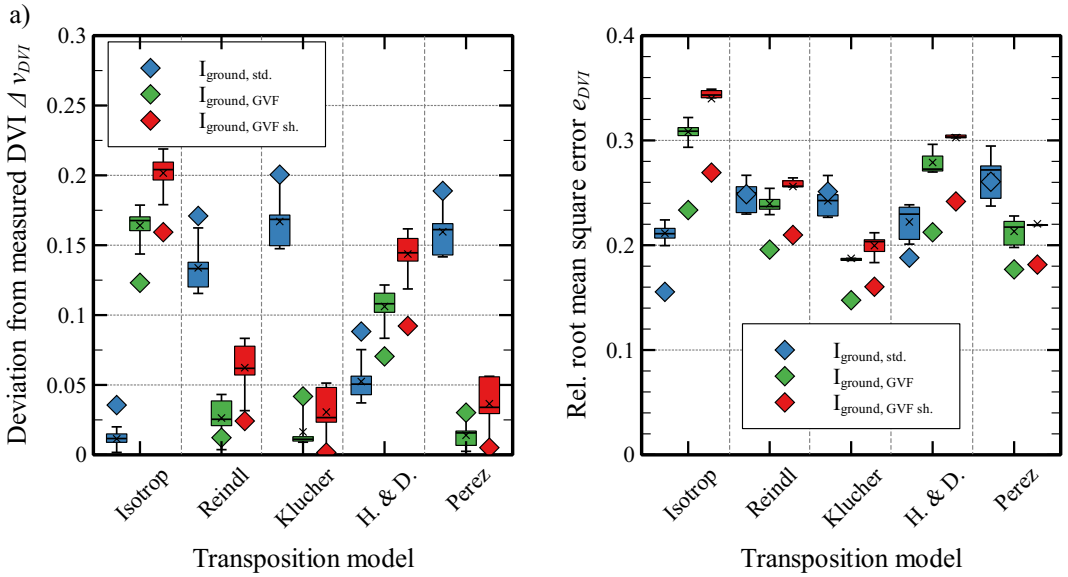

Figure 6.7: a) Deviation Δv_{DVI} between cumulated measured DVI and DVI calculated with five different models for a 24-month period. b) e_{DVI} for the calculated DVI of each model. I distinguish between calculated DVI with measured DHI (diamonds) and with calculated DHI (box plots) as input data. Moreover, three methods are used to calculate I_{ground}: standard (blue), GVF (green), and GVF with consideration of ground shading (red).

In the next step, I evaluate the total irradiance hitting the façade, thus the GVI. Figure 6.8 shows the Δv_{GVI} (a) and e_{GVI} (b) for the different transposition models and ground reflectances used to calculate the GVI. Compared to the calculation of DVI, Δv_{GVI} and e_{GVI} are significantly smaller. It can also be seen from the boxplots that the choice of model used to calculate the DHI does not have a large effect on the calculated GVI. Only when the isotropic model is used e_{GVI} varies in a range of 0.03. For all other models, Δv_{GVI} and e_{GVI} vary by a maximum of 0.02. With the inclusion of direct irradiance, the isotropic model and the model of Hay & Davies evolve into the ones with the lowest Δv_{GVI} and e_{GVI} results. Unlike Δv_{DVI}, Δv_{GVI} is always smaller when using $I_{\mathrm{ground,\,GVF}}$ and $I_{\mathrm{ground,\,GVF\,sh.}}$ than when using $I_{\mathrm{ground,\,std.}}$.
When using $I_{\mathrm{ground,\,GVF}}$ or $I_{\mathrm{ground,\,GVF\,sh.}}$, e_{GVI} ranges from 0.1 to 0.17 with all models. Using $I_{\mathrm{ground,\,std.}}$, a value of 0.14 can be obtained with the isotropic model, and with the anisotropic models, e_{GVI} ranges from 0.17 to 0.24.

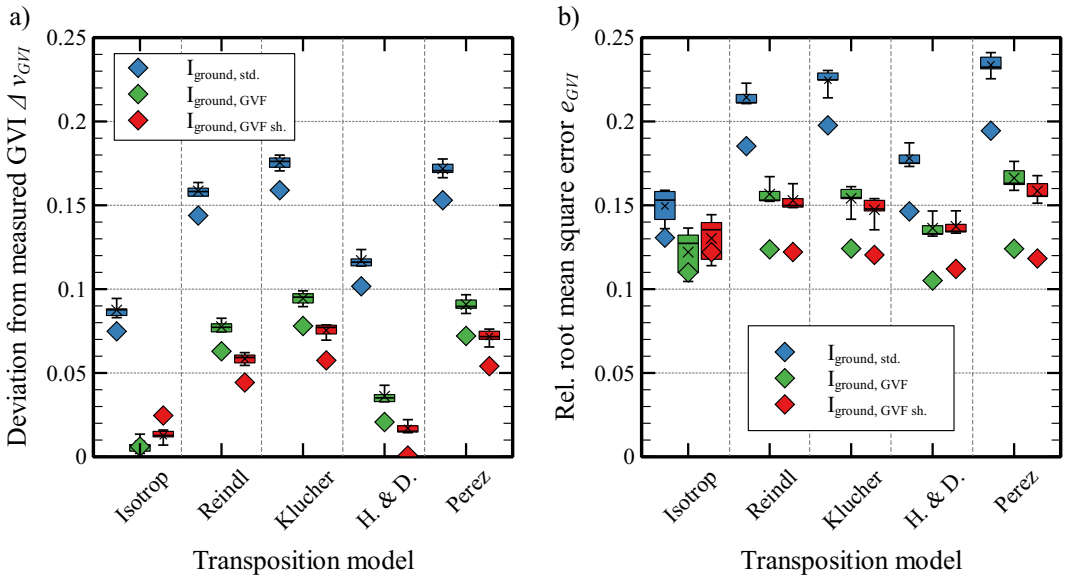

Figure 6.8: a) Deviation Δv_{GVI} between cumulated measured and calculated GVI for a 24-month time period. b) Relative root mean square error e_{GVI} for the GVI of each model. We distinguish between GVI calculated with measured DHI (diamonds) and with calculated DHI (box plots) as input data. Moreover, three methods are used to calculate I_{ground}: standard (blue), GVF (green), and GVF with consideration of ground shading (red). The central horizontal line in the boxplots indicates the median, and the cross indicates the mean. The upper and lower bound of the box mark the 25^{th} and 75^{th} percentile. The lower and upper ends of the error bar mark the minimum and maximum value.

Table 6.1 shows the improvement of the derived deviation Δv_{GVI} and error e_{GVI} by using calculated DHI and the GVF with and without ground shading compared to the GVI determined using $I_{\mathrm{ground,\,std.}}$. By using the GVF all values, i.e. the minimum, mean and maximum deviation Δv_{GVI} and e_{GVI}, are lowered and thus improved. In contrast, only a small improvement is achieved by adding the ground shading. One reason for the lack of improvement by including ground shading is that the objects causing the shades at ISFH are a row of trees and not a massive object. It was assumed that throughout the year an object of height 4 m shadows the ground. However, depending on the season, the trees allow different amounts of light to pass through, resulting in some inaccuracy.

Table 6.1: Improvement of Δv_{GVI} and e_{GVI} by using GVF and GVF with ground shading compared to the standard method of calculating I_{ground}, based on measured GHI and calculated DHI for the time period of April 2020 to January 2022. Given in absolute percentage differences.

	Improvement compared to $I_{\mathrm{ground,\,std.}}$					
I_{ground} method	min Δv	$\overline{\Delta v}$	max Δv	min e	$\overline{e}$	max e
GVF	8.1%	8.1%	8.1%	2.3%	5.3%	7.2%
GVF w. shadow	6.7%	9.5%	10.1%	1.5%	5.5%	7.9%

6.3.3 Annual deviation of the irradiance

Figure 6.9 a) shows the maximum, mean and minimum cumulative GHI per month measured at the ISFH from 1996 to 2020, as well as the cumulative GHI per month of the PVGIS - TMY for the ISFH site for the period 2007 - 2016. On average, the total cumulative GHI differs from year to year by 3.6%, the mean difference to the TMY is 4%. Due to the natural deviation of the annual irradiation, an exact yield forecast is not possible. However, this makes errors caused by the different models of the radiation calculation less significant. Figure 6.9 b) shows the ratios between calculated and measured annual GVI. On the one hand, the measured data from the respective year was used as input data for the calculation, on the other hand, the TMY from PVGIS. I chose the transposition model of Hay and Davies, as it achieves the best results for Lower Saxony. I use the standard ground reflection method for the calculation of the vertical irradiance at IMUK, since the measurement there takes place on the roof of the institute building and not at a façade. Thus, there are no obstacles in the surroundings and the case of an infinitely extended surface that contributes to the ground reflection can be assumed. For the radiation calculation at the ISFH, the GVF with ground shading was used. Despite the high e of about 12% when determining the hourly GVI values, I determined the total annual insolation on the façade with a significantly smaller deviation, as the overestimated and underestimated values balance each other out over the course of a whole year. With the additional data from the IMUK, it is clear that the small deviation in the years we measured at ISFH does not just occur by chance. The ratios calculated using the TMY show that larger annual deviations occur if the annual GHI differs significantly from the GHI in the TMY.

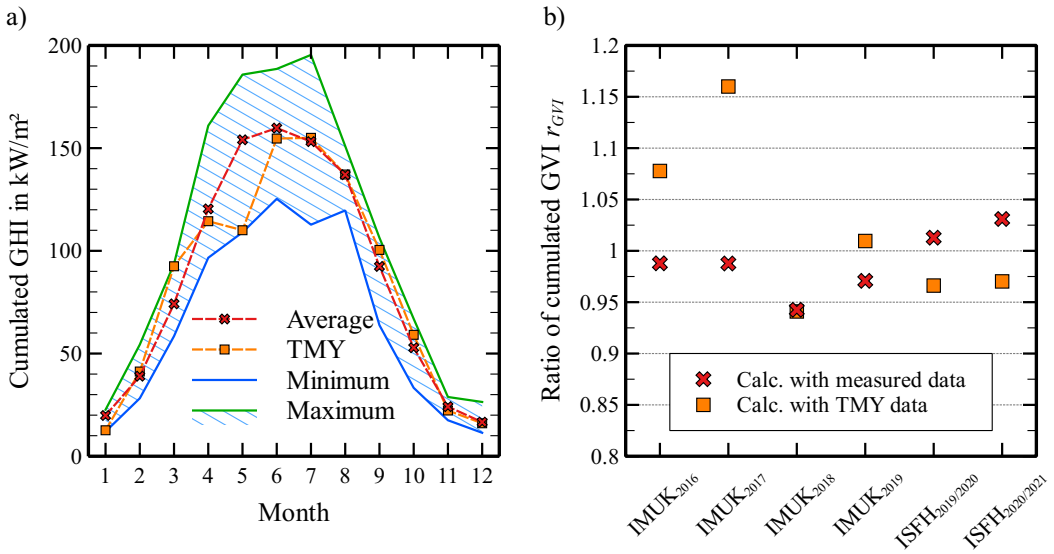

Figure 6.9: a) Minimum (blue line), maximum (green line) and mean (red crosses) monthly GHI measured at ISFH in the years 1996 to 2020 and the cumulative monthly GHI from the TMY for the period 2007 to 2016 (orange squares). b) Ratio between calculated and measured annual irradiation at the façade. Measured data of the respective year (red crosses) and from the TMY (orange squares) were used as input data.

6.4 Energy yield calculation for façade modules

To achieve a certain accuracy for an energy yield prediction for the future, we must be capable of calculating the yield as accurately as possible for given input parameters. Based on the calculation of GVI with different models for determining DHI, DVI and I_{ground} from the previous section, I now calculate the energy yield for façade modules. I will first calculate the yield for a standard PV module and then calculate the yield for a CoTex module. In contrast to the last section, I consider a period of one year only, in which the power output of both modules was recorded every minute.

6.4.1 Accuracy of yield calculation for façade modules

To determine the accuracy of the yield calculation, the same procedure was used as in the previous section for the calculation of DVI and GVI. On the one hand, measured DHI was used and on the other hand, DHI was determined with five different models from the GHI. The transposition of diffuse radiation from the horizontal to the vertical plane was also performed with five different models. For the ground reflection, the three variants $I_{\text{ground, std.}}$, $I_{\text{ground, GVF}}$ and $I_{\text{ground, GVF sh.}}$ were used. Since the irradiation has the greatest influence on the PV yield, the deviation Δv_{P} between the cumulated measured and calculated yield and also the relative root mean square error e_{P} have a similar distribution to the accuracy of the GVI.
Figure 6.10 shows Δv_{P} and e_{P} between calculated and measured energy yield of the standard PV façade module. The deviations are slightly lower and e_{P} is slightly higher than when calculating the GVI. Again, I achieve better results using the GVF than using the standard ground reflection for each model. With the isotropic model and the model of Hay and Davies, when using the GVF (with and without ground shading) deviations of less than 3% can be achieved. The error e_{P} is lowest for the isotropic model, where it is between 12% and 14%. For all other models, e_{P} varies between 14% and 20% when using the GVF and between 17% and 25% when using $I_{\text{ground, std.}}$. Using measured DHI results in a slight improvement in some cases and a small deterioration in others, but never a large difference from the result with calculated DHI.
Please keep in mind that for the investigation of the yield prognosis only a period of 12 months is considered. The deviations depend on the time of year, so when observing a whole year, the deviations partially nullify each other. Therefore, considering the root mean square error e_{P} is more meaningful for comparing the accuracy between the prediction of the GVI and the energy yield.

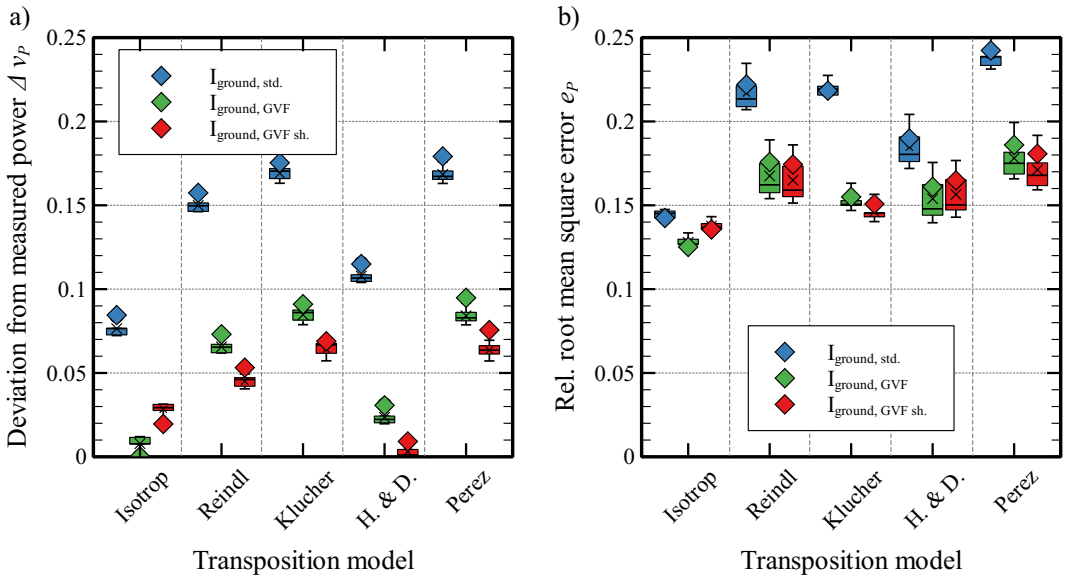

Figure 6.10: a) Deviation Δv_P between measured and calculated energy yield with five different transposition models für a 12-month period. b) e_P for the calculated energy yield of each model. I distinguish between calculated energy yield with measured DHI (diamonds) and with calculated DHI (box plots) as input data. Moreover, three methods are used to calculate the irradiance reflected from the ground: $I_{\mathrm{ground,\,std.}}$ (blue), $I_{\mathrm{ground,\,GVF}}$ (green), and $I_{\mathrm{ground,\,GVF\,sh.}}$ (red).

6.4.2 Accuracy of energy yield calculation of CoTex modules

Back in chapter 4.2.6, when comparing long-term outdoor and laboratory measurements, I found that a small discrepancy exists between the ratio of energy yields under STC measurements and in real operation. The ratio between the power output of the CoTex module and the reference module is 86% in flasher measurements, but only approx. 85.5% after a 12-month measurement period on the façade (see table 4.3). I consider the module temperatures and the angle dependence to explain the discrepancy. Figure 6.11 a) shows the ratio $r_{Temp.}$ between the module temperatures as a function of GVI. On average, the temperature of the CoTex module is $\overline{r}_{Temp.} = 0.976$ of the temperature of the reference module (dashed red line). Since more light is reflected by the CoTex layer, the temperature of the module is also lower. However, the temperature difference is only small.

A larger difference becomes evident in Fig. 6.11 b). The power ratio between the CoTex and the reference module r_{power} is plotted against the angle of incidence (AOI) θ. The flasher measurement showed $r_{power,\,STC} = 0.86$ at STC (red dashed line). However, outdoor measurements show a clear angular dependence: at acute AOI of $\theta \leq 30°$ the mean ratio is $\overline{r}_{power,\,\theta \leq 30°} = 0.86$, some outliers also reach values of up to 0.8 and 0.9. At more obtuse AOI a decrease of the ratio is clearly visible. For example, at $40° \leq \theta \leq 60°$ it is $\overline{r}_{power,\,40° \leq \theta \leq 60°} = 0.849$.

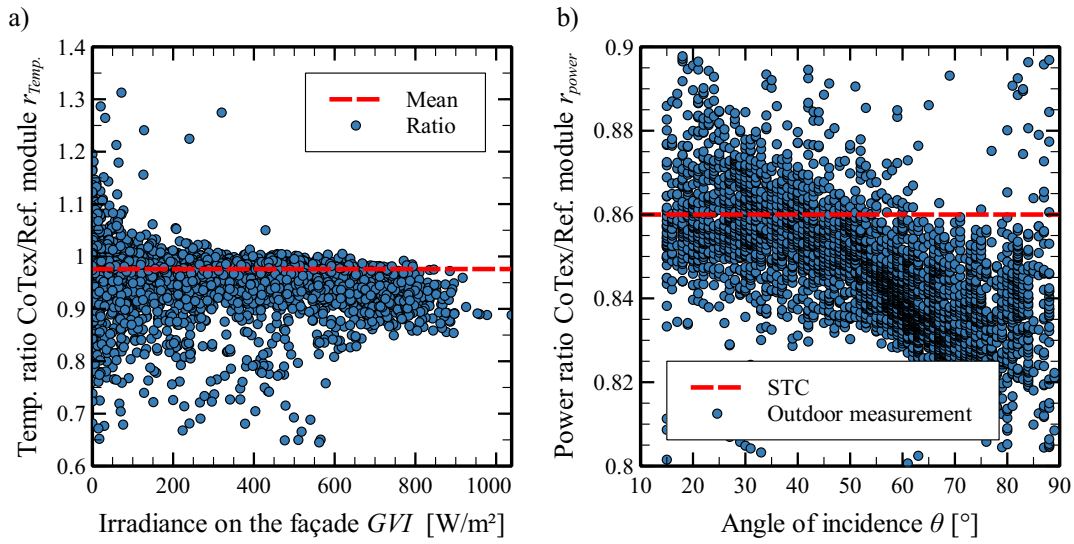

Figure 6.11: a) Ratio $r_{Temp.}$ between the module temperature of the CoTex module and the reference module on the façade at ISFH as a function of GVI. The ratio is $\overline{r}_{Temp.} = 0.976$ on average (red dashed line). b) Ratio r_{power} between the power output of the CoTex module and the reference module on the façade at ISFH as a function of the AOI θ. The flasher measurement showed $r_{power,\,STC} = 0.86$ under STC (dashed red line).

The measurement data allow the calculation of an AOI-dependent correction factor by which the calculated energy yield of the CoTex module is multiplied. I calculate the relative transmission of the CoTex layer for the measured values of 12 months according to equation (2.49). The linear fit function

$$\tau_{\mathrm{CoTex}}(\theta) = -0.0005\theta + 1.011 \tag{6.11}$$

describes the relative transmission and is used for the yield prognosis of any CoTex module.

Figure 6.12 shows the accuracy of the energy yield calculation for the CoTex module with (blue, green and red diamonds and box diagrams) and without (grey, light green and orange crosses and box diagrams) the AOI correction τ_{CoTex}. The use of the AOI correction reduces the deviation Δv_{PC} of the calculated from the measured energy yield by 0.018 on average and the e_{PC} by 0.011. With the AOI correction I achieve an almost identical accuracy in the yield calculation of CoTex façade modules as with standard façade modules.

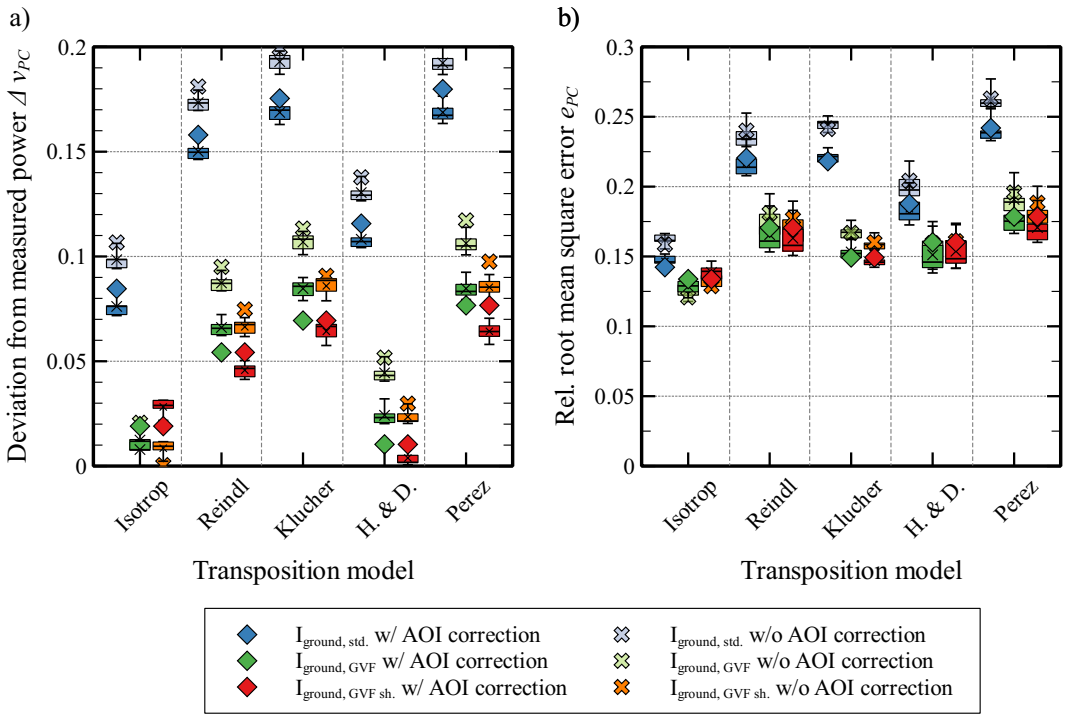

Figure 6.12: a) Deviation Δv_{PC} between measured and calculated energy yield of a greyish CoTex module with five different transposition models for a 12-month period. b) e_{PC} for the calculated energy yield of each model. I distinguish between calculated energy yield with measured DHI (diamonds) and with calculated DHI (box plots) as input data. Shown are the results with and without the AOI correction. Moreover, three methods are used to calculate the irradiance reflected from the ground: $I_{\mathrm{ground,\,std.}}$ (blue and grey), $I_{\mathrm{ground,\,GVF}}$ (green and light green), and $I_{\mathrm{ground,\,GVF\,sh.}}$ (red and orange).

6.5 Conclusion of Chapter 6

A reliable yield forecast for PV modules is essential for professional planning and estimation of the payback period. Numerous scientific papers have shown that, especially when only the GHI is available as an input parameter, the calculation of insolation in the vertical plane is significantly more error-prone than for rooftop modules with a tilt angle smaller than 50°. For vertically mounted modules, the fraction of radiation reflected from the ground occupies a larger portion of the total irradiance and is therefore more relevant than for PV modules with lower tilt angles.

The previously established calculations for ground reflection [22] assume an infinitely extended open area in front of the PV modules, which is, in general, not the reality. The approach of using a ground view factor allows a more accurate calculation of the ground reflection by defining the area to be considered, including varying albedos and thus also taking into account the mounting height of the PV module.

Also known from the literature [18, 20, 44, 46, 52, 56, 59, 63, 64, 73] and shown again in this study, the model which is used for transposing the horizontal insolation into the vertical plane is decisive for the accuracy. So far, no criterion is known which allows a reliable selection of the transposition model best suited for a location. Consequently, for a general interpretation of my results, the worst-case, i.e. the least-suitable model

must be considered. Therefore, the conclusion of this section is that for the particular test stand at the ISFH using the GVF with ground shading reduces the expected deviation of the calculated cumulative insolation at a façade after a 24-month period by 10.2% to 7.8% if the worst-fitting transposition model is selected and to 0.7% if the best-fitting transposition model is selected. On average I find a 9.5% improvement.
Depending on the geometries, the improvement by using the GVF with shading can easily be significantly larger than for the ISFH outdoor test facility. This is shown by the simulation of insolation on PV modules on a façade in an urban canyon, where the deviation of the calculated annual global vertical irradiance using the standard method is up to 34.7%.
The accuracy of the energy yield simulation is only slightly lower than that of the irradiance calculation. For a standard PV module on a façade, the deviation Δv_{P} of the cumulative energy yield over a period of 12 months can be reduced by 10.5% to 0.3% by using $I_{\mathrm{ground,\,GVF\,sh.}}$. The root mean square error e_{P} is between 14% and 18%. For CoTex modules where the appearance has been altered by the application of a colored textile, a similar level of accuracy can be achieved by using an angle of incidence dependent correction to the relative transmission through the CoTex layer.
For planning to purchase PV modules or to build a PV park, whole years are considered for calculating the payback period and the energy gain. Therefore, another important result in this chapter is that for both the calculation of irradiance and energy yield, the relative deviation Δv between the cumulative calculated and measured irradiance or energy yield for long periods of at least 12 months are significantly smaller than the relative root mean square errors e when determining minutely or hourly values.

Chapter 7

Summary

The goal of this work was the development and validation of a new method to alter the appearance of photovoltaic modules, as well as the energy yield prediction of those modules. This approach to modify the appearance of PV modules had to differ from the known methods, especially in the area of flexibility during manufacturing. Furthermore, a procedure for the simulation of a digital prototype had to be created, which allows a prediction of the appearance and yield of a PV module. The final aim of this work was the improvement of the accuracy of the yield prognosis for façade modules and in particular the transfer of the yield prognosis on colored PV modules.

7.1 Fabrication and validation of the CoTex PV modules

I developed the colored textile (CoTex) technique to alter the appearance of PV modules. The technique uses colored textiles or thin fabrics, which are laminated between two layers of encapsulation material on an already manufactured, fully functional PV module. The setup is protected from environmental influences with a weather-resistant front sheet.
Several different materials and colors have been studied in terms of appearance and energy yield of the resulting CoTex modules. With CoTex technology, a PV module can be given a white to grayish appearance by using an unprinted, white nonwoven fabric, thereby a energy yield of the module of 8% - 11%. By using colored or patterned textiles, the appearance of the PV module can be changed as desired. Depending on the material used, the energy loss compared to a PV module without CoTex structure is between 10% and 35%.
The stability of the CoTex structure was subjected to a durability test referring to IEC 61215. No damage to the setup was detected, the appearance of the CoTex module changed slightly. The ratio between the short-circuit current density of the CoTex module under test and a reference module also subjected to the durability test decreased from 0.907 before the test to 0.891 after the test. In a UV stability test, I investigated the extent to which the appearance of CoTex modules containing a color-printed textile in particular changes as a result of UV radiation. For this purpose, a CoTex module

with 9 differently colored and one reference field was exposed to UV radiation of 682.5 kWh/m². After the UV irradiation, the appearance of the colored fields changed by $\Delta E_{00} = 0.99$ on average, and the short-circuit current density decreased by 2.4% on average.
Following the validation through laboratory testing, a reference module and a demonstrator module containing a white unprinted textile were mounted on a south façade of the ISFH for 12 months and the energy yield was measured every minute. In outdoor operation, the ratio of energy yields between demonstrator and reference module decreased by 0.5% compared to the laboratory measurement. During this long-term outdoor measurement, a dependence of the PV yield of the CoTex module on the angle of incidence of the solar radiation became apparent. Compared to the reference module, the angle dependence is significantly stronger, which leads to the fact that the ratio between CoTex and reference module varies periodically with the position of the sun by ±3%.

7.2 Implementation and validation of the simulation of a digital prototype

The appearance of a textile, which is to be used color-printed or unprinted to produce a CoTex module, differs significantly in its raw state from the appearance of the finished CoTex module. The expected loss of energy yield is also dependent on the material used, the color, and the print coverage of each ink. Therefore, I developed the simulation of a digital prototype of CoTex modules, which predicts the energy yield and color of a manufactured CoTex module for arbitrary materials and inks.
To calibrate the simulation for a specific material and specific printing inks, reflectance and *EQE* measurements of a CoTex module with the unprinted material, as well as with the material printed in seven specific colors are necessary. For the measurements, it is sufficient to produce a single CoTex module in which the material contains eight fields in the respective colors and one unprinted field.
I validated the accuracy of the simulation of the digital prototype on a set of four samples: on Freudenberg Performance Light Diffuser in 40 g/m² (FPLD40) printed by an inkjet printer (samples I40), FPLD50 printed by an inkjet (I50) and an offset printer (O50) and a colored semi-transparent foil (CF). The simulations were validated using 51, or in the case of the offset printed FPLD50, 29 color printed samples. The average color difference $\overline{\Delta E_{00}}$ between simulated and measured color was $\overline{\Delta E_{I40}} = 1.69$, $\overline{\Delta E_{I50}} = 2.01$, $\overline{\Delta E_{O50}} = 1.34$, $\overline{\Delta E_{CF}} = 1.22$ and thus hardly perceptible. The mean relative difference $\overline{\Delta r}$ between simulated and measured J_{SC} was $\overline{\Delta r}_{\mathrm{I40}} = 1.3\%$, $\overline{\Delta r}_{\mathrm{I50}} = 1.1\%$, $\overline{\Delta r}_{\mathrm{O50}} = 0.8\%$ and $\overline{\Delta r}_{\mathrm{CF}} = 1.9\%$ and thus also acceptable.
The simulation of the digital prototype allows not only to predict the appearance and yield of any printed CoTex module, but also to find to a requested appearance the combination of material and printing technique that results in the lowest J_{SC} losses.

7.3 Improvement and accuracy of the yield prediction for façade modules

The yield prediction for PV modules mounted vertically on a façade is significantly less accurate when using the usual models than for rooftop PV modules mounted at angles between 30 and 50 degrees. The reason for this is the more complex irradiation situation. Normally, irradiation data is available in the horizontal plane, which must then be transposed to the required inclined plane. Depending on the transposition model used, this conversion becomes less accurate as the angle of inclination of the PV module increases. In addition, the reflected irradiance from the ground takes up a larger portion of the total irradiance incident on the module for vertically oriented modules than for rooftop modules and must therefore be determined more accurately. In this work, I have analyzed five different models each for calculating the fraction of diffuse horizontal irradiance from the global horizontal irradiance and for transposing the diffuse irradiance from the horizontal to the vertical plane. When the total vertical irradiance is considered over a 22 month time period, it is found that the choice of decomposition model does not have a huge impact on the accuracy of the prognosis. The accuracy Δv_{GVI} varies by a maximum of $\pm 1.8\%$ depending on the decomposition model used. The choice of the transposition model, on the other hand, is extremely important. Depending on the transposition model used, the deviation between cumulated measured and simulated irradiance is between 0% and 16%. In addition to the different decomposition and transposition models, a main focus in this chapter was the improved calculation of the reflected irradiance from the ground. For this purpose, I determined the ground view factor of a PV module to include the exact area, different albedos and the mounting height of the module. In the conventional calculation of the ground reflected irradiance, these aspects are not considered. In addition, when calculating the ground reflected irradiance using ground view factor in an extended variant, I also included the shading of the ground by trees in the surrounding area of the test site at ISFH. By using the ground view factor with shading, I was able to significantly increase the accuracy of the yield prediction for a reference module mounted on a south façade of the ISFH for a time period of 12 months. I was able to reduce the deviation of the cumulative energy yield from 8 % - 17 % to 0 % - 7 % and the relative root mean square error from 14 % - 25 % to 14 % - 19 %. When predicting the yield of colored CoTex modules, an angular correction of the angle of incidence of the sun must be included. By using this angular correction, a comparable accuracy can be achieved for CoTex modules as for standard PV modules.

Appendix A

Appendix

A.1 Calculation of the color difference ΔE_{00}

Following [78] ΔE_{00} is calculated as described below:
First the a^*-axis is rescaled with the factor $(1+G)$ and becomes a'.

$$a'_i = (1+G)a^*_i \qquad \text{with} \qquad G = \frac{1}{2}\left(1 - \sqrt{\frac{\bar{C}^{*7}_{ab}}{\bar{C}^{*7}_{ab} + 25^7}}\right), \tag{A.1}$$

with the arithmetic mean $\bar{C}^*_{ab}$ of the vectors $\begin{pmatrix} a^* \\ b^* \end{pmatrix}$ of color 1 and 2:

$$\bar{C}^*_{ab} = \frac{1}{2}\left(\sqrt{a^{*2}_1 + b^{*2}_1} + \sqrt{a^{*2}_2 + b^{*2}_2}\right) \tag{A.2}$$

By this scaling, equal color differences in the a'-b^* layer form circles around one color. Without this scaling they are ellipses, so equal color differences do not have the same distance in the original a*-b*-plane.
$\Delta L'$, $\Delta C'$ and $\Delta H'$ describe the angle-dependent difference of brightness, chroma and hue between two specific colors marked by the indices $i = \{1, 2\}$.

$$\Delta L' = L^*_2 - L^*_1 \qquad \Delta C' = C'_2 - C'_1 \qquad \Delta H' = 2\sqrt{C'_1 C'_2}\sin\left(\frac{\Delta h'}{2}\right) \tag{A.3}$$

where $C'_i = \sqrt{a'^2_i + b^{*2}_i}$. $\Delta h'$ is defined by the tangent function h'_i and the result depends on which quadrant it is in:

$$\Delta h' = \begin{cases} 0, & \text{if } C'_1 C'_2 = 0 \\ h'_2 - h'_1, & \text{if } C'_1 C'_2 \neq 0; |h'_2 - h'_1| \leq 180^\circ \\ (h'_2 - h'_1) - 360^\circ, & \text{if } C'_1 C'_2 \neq 0; (h'_2 - h'_1) > 180^\circ \\ (h'_2 - h'_1) + 360^\circ, & \text{if } C'_1 C'_2 \neq 0; (h'_2 - h'_1) < -180^\circ \end{cases} \tag{A.4}$$

with

$$h'_i = \begin{cases} 0, & \text{if } b^*_i = a'_i = 0 \\ \arctan(b^*_i, a'_i), & \text{otherwise} \end{cases} \tag{A.5}$$

To determine the weighting functions the arithmetic means $\bar{L}'$, $\bar{C}'$ and $\bar{h}'$ are required:

$$\bar{L}' = \frac{1}{2}(L^*_1 + L^*_2) \qquad \bar{C}' = \frac{1}{2}(C'_1 + C'_2)$$
$$\bar{h}' = \begin{cases} \frac{h'_1+h'_2}{2}, & \text{if } C'_1C'_2 \neq 0; |h'_1 - h'_2| \leq 180^\circ \\ \frac{h'_1+h'_2+360^\circ}{2}, & \text{if } C'_1C'_2 \neq 0; |h'_1 - h'_2| > 180^\circ, (h'_1 + h'_2) < 360^\circ \\ \frac{h'_1+h'_2-360^\circ}{2}, & \text{if } C'_1C'_2 \neq 0; |h'_1 - h'_2| > 180^\circ, (h'_1 + h'_2) \geq 360^\circ \\ (h'_1 + h'_2), & \text{if } C'_1C'_2 = 0. \end{cases} \tag{A.6}$$

Now the weighting functions can be calculated:

$$S_L = 1 + \frac{0.015(\bar{L}' - 50)^2}{\sqrt{20 + (\bar{L}' - 50)^2}} \qquad S_C = 1 + 0.045\bar{C}' \qquad S_H = 1 + 0.015\bar{C}'T, \tag{A.7}$$

where T is an experimentally determined, adapted function for the hue weighting function S_H [7]:

$$\begin{aligned} T =& 1 - 0.17\cos(\bar{h}' - 30^\circ) + 0.24\cos(2\bar{h}') \\ &+ 0.32\cos(3\bar{h}' + 6^\circ) - 0.2\cos(4\bar{h}' - 63^\circ) \end{aligned} \tag{A.8}$$

The last term in equation 2.5 improves the accurate interpretation of color differences in the blue area. This function is also empirical.

$$R_T = -2\sin\left(60e^{-\left(\frac{\bar{h}'-275^\circ}{25}\right)^2}\right)\frac{\bar{C}'^7}{\bar{C}'^7 + 25^7} \tag{A.9}$$

A.2 Equations and coefficients for the Perez diffuse transposition model

As already presented in section 6.1, the model of Perez et al. calculates the DVI as follows [70, 71]:

$$DVI = DHI\big[\frac{1}{2}(\cos\alpha)(1 - F_1) + F_1\frac{a}{c} + F_2\sin\alpha\big], \tag{A.10}$$

since we consider modules mounted vertically on the façade, it is $\alpha = 90^\circ$. The parameter a and c represent the solid angles corresponding to the circumsolar part as seen from the inclined plane and the horizontal plane. We compute a and c using the AOI θ and the suns zenit angle θ_Z by:

$$a = max\,, \qquad c = max(\cos 85^\circ,\, \theta_Z). \tag{A.11}$$

Table A.1: Coefficients for the model of Perez et al. for various ϵ. The coefficients were determined on the basis of measurement data from various locations in the USA and Europe. [69]

ϵ	f_{11}	f_{12}	f_{13}	f_{21}	f_{22}	f_{23}
$[1, 1.065]$	-0.008	0.588	-0.062	-0.06	0.072	-0.022
$[1.065, 1.23]$	0.13	0.683	-0.151	-0.019	0.066	-0.029
$[1.23, 1.5]$	0.33	0.487	-0.221	0.055	-0.064	-0.026
$[1.5, 1.95]$	0.568	0.187	-0.295	0.109	-0.152	-0.014
$[1.95, 2.8]$	0.873	-0.392	-0.362	0.226	-0.462	0.001
$[2.8, 4.5]$	1.132	-1.237	-0.412	0.288	-0.823	0.056
$[4.5, 6.2]$	1.06	-1.6	-0.359	0.264	-1.127	0.131
$[6.2, \infty]$	0.678	-0.327	-0.25	0.156	-1.377	0.251

Furthermore we need the sky clearness parameter ϵ and the sky brightness parameter Δ:

$$\epsilon = \frac{DHI + DNI}{DHI}\,, \qquad \Delta = DHI\,\frac{AM}{E_A}, \tag{A.12}$$

where AM is the relative air mass and E_A the extraterrestrial irradiance. Along with a set of empirically determined coefficients f_{ij}, $i = \{1, 2\}$ and $j = \{1, 2, 3\}$ (Table A.1), the circumsolar and horizon brightness coefficients F_1 and F_2 are determined by:

$$F_1 = max\left[0,\, f_{11} + f_{12}\Delta + \frac{\pi\theta_Z}{180} f_{13}\right], \qquad F_2 = f_{21} + f_{22}\Delta + \frac{\pi\theta_Z}{180} f_{23}. \tag{A.13}$$

A.3 Results with different decomposition models

In chapter 6 I show the result of the DHI calculation with the DISC model. Using this model resulted in the best correlation between calculated and measured values. Figure A.1 shows the results using the model of a) Erbs *et al.*, b) Reindl *et al.*, c) the DIRINT model and d) the model of Orgill and Hollands.

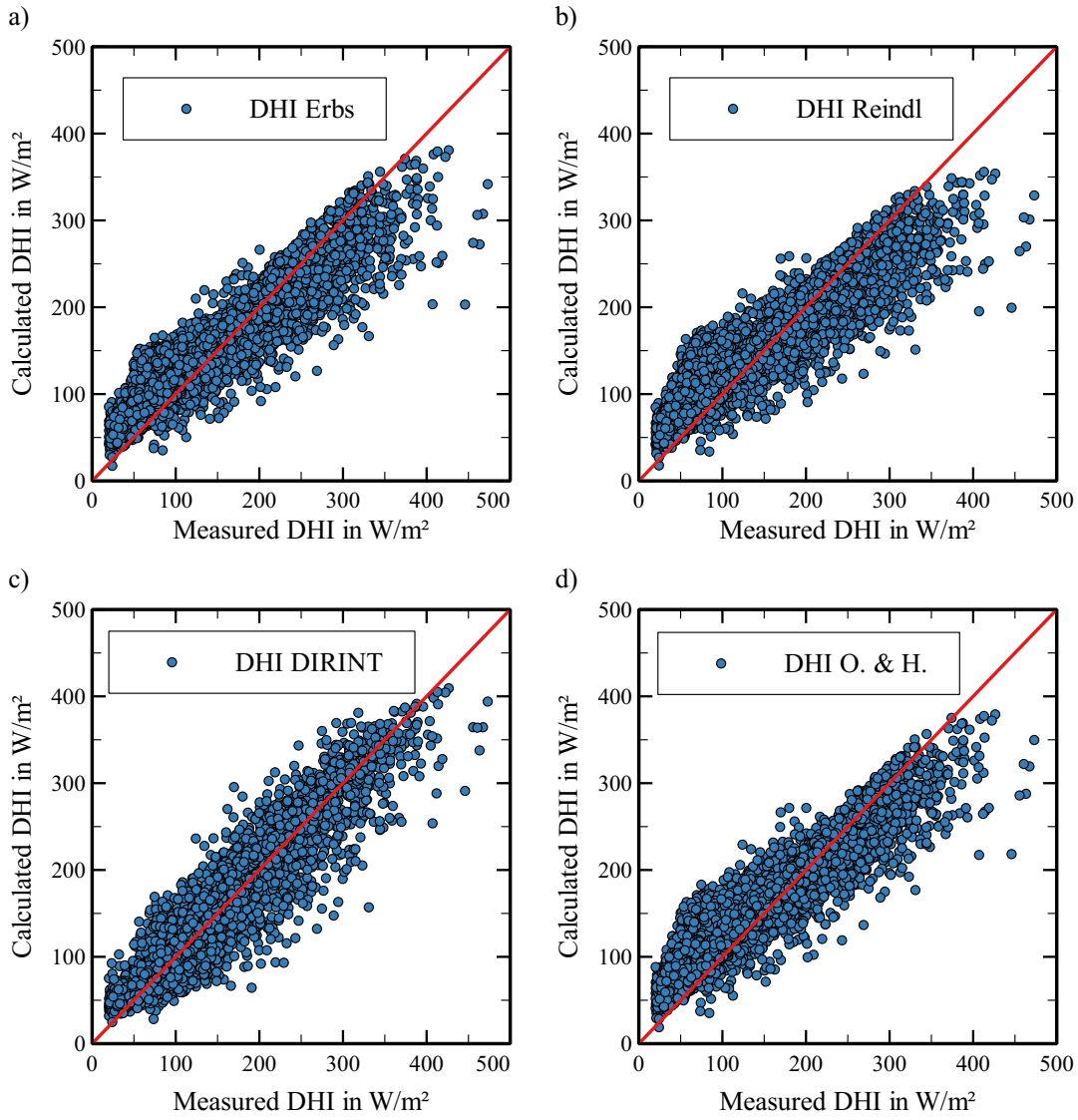

Figure A.1: Correlation between the measured and calculated DHI using the model of a) Erbs *et al.*, b) Reindl *et al.*, c) the DIRINT model and d) Orgill and Hollands.

A.4 Sandia Array Performance Model

To determine the I-V characteristic, I use the Sandia array performance model [54], which uses the equations A.14 - A.21.

$$I_{\mathrm{SC}} = I_{\mathrm{SC,STC}} \cdot f_1\left(\frac{E_{\mathrm{b}} f_2 + f_{\mathrm{d}} E_{\mathrm{d}}}{E_0}\right) \cdot \left(1 + \alpha_{I_{\mathrm{SC}}}(T_{\mathrm{C}} - T_0)\right) \tag{A.14}$$

$$I_{\mathrm{MPP}} = I_{\mathrm{MPP,STC}} \cdot \left(C_0 E_{\mathrm{e}} + C_1 E_{\mathrm{e}}^2\right)\left(1 + \alpha_{I_{\mathrm{MPP}}}(T_{\mathrm{C}} - T_0)\right) \tag{A.15}$$

$$V_{\mathrm{OC}} = V_{\mathrm{OC,STC}} + N_{\mathrm{S}}\delta \ln E_{\mathrm{e}} + \beta_{V_{\mathrm{OC}}}(T_{\mathrm{C}} - T_0) \tag{A.16}$$

$$V_{\mathrm{MPP}} = V_{\mathrm{MPP,STC}} + C_2 N_{\mathrm{S}} \delta \ln E_{\mathrm{e}} + C_3 N_{\mathrm{S}} \left(\delta \ln E_{\mathrm{e}}\right)^2 + \beta_{V_{\mathrm{MPP}}} \left(T_{\mathrm{C}} - T_0\right) \tag{A.17}$$

$$f_1(AM_{\mathrm{a}}) = a_0 + a_1 AM_{\mathrm{a}} + a_2 \left(AM_{\mathrm{a}}\right)^2 + a_3 \left(AM_{\mathrm{a}}\right)^3 + a_4 \left(AM_{\mathrm{a}}\right)^4 \tag{A.18}$$

$$f_2(AOI) = b_0 + b_1 AOI + b_2 \left(AOI\right)^2 + b_3 \left(AOI\right)^3 + b_4 \left(AOI\right)^4 + b_5 \left(AOI\right)^5 \tag{A.19}$$

$$E_{\mathrm{e}} = \frac{I_{\mathrm{SC}}}{I_{\mathrm{SC,STC}} \Big(1 + \alpha_{I_{\mathrm{SC}}} (T_{\mathrm{C}} - T_0)\Big)} \tag{A.20}$$

$$\delta = \frac{n\, k (T_{\mathrm{C}} + 273.15)}{q} \tag{A.21}$$

Bibliography

[1] Directive 2010/31/EU of the European Parliament and of the Council of 19 May 2010 on the Energy Performance of Buildings (Recast). Technical report, European Parliament, Brussels, BEL, 2010.

[2] Agfa. Anapurna fb2540i led. https://www.agfa.com/printing/products/anapurna-fb2540i-led/, 2018. [Online; accessed May 07, 2023].

[3] I. A. Al-Mofeez, M. Y. Numan, K. A. Alshaibani, and F. A. Al-Maziad. Review of typical vs. synthesized energy modeling weather files. *Journal of Renewable and Sustainable energy*, 4(1):012702, 2012.

[4] P. Alessi, M. Brill, J. C. Acosta, E. Carter, R. Connelly, J. Decarreau, R. Harold, R. Hirschler, B. Jordan, C. Kim, et al. 'colorimetry-part 6: Ciede2000-colour-difference formula. *ISO/CIE*, pages 11664–6, 2014.

[5] D. Alman, R. Berns, H. Komatsubara, W. Li, M. Luo, M. Melgosa, J. Nobbs, B. Rigg, A. Robertson, and K. Witt. *Improvement to industrial colour-difference evaluation*. Commission Internationale de l'Éclairage Vienna, 2001.

[6] R. Arndt and R. Puto. Basic understanding of iec standard testing for photovoltaic panels. *Compliance Magazine*, 2010.

[7] R. S. Berns. Derivation of a hue-angle dependent, hue-difference weighting function for ciede2000. In *9th Congress of the International Colour Association*, volume 4421, pages 638–641. International Society for Optics and Photonics, 2002.

[8] Biology Questions and Answers. Human eye. https://www.biology-questions-and-answers.com/images/Human-Eyes.jpg, 2020. [Online; accessed May 07, 2023].

[9] B. Bläsi, T. Kroyer, O. Höhn, M. Wiese, C. Ferrara, U. Eitner, and T. Kuhn. Morpho butterfly inspired coloured bipv modules. *33rd European Photovoltaic Solar Energy Conference and Exhibition; 2630-2634*, 2017.

[10] D. Bredemeier, C. Schinke, T. Gewohn, H. Wagner-Mohnsen, R. Niepelt, and R. Brendel. Fast evaluation of rooftop and façade pv potentials using backward ray tracing and machine learning. In *2021 IEEE 48th Photovoltaic Specialists Conference (PVSC)*, pages 0294–0299, 2021.

[11] I. N. Bronstein, J. Hromkovic, B. Luderer, H.-R. Schwarz, J. Blath, A. Schied, S. Dempe, G. Wanka, and S. Gottwald. *Taschenbuch der mathematik*, volume 1. Springer-Verlag, 2012.

[12] Bruce MacEvoy. Light and the eye. https://www.handprint.com/HP/WCL/color1.html, 2015. [Online; accessed May 07, 2023].

[13] Y. Chen, Y. Yang, Z. Feng, P. P. Altermatt, and H. Shen. Color modulation of c-si solar cells without significant current-loss by means of a double-layer anti-reflective coating. *27th EUPVSEC*, pages 2014–2016, 2012.

[14] F. Clapper and J. Yule. The effect of multiple internal reflections on the densities of half-tone prints on paper. *JOSA*, 43(7):600–603, 1953.

[15] I. E. Commission. *International Standard IEC 60904-9:2007.* IEC, International Electrotechnical Commission, Geneva, Switzerland, 2007.

[16] I. E. Commission. *International Standard IEC 60904-8.* IEC, International Electrotechnical Commission, Geneva, Switzerland, 2014.

[17] M. de Simón-Martín, C. Alonso-Tristán, and M. Díez-Mediavilla. Diffuse solar irradiance estimation on building's façades: review, classification and benchmarking of 30 models under all sky conditions. *Renewable and Sustainable Energy Reviews*, 77:783–802, 2017.

[18] C. Demain, M. Journée, and C. Bertrand. Evaluation of different models to estimate the global solar radiation on inclined surfaces. *Renewable energy*, 50:710–721, 2013.

[19] E. Demichel. Le procédé. *Société Française de Photographie*, 26:17–21, 1924.

[20] M. Diez-Mediavilla, A. De Miguel, and J. Bilbao. Measurement and comparison of diffuse solar irradiance models on inclined surfaces in valladolid (spain). *Energy Conversion and Management*, 46(13-14):2075–2092, 2005.

[21] F. Dorusch. Performance analysis of a multi-coloured building integrated pv system. *11th Conference on Advanced Building Skins 2016*, 2016.

[22] J. Duffy and W. Beckman. *Solar Engineering of Thermal Processes, 2013.* John Willey & Sons, NY, 2013.

[23] E. D. Dunlop, D. Halton, and H. A. Ossenbrink. 20 years of life and more: where is the end of life of a pv module? In *Conference Record of the Thirty-first IEEE Photovoltaic Specialists Conference, 2005.*, pages 1593–1596, 2005.

[24] G. Eder, K. Knöbl, L. Maul, M. Aichinger, G. Peharz, W. Nemitz, and K. Berger. Designed bipv-elements with printed front-glass: simulation and experimental evaluation of the effect of printing on the electrical performance. In *12th Conference on Advanced Building Skins*, 2017.

[25] G. Eder, G. Peharz, R. Trattnig, P. Bonomo, E. Saretta, F. Frontini, C. S. Polo López, H. R. Wilson, J. Eisenlohr, N. M. Chivelet, and et al. *Coloured BIPV: Market, Research and Development*. 2019.

[26] J. Ehlert and T. Smith. View factors for perpendicular and parallel rectangular plates. *Journal of thermophysics and heat transfer*, 7(1):173–175, 1993.

[27] D. Erbs, S. Klein, and J. Duffie. Estimation of the diffuse radiation fraction for hourly, daily and monthly-average global radiation. *Solar Energy*, 28(4):293–302, 1982.

[28] U. Feister and K.-H. Grasnick. Solar uv radiation measurements at potsdam (52° 22' n, 13° 5' e). *Solar Energy*, 49(6):541–548, 1992.

[29] I. O. for Standardization. *ISO 9847:1992 - Solar Energy-Calibration of Field Pyranometers by Comparison to a Reference Pyranometer*. ISO, International Organization for Standardization, 1992.

[30] Freudenberg Performance Materials SE & Co. KG. Light diffuser from freudenberg. https://www.freudenberg-pm.com/-/media/Files/www,-d-,freudenbergpm,-d-,com/Company/2018 04 16 DE Produktbroschuere.pdf, 2019. [Online; accessed May 07, 2023].

[31] A. Gershun. Fresnel reflection of diffusely incident light. *JOSA*, 35(2):162–163, 1945.

[32] T. Gewohn, S. Blankemeyer, M. Vogt, H. Schulte-Huxel, M. Köntges, B. Lim, C. Schinke, and R. Brendel. Laminated textiles enabling custom appearance of building integrated photovoltaic modules. *35th European Photovoltaic Solar Energy Conference and Exhibition; 1842-1844*, 2018.

[33] T. Gewohn, D. Bredemeier, C. Schinke, B. Lim, and R. Brendel. Improved calculation of the power gain of vertical pv modules due to ground reflection using the ground view factor. *IEEE Journal of Photovoltaics*, 12(6):1567–1575, 2022.

[34] T. Gewohn, M. Koopmeiners, M. Vogt, B. Lim, C. Schinke, and R. Brendel. Outdoor testing facility for an experimental validation of yield predictions for building-integrated photovoltaic modules. *37th European Photovoltaic Solar Energy Conference and Exhibition; 1915-1919*, 2020.

[35] T. Gewohn, C. Schinke, B. Lim, and R. Brendel. Predicting color and short-circuit current of colored BIPV modules. *AIP Advances*, 11(9), 2021.

[36] T. Gewohn, M. R. Vogt, B. Lim, C. Schinke, and R. Brendel. Postproduction coloring of photovoltaic modules with imprinted textiles. *IEEE Journal of Photovoltaics*, 11(1):138–143, 2021.

[37] C. Gueymard. An anisotropic solar irradiance model for tilted surfaces and its comparison with selected engineering algorithms. *Solar energy*, 38(5):367–386, 1987.

[38] C. A. Gueymard. Direct and indirect uncertainties in the prediction of tilted irradiance for solar engineering applications. *Solar Energy*, 83(3):432–444, 2009.

[39] C. A. Gueymard and D. R. Myers. Evaluation of conventional and high-performance routine solar radiation measurements for improved solar resource, climatological trends, and radiative modeling. *Solar Energy*, 83(2):171–185, 2009.

[40] I. Hall, R. Prairie, H. Anderson, and E. Boes. Generation of a typical meteorological year. Technical report, Sandia Labs., Albuquerque, NM (USA), 1978.

[41] J. Halme and P. Mäkinen. Theoretical efficiency limits of ideal coloured opaque photovoltaics. *Energy & Environmental Science*, 12(4):1274–1285, 2019.

[42] J. E. Hay and D. J.A. Calculation of the solar radiation incident on inclined surfaces. In *Proceedings first Canadian Solar Radiation Data Workshop, Toronto. Ontario, Canada 1980*, 1980.

[43] R. D. Hersch and M. Hébert. Base models for color halftone reproduction. *Handbook of Digital Imaging*, pages 1–54, 2015.

[44] M. Hofmann and G. Seckmeyer. Influence of various irradiance models and their combination on simulation results of photovoltaic systems. *Energies*, 10(10):1495, 2017.

[45] T. Huld, R. Müller, and A. Gambardella. A new solar radiation database for estimating pv performance in europe and africa. *Solar Energy*, 86(6):1803–1815, 2012.

[46] P. Ineichen. Global irradiance on tilted and oriented planes: model validations. *University of Geneva*, 2011.

[47] P. Ineichen, R. Perez, R. Seal, E. Maxwell, and A. Zalenka. Dynamic global-to-direct irradiance conversion models. *ASHRAE transactions*, 98(1):354–369, 1992.

[48] CIE standard colorimetric illuminants. Standard, International Comission on Illumination, Geneva, CH, 1999.

[49] S. Kabelac and D. Vortmeyer. *K1 Strahlung technischer Oberflächen*, pages 1083–1096. Springer Berlin Heidelberg, Berlin, Heidelberg, 2013.

[50] Kaleo Solar. Solar modules printed with high-resolution portraits. https://www.pveurope.eu/solar-modules/solar-modules-printed-high-resolution-portraits, 2021. [Online; accessed May 07, 2023].

[51] R. Kang. *Digital color halftoning*. SPIE Optical Engineering Press Bellingham (WA), 1999.

[52] T. M. Klucher. Evaluation of models to predict insolation on tilted surfaces. *Solar energy*, 23(2):111–114, 1979.

[53] M. Köntges, H. Schulte-Huxel, S. Blankemeyer, M. R. Vogt, H. Holst, and R. Reineke-Koch. Measuring the light recovery factor of backsheets in photovoltaic modules. *Solar Energy Materials and Solar Cells*, 186:175–183, 2018.

[54] J. Kratochvil, W. Boyson, and D. King. Photovoltaic array performance model. Technical report, 2004.

[55] C. Kutter, B. Bläsi, H. Wilson, T. Kroyer, M. Mittag, O. Höhn, and M. Heinrich. Decorated building-integrated photovoltaic modules: Power loss, color appearance and cost analysis. *35th European Photovoltaic Solar Energy Conference and Exhibition; 1488-1492*, 2018.

[56] M. Lave, W. Hayes, A. Pohl, and C. W. Hansen. Evaluation of global horizontal irradiance to plane-of-array irradiance models at locations across the united states. *IEEE journal of Photovoltaics*, 5(2):597–606, 2015.

[57] B. Liu and R. Jordan. Daily insolation on surfaces tilted towards equator. *ASHRAE J.;(United States)*, 10, 1961.

[58] Lof Solar. C-cell classic series. http://www.lofsolar.com/Standard-series#4, 2021. [Online; accessed May 07, 2023].

[59] P. Loutzenhiser, H. Manz, C. Felsmann, P. Strachan, T. Frank, and G. Maxwell. Empirical validation of models to compute solar irradiance on inclined surfaces for building energy simulation. *Solar Energy*, 81(2):254–267, 2007.

[60] M. R. Luo, G. Cui, and B. Rigg. The development of the cie 2000 colour-difference formula: Ciede2000. *Color Research & Application: Endorsed by Inter-Society Color Council, The Colour Group (Great Britain), Canadian Society for Color, Color Science Association of Japan, Dutch Society for the Study of Color, The Swedish Colour Centre Foundation, Colour Society of Australia, Centre Français de la Couleur*, 26(5):340–350, 2001.

[61] E. L. Maxwell. A quasi-physical model for converting hourly global horizontal to direct normal insolation. Technical report, Solar Energy Research Inst., Golden, CO (USA), 1987.

[62] C. S. McCamy, H. Marcus, J. G. Davidson, et al. A color-rendition chart. *J. App. Photog. Eng*, 2(3):95–99, 1976.

[63] R. Mubarak, M. Hofmann, S. Riechelmann, and G. Seckmeyer. Comparison of modelled and measured tilted solar irradiance for photovoltaic applications. *Energies*, 10(11):1688, 2017.

[64] A. M. Noorian, I. Moradi, and G. A. Kamali. Evaluation of 12 models to estimate hourly diffuse irradiation on inclined surfaces. *Renewable energy*, 33(6):1406–1412, 2008.

[65] G. Notton, C. Cristofari, and P. Poggi. Performance evaluation of various hourly slope irradiation models using mediterranean experimental data of ajaccio. *Energy Conversion and Management*, 47(2):147–173, 2006.

[66] G. Notton, P. Poggi, and C. Cristofari. Predicting hourly solar irradiations on inclined surfaces based on the horizontal measurements: performances of the association of well-known mathematical models. *Energy Conversion and Management*, 47(13-14):1816–1829, 2006.

[67] J. Orgill and K. Hollands. Correlation equation for hourly diffuse radiation on a horizontal surface. *Solar energy*, 19(4):357–359, 1977.

[68] G. Peharz and A. Ulm. Quantifying the influence of colors on the performance of c-si photovoltaic devices. *Renewable energy*, 129:299–308, 2018.

[69] R. Perez, P. Ineichen, R. Seals, J. Michalsky, and R. Stewart. Modeling daylight availability and irradiance components from direct and global irradiance. *Solar energy*, 44(5):271–289, 1990.

[70] R. Perez, R. Seals, P. Ineichen, R. Stewart, and D. Menicucci. A new simplified version of the perez diffuse irradiance model for tilted surfaces. *Solar energy*, 39(3):221–231, 1987.

[71] R. Perez, R. Stewart, R. Seals, and T. Guertin. The development and verification of the perez diffuse radiation model. 1988.

[72] D. Reindl, W. Beckman, and J. Duffie. Diffuse fraction correlations. *Solar Energy*, 45(1):1–7, 1990.

[73] D. Reindl, W. Beckman, and J. Duffie. Evaluation of hourly tilted surface radiation models. *Solar energy*, 45(1):9–17, 1990.

[74] C. T. Report. *Colorimetry (Second Edition) CIE 15.2*. Central Bureau of the International Commission on Illumination (CIE): Vienna, Austria, 1986.

[75] A. Røyset, T. Kolås, and B. P. Jelle. Coloured building integrated photovoltaics: Influence on energy efficiency. *Energy and Buildings*, 208:109623, 2020.

[76] J. Schanda. *Colorimetry: understanding the CIE system*. John Wiley & Sons, 2007.

[77] Z. Schuessler. Defining delta e. `https://zschuessler.github.io/DeltaE/learn/`. [Online; accessed May 07, 2023].

[78] G. Sharma, W. Wu, and E. N. Dalal. The ciede2000 color-difference formula: Implementation notes, supplementary test data, and mathematical observations. *Color Research & Application: Endorsed by Inter-Society Color Council, The Colour Group (Great Britain), Canadian Society for Color, Color Science Association of Japan, Dutch Society for the Study of Color, The Swedish Colour Centre Foundation, Colour Society of Australia, Centre Français de la Couleur*, 30(1):21–30, 2005.

[79] T. Söderström, P. Papet, and J. Ufheil. Smart wire connection technology. In *the 28th European Photovoltaic Solar Energy Conference*, pages 495–499, 2013.

[80] SolarGlasLabor. Individuelles design für photovoltaik-panels. https://gewerbe-basel.ch/content/uploads/2017/03/Photovoltaik-Panels-Hintergrundinfo.pdf, 2017. [Online; accessed May 07, 2023].

[81] SoliTek cells. Manufacturer's data sheet of the solitek standard m.60-b-300 pv module, 2019.

[82] J. S. Stein, W. F. Holmgren, J. Forbess, and C. W. Hansen. Pvlib: Open source photovoltaic performance modeling functions for matlab and python. In *2016 IEEE 43rd Photovoltaic Specialists Conference (PVSC)*, pages 3425–3430, 2016.

[83] A. Stockman and L. T. Sharpe. The spectral sensitivities of the middle-and long-wavelength-sensitive cones derived from measurements in observers of known genotype. *Vision research*, 40(13):1711–1737, 2000.

[84] S. M. Sze. *Physics of Semiconductor Devices, 2nd edn.* Wiley, New York, USA, 1981.

[85] R. C. Temps and K. Coulson. Solar radiation incident upon slopes of different orientations. *Solar energy*, 19(2):179–184, 1977.

[86] M. Theristis, V. Venizelou, G. Makrides, and G. E. Georghiou. Energy yield in photovoltaic systems. In *McEvoy's handbook of photovoltaics*, pages 671–713. Elsevier, 2018.

[87] M. Vogt, T. Gewohn, K. Bothe, C. Schinke, and R. Brendel. Impact of using spectrally resolved ground albedo data for performance simulations of bifacial modules. In *Proceedings of the 35th Eur. Photovolt. Sol. Energy Conference Exhibition, Brussels*, pages 1011–1016, 2018.

[88] D. Vortmeyer and S. Kabelac. *K2 Sichtfaktoren*, pages 1097–1114. Springer Berlin Heidelberg, Berlin, Heidelberg, 2013.

[89] Wikimedia Commons. Halftoningcolor. https://commons. wikimedia.org/ wiki/ File:Halftoningcolor.svg, 2009. [Online; accessed May 07, 2023].

[90] R. Witteck. *Analysis of cell to module losses and UV radiation hardness for passivated emitter and rear cells and modules.* München: Verlag Dr. Hut, 2019.

[91] J. A. Yule. *Principles of color reproduction.* John Wiley & Sons, New York, USA, 1967.

List of Publications

Peer reviewed journal papers

T. Gewohn, M. R. Vogt, B. Lim, C. Schinke, and R. Brendel. Postproduction coloring of photovoltaic modules with imprinted textiles. IEEE Journal of Photovoltaics, 11(1):138–143, 2021.

T. Gewohn, C. Schinke, B. Lim, and R. Brendel. Predicting color and short-circuit current of colored BIPV modules. AIP Advances, 11(9), 09 2021.

T. Gewohn, D. Bredemeier, C. Schinke, B. Lim, and R. Brendel. Improved calculation of the power gain of vertical pv modules due to ground reflection using the ground view factor. IEEE Journal of Photovoltaics, 12(6):1567–1575, 2022.

Conference proceedings papers

B. Matthias, D. Brockmann, A. Hansen, K. Horke, G. Knoop, **T. Gewohn**, M. Zabic, A. Krüger, and T. Ripken. Concept for image-guided vitreo-retinal fs-laser surgery: adaptive optics and optical coherence tomography for laser beam shaping and positioning. In Ophthalmic Technologies XXV, volume 9307, pages 55–62. SPIE, 2015.

T. Gewohn, S. Blankemeyer, M. Vogt, H. Schulte-Huxel, M. Köntges, B. Lim, C. Schinke, and R. Brendel. Laminated textiles enabling custom appearance of building integrated photovoltaic modules. 35th European Photovoltaic Solar Energy Conference and Exhibition; 1842-1844, 2018.

M. Vogt, **T. Gewohn**, K. Bothe, C. Schinke, and R. Brendel. Impact of using spectrally resolved ground albedo data for performance simulations of bifacial mod- ules. In Proceedings of the 35th Eur. Photovolt. Sol. Energy Conference Exhibition, Brussels, pages 1011–1016, 2018.

M. Vogt, R. Witteck, **T. Gewohn**, H. Schulte-Huxel, C. Schinke, M. Köntges, K. Bothe, and R. Brendel. Boosting pv module efficiency beyond the efficiency of its solar cells–a ray tracing study with daidalos now available to the scientific community. EUPVSEC 2019, pages 795–800, 2019.

M. R. Vogt, R. Witteck, **T. Gewohn**, H. Schulte-Huxel, C. Schinke, K. Bothe, and R. Brendel. Ray tracing of complete solar cell modules. In OSA Advanced Photonics Congress (AP) 2019 (IPR, Networks, NOMA, SPPCom, PVLED), page PW2C.1. Optica Publishing Group, 2019.

T. Gewohn, M. Koopmeiners, M. Vogt, B. Lim, C. Schinke, and R. Brendel. Out- door testing facility for an experimental validation of yield predictions for building-integrated photovoltaic modules. 37th European Photovoltaic Solar Energy Conference and Exhibition; 1915-1919, 2020.

D. Bredemeier, C. Schinke, **T. Gewohn**, H. Wagner-Mohnsen, R. Niepelt, and R. Brendel. Fast evaluation of rooftop and façade pv potentials using backward ray tracing and machine learning. In 2021 IEEE 48th Photovoltaic Specialists Conference (PVSC), pages 0294–0299, 2021.

Others

O. Badelt, R. Niepelt, J. Wiehe, S. Matthies, **T. Gewohn**, M. Stratmann, R. Brendel, and C. von Haaren. Integration von Solarenergie in die niedersächsische Energielandschaft (INSIDE). URL: https://www. umwelt. niedersachsen.de/ startseite /aktuelles/ publikationen/ klimaschutz_amp_energie/ publikationen-klimaschutz -und -energie -8854. html (seen on: 30.04.2023), 2020.

Acknowledgements

Zum Schluss möchte ich mich bei allen Personen bedanken, die zum Gelingen meiner Dissertation beigetragen haben:

- Prof. Dr.-Ing. Rolf Brendel für die Aufnahme als Doktorand, die Betreuung meiner Promotion, den Freiraum bei der Wahl der Schwerpunkte und die zahlreichen konstruktiven Diskussionen und motivierende Anregungen,
- Dr. Bianca Lim und Dr. Carsten Schinke für die wissenschaftliche Begleitung, die Unterstütung und den regelmäßigen Austausch,
- Dr. Dennis Bredemeier, Dr. Malte Vogt und Dr. Henning Schulte-Huxel für die zahlreichen wissenschaftlichen Gespräche und ihre Hilfsbereitschaft,
- Susanne Blankemeier und Iris Kunze für ihre Hilfe und die Zusammenarbeit bei der Herstellung der CoTex Module und den damit verbundenen Experimenten,
- Allen Kolleginnen und Kollegen an der Leibniz Universität und am ISFH für die tolle Atmosphäre
- Meinen Eltern Heike und Peter Gewohn für die uneingeschränkte Unterstützung während des gesamten Studiums und der anschließenden Promotionszeit,
- Meinem Bruder Oliver Gewohn für die Hilfe beim Programmieren, wenn die DAIDALOS Simulationen auf dem Server mal nicht so durchlaufen wollten, wie ich es wollte,
- Mark Wegner der durch die Schenkung seines Radiergummis einen unschätzbaren Beitrag zur Wissenschaft geleistet hat,
- Meiner Frau Dr. Elsa Gewohn, die meine wissenschaftlichen Texte immer zuerst lesen und meine Vorträge als erste hören musste, für ihr Verständnis, ihre Unterstützung und die manchmal notwendige Ablenkung.